

# Highly Physical Solar Radiation Pressure Modeling During Penumbra Transitions

Robert V. Robertson

Dissertation submitted to the Faculty of the  
Virginia Polytechnic Institute and State University  
in partial fulfillment of the requirements for the degree of

Doctor of Philosophy  
in  
Aerospace Engineering

Gregory D. Earle, Co-Chair  
Scott M. Bailey, Co-Chair  
Kevin A. Shinpaugh  
Wayne A. Scales  
Michael A. Shoemaker  
Jonathan T. Black

April 30, 2015  
Blacksburg, Virginia

Keywords: Solar Radiation Pressure, Penumbra, Atmospheric Optics, Satellite  
Accelerometry, Spacecraft Navigation, Orbit Determination  
Copyright 2015, Robert V. Robertson

ProQuest Number: 10647629

All rights reserved

INFORMATION TO ALL USERS

The quality of this reproduction is dependent upon the quality of the copy submitted.

In the unlikely event that the author did not send a complete manuscript and there are missing pages, these will be noted. Also, if material had to be removed, a note will indicate the deletion.



ProQuest 10647629

Published by ProQuest LLC (2017). Copyright of the Dissertation is held by the Author.

All rights reserved.

This work is protected against unauthorized copying under Title 17, United States Code  
Microform Edition © ProQuest LLC.

ProQuest LLC.  
789 East Eisenhower Parkway  
P.O. Box 1346  
Ann Arbor, MI 48106 – 1346

# Highly Physical Solar Radiation Pressure Modeling During Penumbra Transitions

Robert V. Robertson

(ABSTRACT)

Solar radiation pressure (SRP) is one of the major non-gravitational forces acting on spacecraft. Acceleration by radiation pressure depends on the radiation flux; on spacecraft shape, attitude, and mass; and on the optical properties of the spacecraft surfaces. Precise modeling of SRP is needed for dynamic satellite orbit determination, space mission design and control, and processing of data from space-based science instruments. During Earth penumbra transitions, sunlight is passing through Earth's lower atmosphere and, in the process, its path, intensity, spectral composition, and shape are significantly affected.

This dissertation presents a new method for highly physical SRP modeling in Earth's penumbra called Solar radiation pressure with Oblateness and Lower Atmospheric Absorption, Refraction, and Scattering (SOLAARS). The fundamental geometry and approach mirrors past work, where the solar radiation field is modeled using a number of light rays, rather than treating the Sun as a single point source. This dissertation aims to clarify this approach, simplify its implementation, and model previously overlooked factors. The complex geometries involved in modeling penumbra solar radiation fields are described in a more intuitive and complete way to simplify implementation. Atmospheric effects due to solar radiation passing through the troposphere and stratosphere are modeled, and the results are tabulated to significantly reduce computational cost. SOLAARS includes new, more efficient and accurate approaches to modeling atmospheric effects which allow us to consider the spatial and temporal variability in lower atmospheric conditions. A new approach to modeling the influence of Earth's polar flattening draws on past work to provide a relatively simple but accurate method for this important effect.

Previous penumbra SRP models tend to lie at two extremes of complexity and computational cost, and so the significant improvement in accuracy provided by the complex models has often been lost in the interest of convenience and efficiency. This dissertation presents a simple model which provides an accurate alternative to the full, high precision SOLAARS model with reduced complexity and computational cost. This simpler method is based on curve fitting to results of the full SOLAARS model and is called SOLAARS Curve Fit (SOLAARS-CF).

Both the high precision SOLAARS model and the simpler SOLAARS-CF model are applied to the Gravity Recovery and Climate Experiment (GRACE) satellites. Modeling results are compared to the sub-nm/s<sup>2</sup> precision GRACE accelerometer data and the results of a traditional penumbra SRP model. These comparisons illustrate the improved accuracy of the SOLAARS and SOLAARS-CF models. A sensitivity analyses for the GRACE orbit illustrates the significance of various input parameters and features of the SOLAARS model on results.

The SOLAARS-CF model is applied to a study of penumbra SRP and the Earth flyby anomaly. Beyond the value of its results to the scientific community, this study provides an application example where the computational efficiency of the simplified SOLAARS-CF model is necessary. The Earth flyby anomaly is an open question in orbit determination which has gone unsolved for over 20 years. This study quantifies the influence of penumbra

SRP modeling errors on the observed anomalies from the Galileo, Cassini, and Rosetta Earth flybys. The results of this study prove that penumbra SRP is not an explanation for or significant contributor to the Earth flyby anomaly.

This work received support through research fellowships, assistantships, and internships from the Virginia Space Grant Consortium, Virginia Tech Institute for Critical Technology and Applied Science, Los Alamos National Laboratory, Air Force Research Laboratory, and the German Academic Exchange Service.

# Acknowledgments

I would first like to thank my co-advisers, Dr. Gregory Earle and Dr. Scott Bailey, for supporting me over the last four years. In particular, I appreciate Greg's constant and selfless prodding to write my research papers instead of working on more fun things, like his CubeSat. I would also like to thank the other members of my committee, especially Dr. Kevin Shinpaugh and Dr. Mike Shoemaker. Kevin introduced me to aerospace engineering at Virginia Tech many years ago and has supported my work in some capacity ever since. Mike has been especially involved in my research and gracious with his time, always providing great feedback and productive discussions. Thanks to Dr. Troy Henderson for advising me for my first two years in graduate school at Virginia Tech and encouraging and advocating for me during that time.

This research project began in 2010, when I was an undergraduate researcher for one summer at the Institute of Geodesy (IFE) in Hannover, Germany. I would like to recognize Dr. Jakob Flury, Tamara Bandikova, and Manuel Schilling of the IFE for their very significant role in the development of the SOLAARS model. Jakob and Tamara are responsible more than anyone else for my continued involvement in this line of research, and I cannot overstate the value of their contributions to the development of the SOLAARS model. Thanks also to Dr. David Vokrouhlický for taking the time to teach Tamara and I about his modeling methods, which form the foundation of my research.

I need to thank my friends at Space@VT for all of the good times, welcome distractions, and even occasional research help over the years. You know who you are.

Finally, I want to thank my family for their encouragement over the many years I have spent in school. I especially want to thank my father, Mark Robertson, for being such a great role model and supporter of my education. Last but not least, thank you to my amazing fiance, Sarah Scott, who has always propped me up when I needed it and who's dedication and discipline has always inspired me to be better.

# Contents

<b>1</b>	<b>Introduction</b>	<b>1</b>
1.1	Solar radiation pressure . . . . .	1
1.2	Earth oblateness . . . . .	3
1.3	Atmospheric radiative transfer . . . . .	5
1.4	Problem statement and motivation . . . . .	10
1.5	Organization of Dissertation . . . . .	12
<b>2</b>	<b>Review of Relevant Literature</b>	<b>14</b>
2.1	Penumbra SRP modeling . . . . .	14
2.2	Earth oblateness and penumbra SRP . . . . .	17
2.3	Atmospheric refraction . . . . .	20
2.4	Atmospheric extinction . . . . .	21
2.5	Summary . . . . .	27
<b>3</b>	<b>Theory and modeling</b>	<b>28</b>
3.1	Earth oblateness . . . . .	29
3.1.1	Locating the characteristic grazing point . . . . .	31
3.1.2	Describing the osculating spherical Earth . . . . .	34
3.1.3	Implementation . . . . .	36
3.2	Fundamental SRP acceleration formula . . . . .	38
3.3	Light ray geometry . . . . .	41
3.4	SOLAARS Implementation . . . . .	48

3.5	Refraction parameters . . . . .	48
3.6	Radiance coefficients . . . . .	53
3.6.1	Rayleigh scattering . . . . .	57
3.6.2	Aerosol extinction . . . . .	60
3.6.3	Molecular absorption . . . . .	62
3.6.4	Cloud extinction . . . . .	66
3.6.5	Extinction model validation . . . . .	66
3.7	SOLAARS-CF: A fast approximation to SOLAARS . . . . .	67
3.7.1	Geometric parameters and SOLAARS data . . . . .	69
3.7.2	Curve fitting . . . . .	71
3.7.3	Implementation . . . . .	72
<b>4</b>	<b>Results and Analysis</b>	<b>76</b>
4.1	Application to the GRACE satellites . . . . .	76
4.1.1	Testing SOLAARS-CF oblateness with GRACE data . . . . .	78
4.1.2	Applying SOLAARS to GRACE . . . . .	80
4.1.3	SOLAARS solar radiation fields . . . . .	81
4.1.4	Two typical GRACE penumbra transitions . . . . .	84
4.1.5	Issues to consider . . . . .	87
4.1.6	A series of subsequent transitions . . . . .	88
4.1.7	Sensitivity analysis . . . . .	90
4.1.8	A note on penumbra boundaries . . . . .	94
4.2	Application to the Earth flyby anomaly . . . . .	95
4.2.1	Computing the penumbra SRP anomaly contribution . . . . .	97
4.2.2	SRP accelerations . . . . .	98
4.2.3	Error estimation and anomaly behavior . . . . .	100
4.2.4	Penumbra SRP contribution to the anomaly . . . . .	101
<b>5</b>	<b>Conclusions and Future Work</b>	<b>102</b>

5.1	Review . . . . .	102
5.1.1	Application to the GRACE satellites . . . . .	102
5.1.2	Application to the Earth flyby anomaly . . . . .	102
5.2	Conclusions . . . . .	103
5.3	Future work . . . . .	103
	<b>Bibliography</b>	<b>105</b>

# List of Figures

1.1	Geometry of photon momentum transfer for absorbed (a) and reflected (b) photons. A reflected photon results in a different direction and magnitude of momentum transferred to the object. . . . .	2
1.2	Time spent in penumbra during each orbital period as a function of circular orbit altitude. Orbits are in the ecliptic plane and simulations are carried out using the SOLAARS-CF model described in Section 3.7. Note that due to the orbit-Sun geometry assigned to each orbit, these results represent the minimum time spent in penumbra at each altitude. . . . .	4
1.3	Geometry of a light ray passing Earth to strike a satellite in orbit. The dotted line represents a spherical model of Earth that would incorrectly lead one to determine that the light ray is blocked. . . . .	4
1.4	Extraterrestrial solar spectral irradiance and with blackbody irradiances at various temperatures from Thomas and Stamnes (2002). These curves illustrate how the extraterrestrial solar spectrum can be approximated as a blackbody spectrum. The spectral subranges are indicated by the vertical, dotted lines. . . . .	6
1.5	Scattering patterns for various particle sizes from McCartney (1976). Note the symmetry of the Rayleigh scattering case with a small particle shown in section (a). The complex patterns of scattering with larger particles shown in sections (b) and (c) require the more complex Mie scattering theory. . . . .	8
1.6	A comparison of normalized line broadening profiles from Thomas (1999). In this plot, $\nu$ is frequency and $\Delta\nu$ is the Doppler width for the Doppler and Voight profiles and the Lorentz width for the Lorentz profile. . . . .	9
1.7	Eastern component of crosswind derived from processing on GOCE accelerometer data and associated error estimates from Doornbos (2014). The high error region corresponds to GOCE penumbra, and the faint white line pointed out in the upper, red region of the data represents processing errors due to mis-modeling of penumbra SRP. . . . .	11

1.8	Absolute difference in orbital elements for a debris object ( $20 \text{ m}^2/\text{kg}$ area-to-mass ratio) in the geosynchronous orbit regime propagated with different pnemubra SRP models from Hubaux et al. (2012). In the legend, $\nu_p$ is the new shadow function presented by Hubaux et al. (2012), $\nu_c$ is a cylindrical shadow function, and $\nu_M$ is the shadow function that appears in Montenbruck and Gill (2000). . . . .	13
2.1	Geometry of atmosphere-free penumbra shadow cones and cylindrical shadow model from Hubaux et al. (2012). . . . .	15
2.2	Comparison of shadow functions from Hubaux et al. (2012). In the legend, $\nu_p$ is the new shadow function presented by Hubaux et al. (2012), $\nu_c$ is a cylindrical shadow function, and $\nu_M$ is the shadow function from Montenbruck and Gill (2000). . . . .	15
2.3	Geometry involved in the M&G 2000 penumbra SRP shadow function (image from Montenbruck and Gill (2000)). The geometric parameters here are used to compute the shadow function value, which is simply the visible area of the solar disc from behind the atmosphere-free occulting body divided by the total area of the disc. . . . .	16
2.4	Sunset penumbra SRP accelerations (denoted $T$ here) from Vokrouhlický et al. (1993) illustrating the significance of atmospheric effects. Curve 1 shows results from their model, Curve 2 shows the results of an atmosphereless model equivalent to the M&G 2000 model, and Curve 3 is a cylindrical shadow, step approximation to the transition. . . . .	17
2.5	Geometry of penumbra phases (full phase, pnumbra, and umbra) from Adhya et al. (2004). The phase is determined by the number of intersections between the dotted lines connecting the satellite to the solar disc limits and the Earth spheroid. . . . .	18
2.6	Geometry from Vokrouhlický et al. (1996) of the osculating spherical Earth used to approximate the oblate Earth. The satellite is at the position labeled “SAT”. The light ray grazing point, which is the point on Earth which the ray passes closest to, lies along the line dimensioned $h$ . The spherical, osculating Earth is positioned and assigned a radius so that it is: (1) tangent to the oblate spheroid Earth at the grazing point and (2) matches the radius of curverature of the oblate Earth at the grazing point in the Sun-Earth-satellite plane. . .	19
2.7	Photograph taken by astronaut Scott Carpenter from the MA-7 orbiter from Cameron et al. (1963). Note the significant compression of the solar disc due to atmospheric refraction. . . . .	20

2.8	Refraction modeling geometry from Auer and Standish (2000). The distance to the geocenter ( $r$ ) and angle ( $\psi$ ) used to model refraction in the method presented by Auer and Standish (2000) . . . . .	21
2.9	An example of a layered atmosphere model for radiative transfer from Avrett and Loeser (1984). This layered model of the atmosphere assumes spherical shells. Note that some models assume flat, infinite layers to further simplify the problem. . . . .	22
2.10	Comparison of Results from MODTRAN2 and FASCODE from Anderson et al. (1993). The line labeled “MODTRAN2(L)” shows results from using a more complex temperature model than the model with results labeled “MODTRAN2”. This comparison indicates that the MODTRAN2 RTC, using a more detailed temperature model, shows strong correlation with FASCODE results. . . . .	24
2.11	Comparison of Experimental (—), SPCTRAL2 (- - -), and SMARTS2 (· · ·) Irradiance Results In Valencia, Spain from Utrillas et al. (1998). These results indicate that the more recent SMARTS2 model performs better. Note that over other spectral ranges, the two models performed more consistently and both produced better correlation with experimental results than over the range shown here. . . . .	25
2.12	Simulated photon paths in a Monte Carlo model from Bird 1982. The spherical shell atmosphere shown here is the model atmosphere for the BRITE Monte Carlo RTC. . . . .	27
3.1	A satellite penumbra transition with atmospheric effects. The boundaries of the penumbra region are extended by the atmosphere in the full sunlight and umbra directions. Note the significant compression of the SOLAARS modeled solar radiation fields in penumbra due to atmospheric refraction. . . . .	29
3.2	Flow of inputs and intermediate results for computing penumbra SRP accelerations. We tabulate the output of atmospheric effects modeling, where the most computationally intensive steps take place, so that we can do this very precisely without influencing the speed of SRP acceleration calculations. . . . .	30

3.3	Geometry involved in SOLAARS Earth oblateness modeling. The satellite position ( $\vec{r}$ ) and satellite to Sun vector ( $\vec{d}$ ) are used to find the grazing point vector ( $\vec{G}$ ). The $\hat{N}$ plane defines the slice of the spheroid described in the two dimensional illustration on the right. The blue ellipse is a slice by the $\hat{N}$ plane of the Earth oblate spheroid, and the green ellipse is a scaled version of the blue ellipse which results in a single intersection with $\vec{d}$ . The blue ellipse is parameterized by its semimajor ( $\vec{a}$ ) and semiminor ( $\vec{b}$ ) axis vectors, and the angle $\lambda_e$ describes the orientation of $G$ in this ellipse. $\vec{\gamma}$ is the normal to the ellipse at the angle $\lambda_e$ . $R_{\oplus}$ and $\vec{\alpha}$ are the radius and center of the osculating spherical Earth. . . . .	32
3.4	Flowchart outlining the process for adjusting geometric parameters for Earth oblateness at each satellite position. . . . .	37
3.5	Earth pointing reference frame ( $\{e\}$ ) for SRP calculations and spherical coordinates $\theta$ and $\phi$ . Note that in the left view, the Sun-Earth-satellite plane is the plane of the page. $\Delta\phi$ and $\Delta\theta$ are used in numerical integration in the place of the differential solid angle $\Delta\Omega$ in Eq. 3.30. . . . .	40
3.6	Light ray geometry in the $\phi = 0$ plane. Points $H$ , $E$ , $G$ , $B$ , and $J$ are the center of the Sun, location of emission, geocenter, vertex of refraction, and satellite position, respectively. The line from the geocenter to the vertex of refraction has three segments: the Earth radius ( $R_{\oplus}$ ), grazing height ( $h_g$ ), and refractive height ( $S$ ). $R$ and $r$ are the geocentric distances to the Sun and satellite, respectively. $Re$ is the light ray refraction angle and $\omega$ is geocentric Sun-satellite angle. . . . .	42
3.7	Geometry for transitioning from the actual geocentric Sun-satellite angle ( $\omega$ ) to the atmosphere-free angle ( $\bar{\omega}$ ) which simplifies our geometric relations. Point $J$ is the satellite position and point $D$ is the atmosphere-free position along the un-refracted ray with the same $\theta$ angle and satellite-Earth distance ( $r$ ). Point $B$ is the vertex of refraction and points $A$ and $C$ form equivalent right triangles with $B$ and the geocenter at point $G$ . The distance to the vertex of refraction is the sum of the Earth radius ( $R_{\oplus}$ ), grazing height ( $h_G$ ), and refractive height ( $S$ ). . . . .	43
3.8	Geometry involved in computing the overall $\theta$ limits of the solar radiation field, which lie in the $\phi = 0$ plane. Points $H$ and $G$ are the center of the Sun and geocenter, respectively. Point $D$ and angle $\bar{\omega}$ are the atmosphere-free satellite position and Sun-satellite angle illustrated in Fig. 3.7. The angles $\gamma$ and $\delta_{max}$ are computed based on the satellite-Sun distance ( $d$ ), satellite-Earth distance ( $r$ ), and the Sun-Earth distance ( $R$ ) and used to compute the overall $\theta$ limits. . . . .	44

3.9	Geometry involved in computing the overall $\phi$ limits of the solar radiation field, which occur at $\pm\phi_{max}$ where the light ray is emitted from and tangent to point $P$ on the Sun. Points $H$ , $G$ , and $J$ are the Sun center, geocenter, and satellite position, respectively. $K$ is the projection the Sun center onto the $\hat{e}_1$ - $\hat{e}_2$ plane. $R$ is the Sun-Earth distance, $R_\odot$ is the Solar radius, $r$ is the satellite-Earth distance, and $\omega$ is the Sun-satellite angle. . . . .	45
3.10	Geometry involved in slicing the Sun in $\phi$ to compute $\theta$ limits for non-zero $\phi$ angles and light ray angles of emission ( $\beta$ ). Points $H$ , $G$ , $E$ , and $D$ are the Sun center, geocenter, location of emission, and atmosphere-free satellite position, respectively. $R_\odot$ is the solar radius, $R$ is the geocentric distance to the Sun center, $r$ is the satellite-Earth distance, and $\bar{\omega}$ is the atmosphere-free Sun-satellite angle. Points $F$ and $M$ and angles $\epsilon$ and $\xi$ and are used in intermediate steps towards describing the non-zero $\phi$ geometry. Parameters with a prime ('') denote values in the non-zero $\phi$ plane corresponding to those in the $\phi = 0$ plane. . . . .	46
3.11	Flowchart for software implementation of the SOLAARS model. This process is repeated at each satellite position. . . . .	49
3.12	Density profiles for the standard atmosphere profiles used in the SOLAARS model. . . . .	50
3.13	Geometric parameters involved in modeling refraction. In this illustration, point $B$ is the vertex of refraction, $h_g$ is the light ray grazing height, $\psi$ is the angle of the light ray with respect to the local vertical, and $h_\psi$ is the height of the light ray at a particular $\psi$ angle. The angle $\psi_f$ is the final value of $\psi$ where the light ray has left the atmosphere at the atmosphere height ( $h_T = 50km$ ) and $\psi'_f$ is the value of $\psi$ which we use in the place of $\psi_f$ which is located at some height $h_f > h_T$ . The refractive height ( $S$ ) is the distance between the point $B$ and the light ray grazing point at the grazing height ( $h_g$ ). . . . .	51
3.14	Refraction angle ( $Re$ ) and refractive height ( $S$ ) profiles computed using each of the standard atmospheres used in the SOLAARS model. . . . .	53
3.15	Solar spectrals for light rays with different grazing heights. The initial, extraterrestrial spectrum and spectra computed with only Rayleigh scattering effects are included for comparison. . . . .	55
3.16	Geometric parameters involved in modeling extinction processes. $R_\oplus$ is the Earth radius, $h_T$ is the height of the top of the atmosphere (50 km), $s_T$ is the path distance from the grazing point to the top of the atmosphere, $h_g$ is the light ray grazing height, and $h_s$ is the height of a light ray at a path distance ( $s$ ) along the approximate light ray path. . . . .	57
3.17	Transmittances at different grazing heights. . . . .	58

3.18	Aerosol extinction coefficient profiles for each of the scenarios described in Table 3.1. . . . .	61
3.19	Extinction coefficient profiles for a two spectral bin model with a Visible/UV bin ( $\bar{L}_1$ ) and IR bin ( $\bar{L}_2$ ). Results are shown for each of the aerosol profiles described in Table 3.1. . . . .	62
3.20	HITRAN absorption cross section spectra used in the SOLAARS model. . . . .	63
3.21	Mixing ratios profiles for the five standard atmospheres used in SOLAARS. . . . .	64
3.22	Extinction coefficient profiles for a two spectral bin model with a Visible/UV bin ( $\bar{L}_1$ ) and IR bin ( $\bar{L}_2$ ). Results are shown for each of the standard atmospheres used in the SOLAARS model. . . . .	65
3.23	Zonal average cloud top heights from Lelli et al. (2011). . . . .	67
3.24	Comparison of SMARTS2 (Gueymard, 2001) and the results of our full modeling and modeling with only Rayleigh scattering for direct beam SSI. The extraterrestrial spectrum used from ASTM (2014) is shown as well. Note that these SSI spectra are smoothed to 50 nm resolution. The difference between the full SOLAARS model and SMARTS2 results is shown as well. . . . .	68
3.25	SOLAARS-CF geometric parameters. $\hat{R}$ is the geocentric unit vector pointing to the Sun and $\hat{E}$ is the unit normal to the ecliptic. The satellite position vector $\vec{r}$ is described in the curve fit SOLAARS approximation by its projection along the $\hat{R}$ direction ( $r_R$ ) and its remaining components in $\vec{r}_E$ . The component of $\vec{r}_E$ perpendicular to the ecliptic is $r_{E\perp}$ and the component parallel to the ecliptic is $r_{E\parallel}$ , which is scaled to compensate for Earth oblateness. . . . .	70
3.26	A constant slice of SOLAARS results for locations in a constant $r_R$ plane without Earth oblateness correction (a) and with the correction for flattening in the ecliptic (b). . . . .	71
3.27	SOLAARS attenuation factor data which is the basis of the SOLAARS-CF curve fit. . . . .	72
3.28	Comparison of SOLAARS-CF curve fit and SOLAARS SRP attenuation factor data being fit to in the $r_R=2000$ km slice. The three sigmoids, which correspond to the three hyperbolic tangent terms in Eq. 3.7.2, compose the SOLAARS-CF curve. . . . .	73
3.29	Curve fitting results for $a$ coefficients in each constant $r_R$ slice of the SOLAARS data and associated curve fits to the $a$ coefficients as a function of the $r_R$ distance. . . . .	74
3.30	SOLAARS results which are the basis for curve fitting (a) and curve fitting residuals (b). . . . .	75

3.31 Flowchart for SOLAARS-CF software implementation. . . . .	75
4.1 A photo of the GRACE satellites during integration from Doornbos (2012). . .	77
4.2 Illustration of the GRACE satellites in orbit from <a href="http://www.csr.utexas.edu/grace">http://www.csr.utexas.edu/grace</a> . .	77
4.3 GRACE A shadow function map for GRACE A for 2008 generated using SOLAARS-CF. . . . .	78
4.4 Comparison of GRACE A attenuation factors derived from accelerometer data and from the SOLAARS-CF model with and without Earth oblateness. . . .	79
4.5 Comparison of penumbra timing error results with and without Earth oblate- ness in SOLAARS-CF. . . . .	79
4.6 A SOLAARS solar radiation field dataset for a GRACE preumbra transition. Each frame in these plots is titled with the elapsed time in the penumbra transi- tion. These results were generated using the “low aerosol” profile from Table 3.1 and a cloudless (i.e. $h_{CT} = 0$ ) USS atmosphere. Results are separated into two plots, where (a) shows radiance and (b) shows the spectral composition of the solar radiation fields. . . . .	83
4.7 Typical example of a shadow exit of GRACE Satellite A on January 22, 2008. Accelerometer data and SRP modeling results from SOLAARS, SOLAARS- CF, and the model from Montenbruck and Gill (2000) are shown. . . . .	85
4.8 Typical example of a shadow exit of GRACE Satellite A on March 25, 2008. Accelerometer data and SRP modeling results from SOLAARS, SOLAARS- CF, and the model from Montenbruck and Gill (2000) are shown. . . . .	86
4.9 Accelerometer data and SRP modeling results from our precise model for 43 subsequent shadow entries of GRACE Satellite A on January 21-23, 2008. . .	89
4.10 Sensitivity of SRP modeling results to varying input conditions/methods: (a) standard atmosphere model, (b) cloud top height, (c) aerosol profile (see Table 3.1), (d) Earth radius, (e) number of light rays used ( $\mathbb{N}_R$ ), (f) comparison with the M&G 2000 model, and (g) comparison with modeling without effects ignored by Vokrouhlický et al. (1993). Note that “baseline case” in (e) and (f) refers to results from our full model using the USS atmosphere model, a 5.892 km cloud top height, mean Earth radius, medium aerosol profile, and 196 light rays. . . . .	91
4.11 Sensitivity of modeling results to the $\beta'$ orbit angle. This sensitivity is pre- sented as a $\Delta v$ integrated difference between the extrema of penumbra SRP accelerations (for a single transition on each date) modeled using the high and low aerosol profiles and between baseline SOLAARS and M&G 2000 results. (a) shows the $\Delta v$ results and (c) shows the magnitude of $\beta'$ orbit angles. . .	93

4.12 Comparison of penumbra transition limits. . . . .	94
4.13 Process for estimating the contribution of penumbra SRP to the flyby anomaly. We compute a penumbra SRP anomalous $\Delta v_\infty$ by comparing the hyperbolic excess velocities of the simulated pre-encounter and post-encounter OD solutions at each time step. . . . .	97
4.14 SOLAARS-CF, full SOLAARS, and M&G 2000 penumbra SRP modeling results for a) 1990 Galileo, b) Cassini, and c) Juno Flybys. Note that the full SOLAARS was not used in propagation of any the trajectories, but was applied to the trajectory solution from SOLAARS-CF for comparing SRP acceleration results. . . . .	99
4.15 Anomaly error estimate ( $\sigma_{v_\infty}$ ) and $\Delta v_\infty$ results for 1990 Galileo Flyby. . . . .	101

# List of Tables

1.1	Atmospheric interaction characteristics of bands of the solar spectrum from Thomas and Stamnes (2002). In the second column, $\lambda$ is wavelength. . . . .	7
3.1	Parameters used to generate the aerosol extinction profiles used here, based on data from Jursa (1985). “Background” refers to background stratospheric, i.e. an atmosphere with negligible volcanic aerosols. Seasons specified in the table are for the USS atmosphere case, and for other standard atmosphere cases the corresponding season is chosen (e.g. fall/summer is used with the sub-arctic summer standard atmosphere). . . . .	61
3.2	Curve fitting formulas for computing the $a$ coefficients which capture $r_R$ dependence of penumbra SRP. Note that these curve fitting formulas are evaluated with the distance $r_R$ in units of $10^6$ meters. . . . .	73
4.1	Data from past Earth flyby anomalies up to MESSENGER (labeled MSGR) from Anderson et al. (2008) and recent Juno $\Delta v_\infty$ and $\sigma_{v_\infty}$ values are from Thompson et al. (2014). Note that the majority of observed anomalous $\Delta v_\infty$ values are at least an order of magnitude greater than the estimated errors in hyperbolic excess velocities. The Juno spacecraft mass used here is from NASA (2011) and is a beginning of mission value. . . . .	96
4.2	Estimated penumbra SRP anomalous $\Delta v_\infty$ contributions and estimated error in these contributions ( $\sigma_{v_\infty}$ ). The time spent in penumbra ( $\Delta t_p$ ) and full sunlight SRP acceleration magnitude ( $a_{SRP}$ ) are included to illustrate their correlation with anomaly results. . . . .	101

# Chapter 1

## Introduction

### 1.1 Solar radiation pressure

Solar radiation pressure (SRP) is one of the major non-gravitational forces acting on space-craft, both for Earth orbiters and solar system missions. For Earth orbiters, SRP can be the most significant non-gravitational force above an orbit altitude of roughly 650 km, when atmospheric drag forces become smaller than SRP forces due to decreasing atmospheric density; however, this altitude boundary is dependent on the numerous factors that determine atmospheric drag and SRP accelerations. SRP accelerations depend on:

1. The intensity, direction, and spectral composition of the local solar radiation field
2. The geometry, attitude, mass, and optical properties of the object in orbit

The dependence of SRP on these factors is explained by the physics that drive solar radiation pressure.

To understand the fundamental physics of SRP, we can begin with the particle model of electromagnetic radiation, where the solar radiation field incident on a satellite is composed of a finite number of photons. These photons are traveling at the speed of light and, while they have no mass, they do have momentum ( $p$ ):

$$p = \frac{h_p}{\lambda} \tag{1.1}$$

where  $h_p$  is Planck's constant and  $\lambda$  is wavelength. Since photons have momentum, when they strike a surface of an object, they exchange momentum with that object. According to Newton's Third Law, the momentum transferred to the object is equal and opposite to the momentum change of the photon. The object's mass determines its acceleration due to this

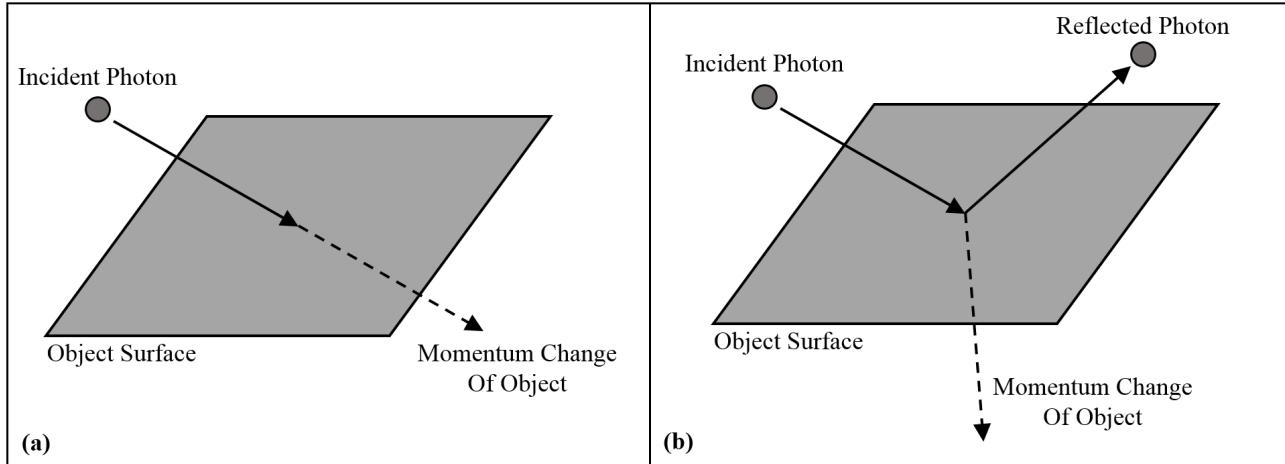


Figure 1.1: Geometry of photon momentum transfer for absorbed (a) and reflected (b) photons. A reflected photon results in a different direction and magnitude of momentum transferred to the object.

change in momentum. If the photon is absorbed by the surface it strikes, then the object acceleration will occur in the direction of the incident photon, as illustrated in Fig. 1.1a. If the photon is reflected, as illustrated in Fig. 1.1b, then the change in momentum of the photon is very different. In fact, when the photon is incident and reflected perpendicular to the surface, the resulting momentum change of the object (i.e. SRP acceleration) is twice as large as if the photon were absorbed.

When a photon is reflected, both the orientation of the object surface and direction of the incident photon path influence the direction and magnitude of the SRP acceleration. The object geometry and attitude determine the orientation of the particular surface struck by the photon. The optical properties of the surface and the wavelength of the incident photon determine whether the photon is reflected and in what direction. These optical properties are the same ones that determine the varying visual appearance (i.e. color, brightness, texture) of objects to the human eye. For modeling of SRP accelerations, the probability of photon reflection (i.e. the surface optical properties) and the direction of reflected photons is usually described on a macroscopic scale where the entire solar radiation field is treated as a single light ray.

For a macroscopic description of surface interactions, surface optical properties are measured to describe what fraction of incident photons will be reflected in a particular way. The small scale geometry, or texture, of a surface and its material properties determine the angular distribution of reflected photons. A rough surface texture or material that allows light to partially enter its internal structure and exit in random directions leads to diffuse reflections (corresponding to a matte appearance). A smooth surface texture and material that does not allow light to enter leads to specular reflections (corresponding to a mirrored appearance).

For a macroscopic description of the incident solar radiation field, we use mean solar radiance and normalized solar spectral irradiance. Mean solar radiance describes the total photon momentum incident on the object. The normalized solar spectral irradiance describes the spectral distribution of incident photons. Along with surface optical properties, this spectral distribution of incident light determines what fraction of the sunlight will reflect from the object and how it will reflect (i.e. in what directions).

The spectral distribution of sunlight is easily modeled for the majority of the orbit of any Earth satellite. In full sunlight, the sunlight reaching a satellite or other object in Earth orbit can be accurately approximated as a point source with a constant radiance and spectral composition. However, during Earth penumbra transitions, a point source approximation is no longer accurate.

During penumbra transitions, the solar image is rising or setting from the perspective of the object in orbit, and sunlight is passing through the atmosphere en-route to penumbra. The transfer of radiation through the lower atmosphere (below 50 km) leads to significant changes in the shape of the local solar radiation field and the distribution of radiance and spectral composition in the solar image. The time a satellite spends in penumbra each orbit is presented as a function of orbit altitude in Fig. 1.2. These results are generated using the SOLAARS-CF model and, to isolate the influence of orbit altitude, each data point is generated for a circular orbit in the ecliptic. These results show that penumbra solar radiation pressure modeling can be important in all orbit regimes, and that beyond low Earth orbit (LEO), time spent in penumbra increases with orbit altitude.

## 1.2 Earth oblateness

The irregular shape of the Earth is well documented. This irregular shape is primarily of concern to orbit modelers because of the resulting irregularities in the Earth gravity field. By far the most dominant irregularity is polar flattening. This flattening causes the the J2 gravitational perturbation, which refers to the second zonal term in a spherical harmonic model of the geopotential. Polar flattening is reflected in the WGS84 reference ellipsoid, which is an oblate spheroid with a polar radius of  $R_{\oplus p} = 6356752$  m and equatorial radius of  $R_{\oplus e} = 6378137$  m (NIMA, 2000).

The oblate shape of Earth is important in penumbra SRP modeling because it influences the location and curvature of the horizon for a satellite. The most significant effect is in the timing of penumbra transitions. A smaller Earth radius, closer to the polar radius ( $R_{\oplus p}$ ) results in an earlier sunrise penumbra transition, and an Earth radius closer the equatorial value ( $R_{\oplus e}$ ) results in a later sunrise. The influence of oblateness on penumbra SRP is illustrated in Fig. 1.3, where a light ray is from the sun strikes the satellite in orbit. The dashed circle represents a spherical model of Earth with a radius equal to the equatorial radius of the more precise, oblate spheroid model. The spherical model would result in the

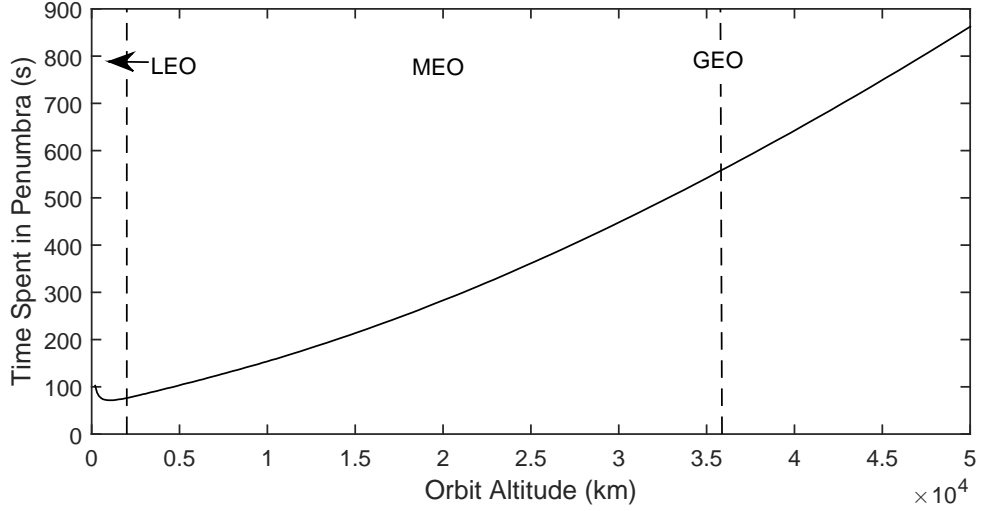


Figure 1.2: Time spent in penumbra during each orbital period as a function of circular orbit altitude. Orbits are in the ecliptic plane and simulations are carried out using the SOLAARS-CF model described in Section 3.7. Note that due to the orbit-Sun geometry assigned to each orbit, these results represent the minimum time spent in penumbra at each altitude.

light ray not striking the satellite and contributing to SRP acceleration of the satellite.

The simple scenario illustrated in Fig. 1.3 effectively demonstrates the influence of Earth oblateness on penumbra SRP. However, atmospheric refraction and extinction are the main drivers of penumbra SRP. Therefore, the effect of oblateness is primarily in how it affects the position of the atmosphere, which varies as a function of altitude above the oblate solid Earth.

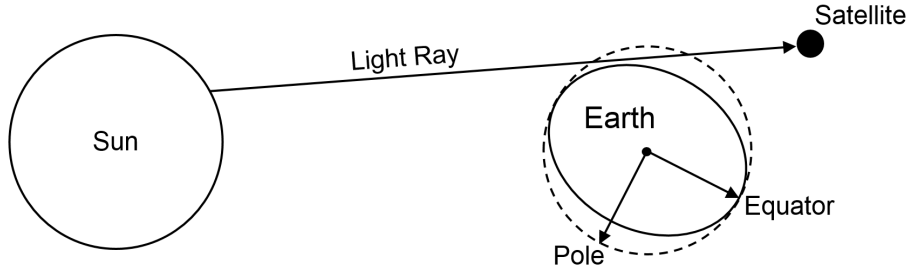


Figure 1.3: Geometry of a light ray passing Earth to strike a satellite in orbit. The dotted line represents a spherical model of Earth that would incorrectly lead one to determine that the light ray is blocked.

## 1.3 Atmospheric radiative transfer

The primary challenge in physically modeling penumbra solar radiation fields is modeling the influence of the atmosphere. As a result, the majority of Chapter 3 is concerned with atmospheric radiative transfer modeling in SOLAARS, which can be separated into two distinct effects: refraction and extinction. While the resulting light ray geometries are complex, the concept of atmospheric refraction is relatively simple: spatial variations in the refractive index of the atmosphere, driven primarily by the exponential decay of density with altitude, leads to refraction of light rays. Decreasing refractive index with altitude in the lower atmosphere means that solar light rays are bent towards the geocenter. As modeling results will show in later sections, interaction of sunlight with the atmosphere above the stratosphere at about 50 km altitude are negligibly small for SRP modeling. Therefore, refraction of light rays away from the geocenter due to increasing refractive index with altitude in the ionosphere is not considered.

In contrast to the simpler concept of refraction, atmospheric extinction modeling includes numerous scattering and absorption processes which exhibit complex spectral behavior. A description of the solar spectral distribution of sunlight is required to model the influence of these extinction processes. As shown in Fig. 1.4, the extraterrestrial solar spectral irradiance (with units of power per unit area per unit wavelength) is roughly that of a black body at 5778 K. An extraterrestrial spectrum is the starting point for atmospheric extinction modeling and is modified as its radiation passes through the atmosphere and interacts with the various constituent gasses and suspended particles (aerosols), both liquid and solid.

The variability of solar spectral irradiance and the interaction of sunlight with atmospheric constituents are summarized in Table 1.1. Solar variability is most significant in the higher energy, low wavelength spectral bands. As shown in Fig. 1.4, these  $<200\text{ nm}$  bands which exhibit significant variability account for a very small fraction of the total solar irradiance, which is the wavelength integrated solar spectral irradiance. Since SRP accelerations roughly scale with total solar irradiance, the effect of these total solar irradiance variations on SRP is usually less than 1%.

It is necessary to make a clear distinction between the two extinction processes being addressed in the SOLAARS model: scattering and absorption. The combined effect of these two processes is called extinction, and both of these processes attenuate the power of a given beam of radiation from the Sun, but do so through different mechanisms. Absorption of radiation by molecules is described using quantum mechanics, where the energy of photons is exchanged with molecules when collisions occur. Conversely, scattering is explained using the wave theory of light, where the energy of photons is redirected due to larger scale interactions with light. As shown in Fig. 1.5 from McCartney (1976), the behavior of scattering is highly dependent on the ratio of the wavelength of the radiation to the size of the particles. As a result, scattering is categorized and described differently according to this ratio. Rayleigh scattering occurs when the particle is much smaller than the wavelength, and

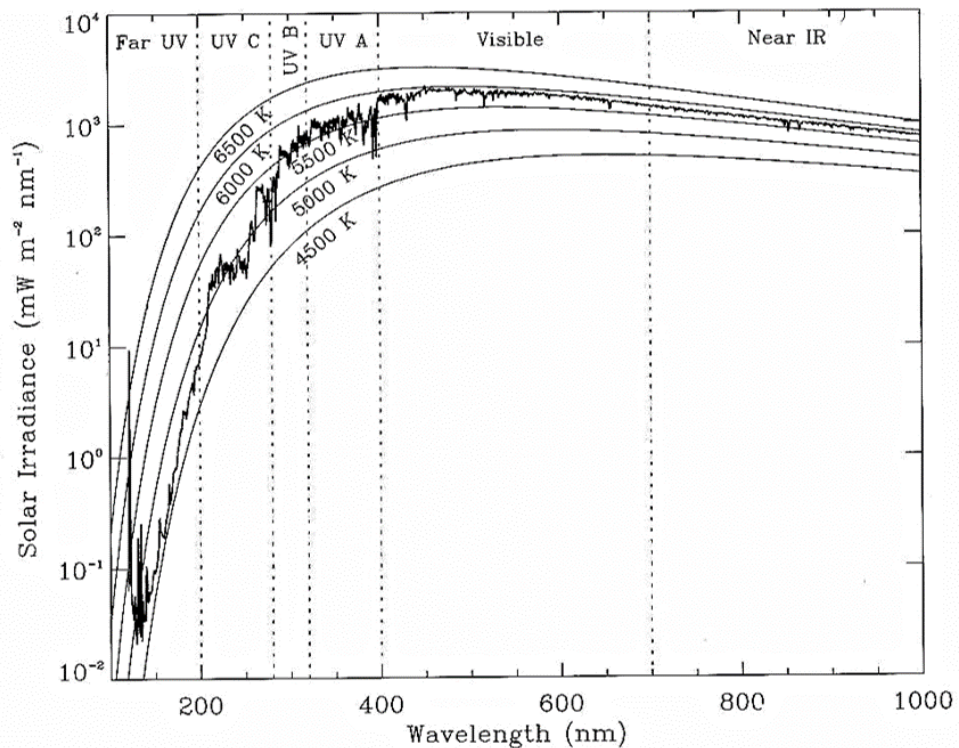


Figure 1.4: Extraterrestrial solar spectral irradiance and with blackbody irradiances at various temperatures from Thomas and Stamnes (2002). These curves illustrate how the extraterrestrial solar spectrum can be approximated as a blackbody spectrum. The spectral subranges are indicated by the vertical, dotted lines.

Table 1.1: Atmospheric interaction characteristics of bands of the solar spectrum from Thomas and Stammes (2002). In the second column,  $\lambda$  is wavelength.

Band	Range	Solar variability	Comments
X rays	$\lambda < 10 \text{ nm}$	10-100%	Photoionizes all thermosphere species.
Extreme UV	$10 < \lambda < 100 \text{ nm}$	50%	Photoionizes O <sub>2</sub> and N <sub>2</sub> . Photodissociates O <sub>2</sub> .
Far UV	$100 < \lambda < 200 \text{ nm}$	7-80%	Dissociates O <sub>2</sub> . Discrete electronic excitation of atomic resonance lines.
Middle UV	$200 < \lambda < 280 \text{ nm}$	1-2%	Dissociates O <sub>3</sub> in intense Hartley bands. Potentially lethal to biosphere.
UV-B	$280 < \lambda < 320 \text{ nm}$	<1%	Some radiation reaches surface, depending on O <sub>3</sub> optical depth. Responsible for skin erythema.
UV-A	$320 < \lambda < 400 \text{ nm}$	<1%	Reaches surface. Benign to humans. Scattered by clouds, aerosols, and molecules.
Visible	$400 < \lambda < 700 \text{ nm}$	$\leq 0.1\%$	Absorbed by ocean, land. Scattered by clouds, aerosols, and molecules. Primary energy source for biosphere and climate system.
Near IR	$0.7 < \lambda < 3.5 \mu\text{m}$		Absorbed by O <sub>2</sub> , H <sub>2</sub> O, CO <sub>2</sub> in discrete vibrational bands.
Thermal IR	$3.5 < \lambda < 100 \mu\text{m}$		Emitted and absorbed by surfaces and IR-active gases.

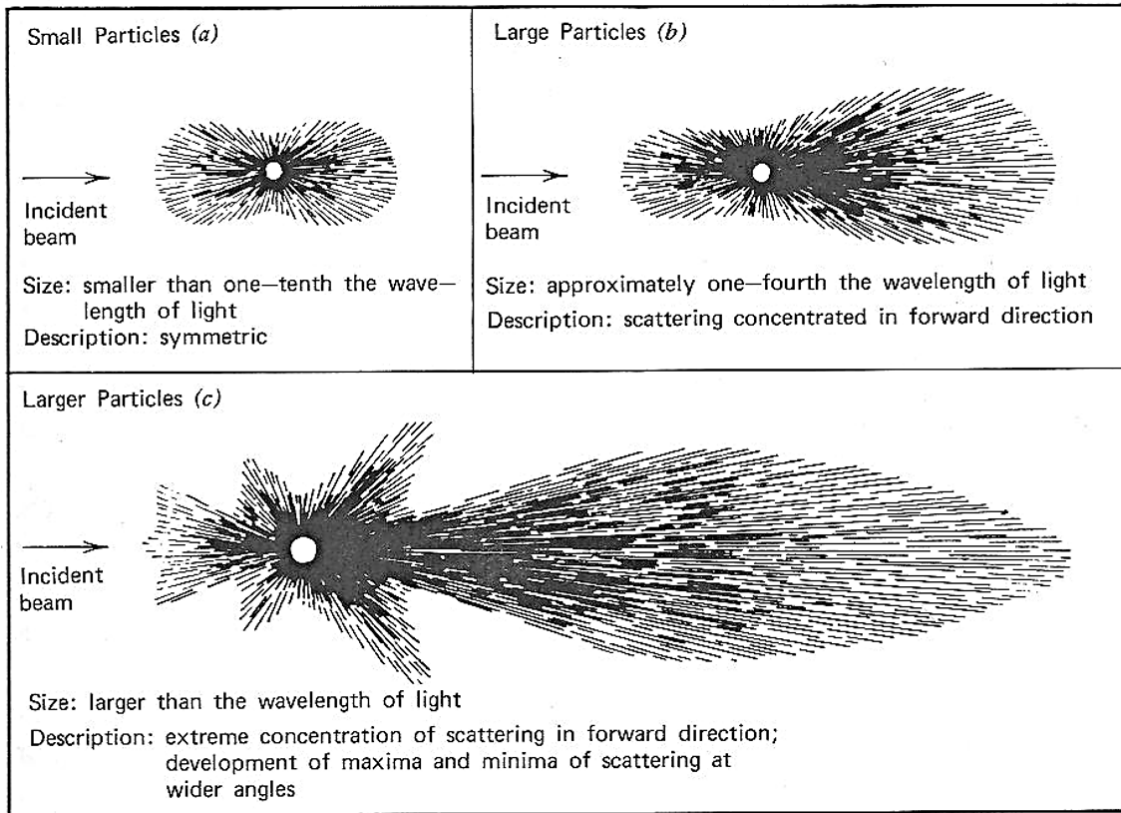


Figure 1.5: Scattering patterns for various particle sizes from McCartney (1976). Note the symmetry of the Rayleigh scattering case with a small particle shown in section (a). The complex patterns of scattering with larger particles shown in sections (b) and (c) require the more complex Mie scattering theory.

this type of scattering results in roughly equal amounts of radiative flux in the directions of incidence and transmission as shown in section (a) of Fig. 1.5. Mie scattering theory is used when the particles are greater than one tenth of the wavelength of incident radiation, and this theory is based on the processes of reflection, refraction, and diffraction. In addition to the texts cited to this point in this section, Irvine (1975) gives a comprehensive treatment on the basics of modeling absorption and scattering in the atmosphere which introduces much of the mathematical basis for atmospheric radiative transfer codes (RTCs).

There are three fundamental inputs used to model radiative transfer in the atmosphere:

1. Extraterrestrial solar spectral irradiance
2. Atmosphere models
3. Spectroscopic parameters

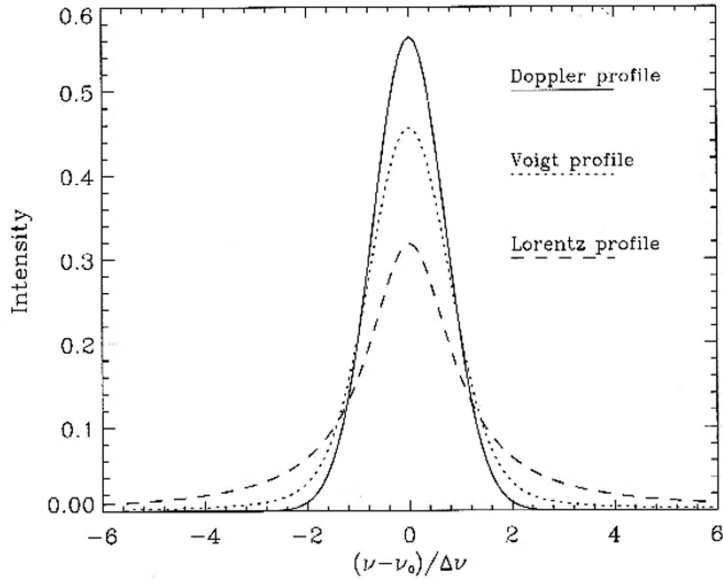


Figure 1.6: A comparison of normalized line broadening profiles from Thomas (1999). In this plot,  $\nu$  is frequency and  $\Delta\nu$  is the Doppler width for the Doppler and Voight profiles and the Lorentz width for the Lorentz profile.

As previously mentioned, the extraterrestrial solar spectral is necessary for describing the spectral composition and intensity of incident radiation on the atmospheric medium. A complete atmosphere model including temperature, pressure, and concentrations of various gases, aerosols, and other particles is used to describe the probability of light interacting with atmospheric constituents along its path in the atmosphere.

In many RTCs, spectral lines are defined to describe the attenuation of radiation by molecules in the atmosphere for its various molecular constituents. The molecules are modeled as damped harmonic oscillators to accurately model their interaction cross sections and assign a physically accurate attenuation profile associated with each molecular species. Lorentz line broadening is used to model broadening of the spectral lines due to pressure effects, Doppler broadening is used to account for thermal effects, and the net result of these two broadening profiles is described by the Voigt profile. This Voigt profile is simply a convolution of the Doppler and Lorentz line broadening profiles that describe the distribution of intensity for each spectral line. Examples of these three profiles are shown in Fig. 1.6, where  $\nu_0$  is the frequency of the spectral line.

## 1.4 Problem statement and motivation

The goal of this work is to develop a new, highly physical and accurate penumbra solar radiation pressure model that builds upon past work by:

1. Presenting the complex light ray geometries in a more intuitive way, with complete derivations for all geometric parameters
2. More precise modeling of the atmospheric effects which drive penumbra SRP
3. Tabulating parameters describing atmospheric effects to significantly reduce computational cost
4. Validating modeling results using comparisons with high-precision satellite accelerometer data and a typical penumbra SRP model
5. Characterizing the sensitivity of penumbra SRP to key parameters that drive the model
6. Developing a simple, fast model based on results from our complex, high accuracy SOLAARS model

A more practical high-precision penumbra SRP model is particularly relevant now, in light of a continued desire for more precise orbit determination and reduction of high-precision satellite accelerometer data. Some missions such as the low Earth orbiters Challenging Minisatellite Payload (CHAMP), Gravity Recovery and Climate Experiment (GRACE), and Gravity and Steady-State Ocean Circulation Explorer (GOCE), are equipped with very sensitive, triaxial accelerometers observing the total of all non-gravitational forces acting on the satellites (Reigber et al. 1999, Tapley et al. 2004, ESA 1999). This includes the effects of solar and Earth radiation pressure as well as residual atmospheric drag, thermospheric winds, and effects of the attitude control system. For these missions, the accelerometer observations can replace modeling of non-gravitational accelerations. Modeling, however, is still required in case of sensor outages, or if one wants to separate the individual non-gravitational contributions (e.g., to determine drag acceleration and thermospheric densities and winds (Tapley et al. 2007, Doornbos et al. 2010)). Our model could be used to more accurately remove the contribution of solar radiation pressure from accelerometer observations, and improve estimation of thermospheric winds and densities.

As Vokrouhlický et al. (1993) point out, the effectiveness of the simple shadow functions typically used in penumbra solar radiation pressure modeling is limited because they are not informed by the key physical processes involved in penumbra SRP. The properties of solar radiation reaching Earth's penumbra are driven by refraction and extinction in Earth's lower atmosphere. In principle, the situation is related to sunrise and sunset observed on the surface of Earth. However, as light rays reaching a satellite in penumbra travel a much longer path

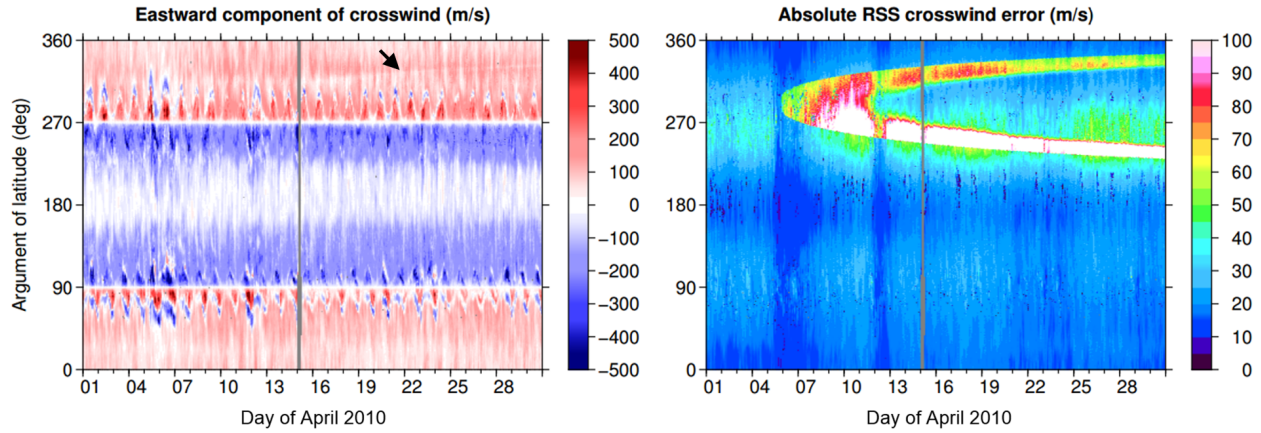


Figure 1.7: Eastern component of crosswind derived from processing on GOCE accelerometer data and associated error estimates from Doornbos (2014). The high error region corresponds to GOCE penumbra, and the faint white line pointed out in the upper, red region of the data represents processing errors due to mismodeling of penumbra SRP.

through the atmosphere than those reaching the surface of Earth, the effects of refraction and extinction are much stronger. Refraction shifts the timing of the penumbra transition, and influences its duration. In addition to these timing effects, refraction causes beam divergence, reducing the amount of sunlight reaching penumbra. Atmospheric extinction due to absorption and scattering in the atmosphere further reduces the intensity of the sunlight and changes its spectral composition. Nearly all of the SRP change in penumbra is caused not by shadowing from the solid Earth but rather by the atmosphere, primarily through atmospheric refraction and extinction of the light rays. These atmospheric effects reduce SRP to near zero when the solar disc as seen from the satellite does not even touch the solid Earth. This is particularly interesting, as atmospheric effects are generally disregarded in penumbra SRP modeling.

According to the data user manual for GOCE wind and density retrieval (Doornbos, 2014), there is a 35% increase in GOCE SRP modeling errors when the satellite is close to penumbra transitions. These SRP modeling errors contribute most significantly to wind retrieval errors. The GOCE crosswind data shown in Fig. 1.7 illustrate the need for more precise penumbra SRP modeling. The faint streak in the upper region of the crosswinds retrieved from GOCE accelerometer data follows the GOCE penumbra region. This streak in the wind data indicates that SRP is not being accurately removed from accelerometer data during penumbra transitions, leading to aliasing of the SRP accelerometer signal onto the density and wind accelerations.

According to Doornbos (2014), in addition to penumbra SRP modeling errors contributing significantly to wind errors throughout the GOCE mission, these errors significantly influence density retrieval from the early phase of the GOCE mission. Early in the mission, GOCE was at higher altitudes, when drag accelerations were lower, and therefore closer to SRP ac-

celerations. The significance of penumbra SRP modeling errors in wind and density retrieval for GOCE is particularly strong motivation for an improved model. The exceptionally low altitude of the GOCE orbit (between 250 and 300 km for the majority of the mission) leads to higher drag accelerations and limits the significance of SRP modeling errors. These same penumbra SRP modeling errors can make it impossible to accurately retrieve crosswinds in penumbra from satellite missions at higher altitudes like CHAMP and GRACE (Doornbos, 2012).

In this dissertation, the target of SRP modeling is generally called “the satellite,” however our model can be applied to any object in Earth’s penumbra. Any application where very precise orbit determination is important (e.g., GPS, collision avoidance, and debris propagation) could benefit from the improved SRP force modeling offered by a highly physical approach. McMahon and Scheeres (2010) note the potential for significant secular contributions to orbit dynamics from asymmetric penumbra transitions which exhibit different behavior upon umbra entry and umbra exit. Traditional penumbra SRP models cannot capture these asymmetries because they assume a spherical, atmosphere-free Earth. The SOLAARS model presented here could be used to accurately quantify the significance of these asymmetries.

Although they did not apply a highly physical penumbra SRP model in their investigation, Hubaux et al. (2012) presents a study of the effect of several penumbra SRP models on accurate space debris orbit propagation. The results of this study, shown in Fig. 1.8, indicate that penumbra SRP modeling has some influence on the evolution of the orbital elements of a debris object. The penumbra SRP models being compared in Fig. 1.8 are applied to a high area-to-mass ratio (HAMR) debris object, which results in increased sensitivity to SRP. Due to this increased sensitivity to SRP, the results indicate some sensitivity to penumbra SRP modeling even though the models tested do not exhibit the asymmetries noted by McMahon and Scheeres (2010). Unfortunately, none of the three models being compared in Hubaux et al. (2012) are informed by the dominant physical processes driving penumbra SRP. The SOLAARS or SOLAARS-CF models could be used to more accurately study the significance of penumbra SRP modeling in long-term orbit dynamics by providing an accurate standard for comparison with simpler, computationally efficient alternatives.

## 1.5 Organization of Dissertation

This dissertation is organized to present the material in a simple and familiar format. Chapter 2 presents a review of literature on the key topics for each aspect of the models presented here. Chapter 3 presents the theory and modeling behind the SOLAARS and SOLAARS-CF penumbra SRP models. Chapter 4 includes results from two studies carried out using the SOLAARS and SOLAARS-CF models. These studies serve to validate the models, characterize their sensitivity to various inputs, and demonstrate improvements over typical models. Finally, Chapter 5 summarizes the conclusions from this work and suggests topics for future work in penumbra SRP modeling.

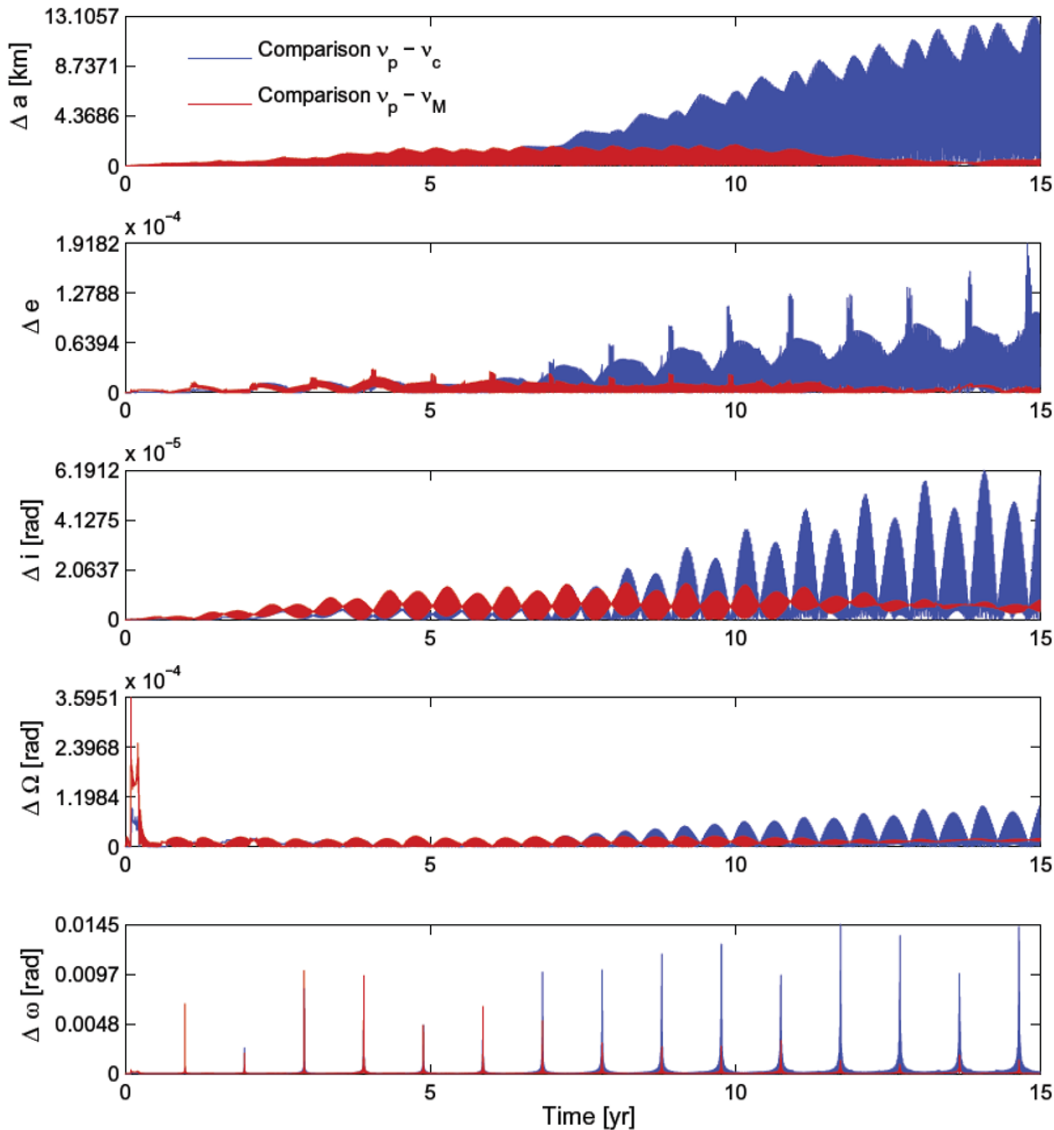


Figure 1.8: Absolute difference in orbital elements for a debris object ( $20 \text{ m}^2/\text{kg}$  area-to-mass ratio) in the geosynchronous orbit regime propagated with different pnemubra SRP models from Hubaux et al. (2012). In the legend,  $\nu_p$  is the new shadow function presented by Hubaux et al. (2012),  $\nu_c$  is a cylindrical shadow function, and  $\nu_M$  is the shadow function that appears in Montenbruck and Gill (2000).

# Chapter 2

## Review of Relevant Literature

### 2.1 Penumbra SRP modeling

Kozai (1961) and Wyatt (1961) first recognized and addressed the influence of eclipses on SRP and posed formulas for considering its influence on orbits. They used a discontinuous step function for penumbra transitions, and this simple approach persisted until Ferraz-Mello (1964, 1972) introduced a continuous shadow function, having a value of 0 in shadow and 1 in full sunlight. Since Ferraz-Mello introduced this continuous shadow function, numerous investigators have implemented their own shadow functions. As was the case for Ferraz-Mello, investigators often select the shadow function to exhibit a basic, smooth behavior but primarily are concerned with the mathematical properties required to fit their orbit integration schemes (e.g. Lála and Sehnal 1969, Lála 1971, Hubaux et al. 2012).

These simple shadow functions are defined as a function of geometric parameters describing the relative positions of the Earth, Sun, and satellite. The shadow function presented in Hubaux et al. (2012) is a function of the angle between the satellite and Sun geocentric position vectors illustrated in Fig. 2.1 (bottom). The bottom part of 2.1 shows the shadow cones bounding the penumbra region in the models presented by Hubaux et al. (2012) and Montenbruck and Gill (2000), and the top part of this figure shows the cylindrical umbra region which is assumed for a discontinuous step model of penumbra SRP. To attain a function which mathematically functions within an efficient, symplectic orbit integration scheme, Hubaux et al. (2012) uses a hyperbolic tangent sigmoid (s-shaped) shadow function with a scaling parameter that ensures that the width of the 0-1 sigmoid curve equals the time spent traversing the penumbra region illustrated in Fig. 2.1 (bottom). This hyperbolic tangent shadow function ( $\nu_p$ ) is compared with the cylindrical model ( $\nu_c$ ) and shadow function from Montenbruck and Gill (2000) in Fig. 2.2.

Unlike the somewhat arbitrary shadow function used in Hubaux et al. (2012), the shadow function which appears in Montenbruck and Gill (2000), which we will describe as the M&G

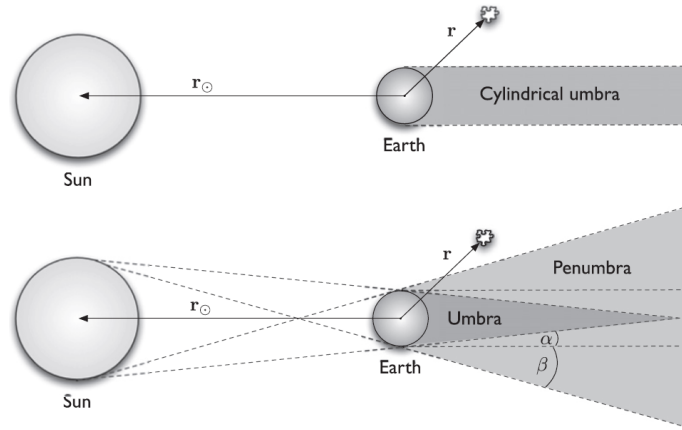


Figure 2.1: Geometry of atmosphere-free penumbra shadow cones and cylindrical shadow model from Hubaux et al. (2012).

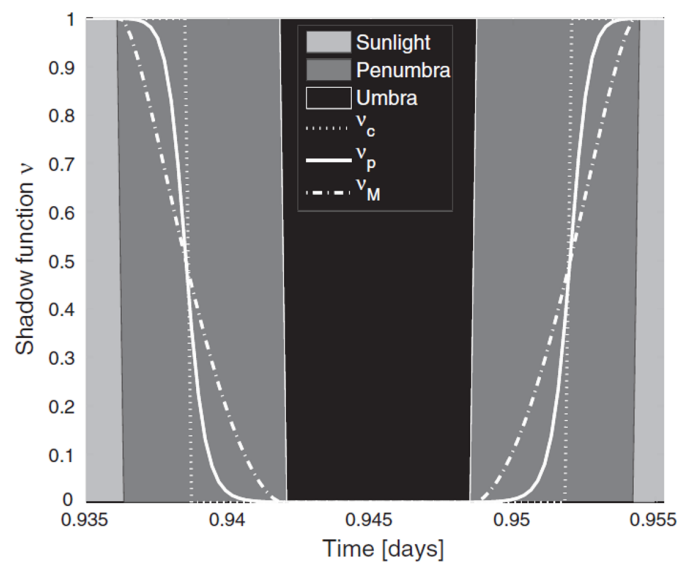


Figure 2.2: Comparison of shadow functions from Hubaux et al. (2012). In the legend,  $\nu_p$  is the new shadow function presented by Hubaux et al. (2012),  $\nu_c$  is a cylindrical shadow function, and  $\nu_M$  is the shadow function from Montenbruck and Gill (2000).

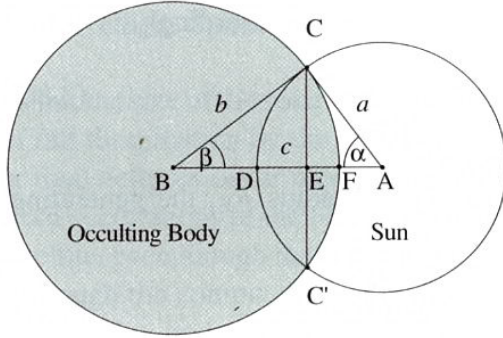


Figure 2.3: Geometry involved in the M&G 2000 penumbra SRP shadow function (image from Montenbruck and Gill (2000)). The geometric parameters here are used to compute the shadow function value, which is simply the visible area of the solar disc from behind the atmosphere-free occulting body divided by the total area of the disc.

2000 model, does have a physical basis. The M&G 2000 shadow function is defined based on the area of the solar disc visible from the satellite’s perspective. The geometry involved in computing this shadow function is illustrated in Fig. 2.3. The M&G (2000) shadow function is simply the area of the white, visible region of the solar disc in Fig. 2.3 divided by the total solar disc area. Although this definition of the shadow function is informed by some physical model of penumbra solar radiation, it assumes an atmosphere-free occulting body. For a planet with a sufficiently dense atmosphere like Earth, the primary drivers of penumbra SRP effects are atmospheric refraction and extinction.

Link (1962) first addressed the atmospheric effects that are key to physically representative penumbra SRP modeling. Kabeláč (1988) built on this work with a simplified approach, and, finally, Vokrouhlický et al. (1993) presented the most recent, highly physical approach, where the complex solar radiation fields in Earth penumbra are modeled with refraction and Rayleigh scattering by an atmosphere with vertically changing density. In their procedure, the solar radiation field is divided and treated as the sum of a finite number of light rays. The path and radiance of each light ray is modeled separately, and the SRP acceleration is computed as the sum over all light rays. In Vokrouhlický et al. (1994), the same authors present an approximate version of their model which is still quite complex and computationally intensive compared to typical penumbra SRP models. Fig. 2.4 shows modeled SRP accelerations from Vokrouhlický et al. (1993) for the LAGEOS satellite. This figure includes results from their model, a cylindrical shadow model, and an atmosphere-free model. This comparison of LAGEOS penumbra SRP modeling results illustrates the significant influence of atmospheric effects.

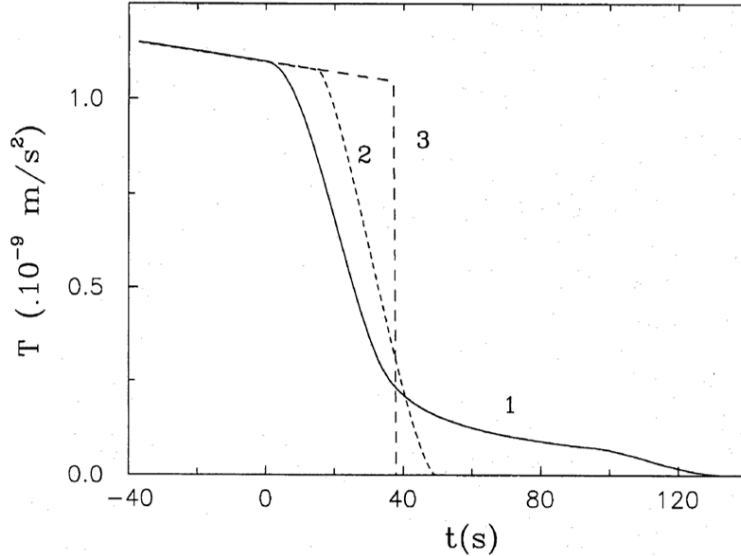


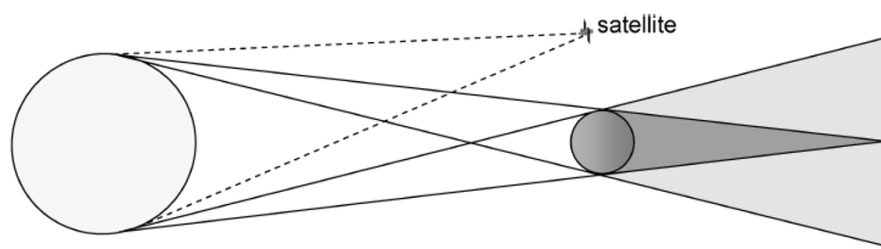
Figure 2.4: Sunset penumbra SRP accelerations (denoted  $T$  here) from Vokrouhlický et al. (1993) illustrating the significance of atmospheric effects. Curve 1 shows results from their model, Curve 2 shows the results of an atmosphereless model equivalent to the M&G 2000 model, and Curve 3 is a cylindrical shadow, step approximation to the transition.

## 2.2 Earth oblateness and penumbra SRP

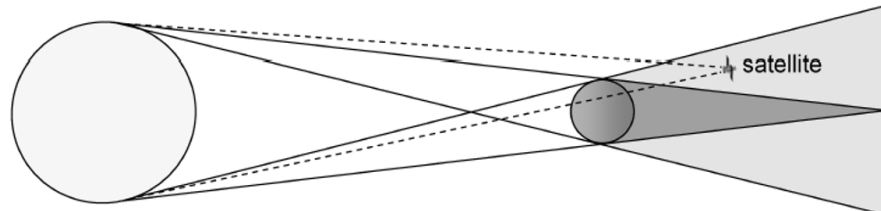
The influence of the oblate shape of Earth is a much simpler effect to consider in penumbra SRP modeling than the influence of the atmosphere. Regardless of its relative simplicity, Earth oblateness is generally disregarded and, as Adhya et al. (2004) points out, surprisingly little work has been done to integrate its effect into models. As is the case for penumbra SRP modeling in general, past work seems to lie at two extremes of complexity and computational cost.

Adhya et al. (2004) presents a relatively simple method for determining the SRP phase of a satellite while considering the oblate shape of Earth. The possible phases of SRP, as illustrated in Fig. 2.5, are full, penumbra, and umbra. In this method, the goal is to determine whether there are intersections between the dotted lines in Fig. 2.5 and the solid Earth. If none of the lines intersect, then the satellite is in full sunlight; if two intersect, then the satellite is in umbra; and if only one of the lines intersect, then the satellite is in penumbra.

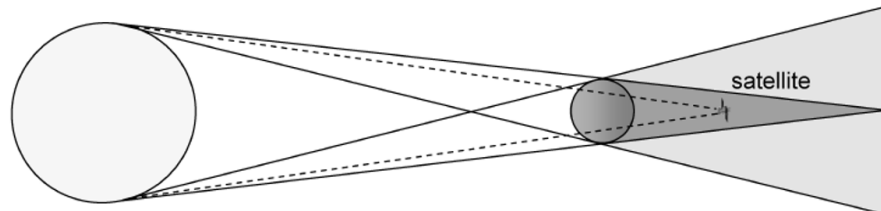
At a given satellite position, it is possible to describe each of the two dotted lines in Fig. 2.5 and the oblate spheroid representation of the surface of Earth with equations in three-dimensional space. Substituting the equation of one these dotted lines into the equation of the oblate spheroid yields a quadratic whose solution is an intersection point. If there is a real solution to this quadratic, then there is an intersection. One simply needs to check



a) Full phase: no lines intersect



b) Penumbra: one line intersects



c) Umbra: both lines intersect Earth

Figure 2.5: Geometry of penumbra phases (full phase, pnumbra, and umbra) from Adhya et al. (2004). The phase is determined by the number of intersections between the dotted lines connecting the satellite to the solar disc limits and the Earth spheroid.

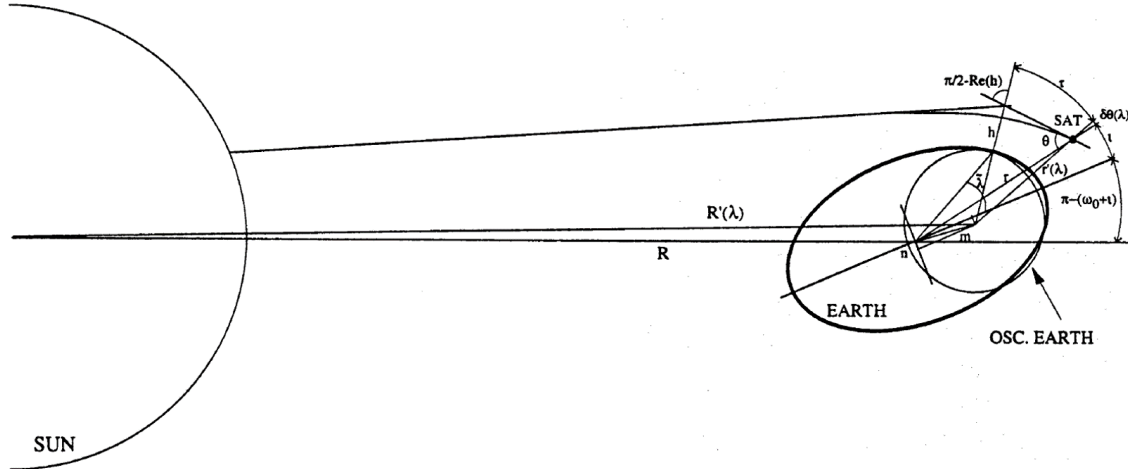


Figure 2.6: Geometry from Vokrouhlický et al. (1996) of the osculating spherical Earth used to approximate the oblate Earth. The satellite is at the position labeled “SAT”. The light ray grazing point, which is the point on Earth which the ray passes closest to, lies along the line dimensioned  $h$ . The spherical, osculating Earth is positioned and assigned a radius so that it is: (1) tangent to the oblate spheroid Earth at the grazing point and (2) matches the radius of curvature of the oblate Earth at the grazing point in the Sun-Earth-satellite plane.

(for each of the two dotted lines) these quadratic terms for a real solution to determine the SRP phase of the satellite. Comparisons to Envisat photometry data in Adhya et al. (2004) illustrate the significant eclipse timing error reduction (> 50%) when using an oblate spheroid instead of a sphere to approximate the shape of Earth.

As a refinement of their earlier work on highly physical penumbra SRP modeling, Vokrouhlický et al. (1996) integrate Earth oblateness into the formulas from Vokrouhlický et al. (1994). In this method, the authors define an osculating spherical Earth by a radius and new geocenter position for each light ray as illustrated in Fig. 2.6. The aim of their approach is to position and size a spherical Earth which best approximates the area of Earth and atmosphere around each light ray’s grazing point, which is the point on Earth’s surface nearest to the light ray path. This osculating sphere matches the radius of curvature of the oblate Earth (in the Earth, Sun, satellite plane) at the grazing point of the light ray being addressed and is positioned such that it is tangent to the oblate Earth at the grazing point. This definition of an osculating spherical earth is mathematically integrated into all of the formulas from their 1994 paper to model each light ray with its own spherical Earth and spherically stratified atmosphere.



Figure 2.7: Photograph taken by astronaut Scott Carpenter from the MA-7 orbiter from Cameron et al. (1963). Note the significant compression of the solar disc due to atmospheric refraction.

## 2.3 Atmospheric refraction

The somewhat complex analytic method from Garfinkel (1967) is used by Vokrouhlický et al. (1993) for penumbra SRP modeling. This model is based on the 1962 Standard Atmosphere. Garfinkel developed his earlier 1944 model Garfinkel (1944) to simply and accurately model astronomical refraction in a polytropic atmosphere. Garfinkel updated the model to use the 1962 U.S. standard atmosphere in Garfinkel (1967). Garfinkel’s methods for modeling astronomical refraction have been widely applied, including a particularly relevant application to refraction of the solar disk in the atmosphere from the perspective of an Earth orbiting satellite in Cameron et al. (1963). Cameron et al. (1963) presents a simplified implementation of Garfinkel’s 1944 paper which is much simpler than Garfinkel’s methods, and compares results with photographic observations from the Mercury Spacecraft (see Fig. 2.7).

Auer and Standish (2000) present a simple and efficient method for computing atmospheric refraction parameters that involves integration of the light ray path through the atmosphere over the angle  $\psi$  illustrated in Fig. 2.8. This method is much simpler than the methods from Garfinkel and even the simplified model from Cameron et al. (1963), however it is

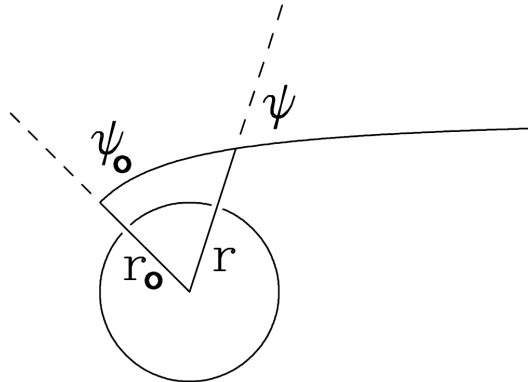


Figure 2.8: Refraction modeling geometry from Auer and Standish (2000). The distance to the geocenter ( $r$ ) and angle ( $\psi$ ) used to model refraction in the method presented by Auer and Standish (2000).

not analytic and requires a numerical solution of the light ray to geocenter distance ( $r$ ) at each ( $\psi$ ) angle in integration of the light ray path. The method from Auer and Standish (2000) has been in use since before its publication (e.g. by Seidelmann (1992)) for modeling refraction with any choice of atmospheric density profile. This flexibility and the simplicity of the refraction modeling presented by Auer and Standish (2000) makes it attractive for penumbra SRP modeling applications.

## 2.4 Atmospheric extinction

The spatial and seasonal variability of atmospheric conditions and the diverse population of particles in Earth's atmosphere make the modeling of absorption and scattering a very complicated problem. Fortunately, the utility of RTCs for a broad range of important scientific and engineering applications has led to the development of many approaches to this problem over the years, and the combination of improved rigorous models and new measurements have continually enabled researchers to refine the more practical, simpler models. Current state-of-the-art models of each type covered in this section offer distinct capabilities and levels of precision. This section will cover the following types of atmospheric radiative transfer models:

1. Line-By-Line Methods
2. Spectral Band Methods
3. Parameterized Transmittance Methods
4. Monte Carlo Methods

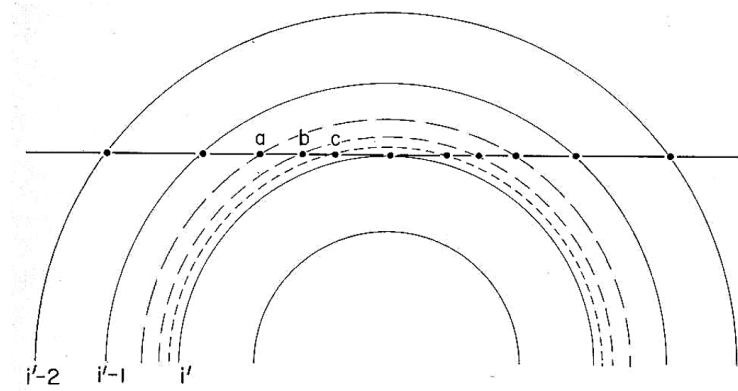


Figure 2.9: An example of a layered atmosphere model for radiative transfer from Avrett and Loeser (1984). This layered model of the atmosphere assumes spherical shells. Note that some models assume flat, infinite layers to further simplify the problem.

This section will introduce the state-of-the-art in each of these types of RTCs, cover the basic theory behind each of these methods and discuss their performance and computational characteristics. In describing some of these atmospheric RTCs, earlier radiative transfer methods will be introduced which formed the groundwork for these codes. While these earlier models do not represent the state-of-the-art in radiative transfer of solar radiation in the atmosphere, they often present simpler, less computationally expensive approaches.

### Line-by-line methods - FASCODE

To model scattering and absorption in the atmosphere, both the radiation and the atmospheric medium must be broken up into some finite number of elements (Avrett and Loeser, 1984). The solar radiation must be separated according to wavelength, with each spectral band having some amount of flux associated with it which is attenuated as it travels through the atmosphere. Similarly, the atmospheric medium is separated into a number of layers, each having a constant temperature, pressure, and set of scattering and absorption coefficients that are determined for each of the spectral bands of radiation incident on that layer. The distance the radiation travels through each layer is dependent on geometrical factors and processes. This separation of the medium into a finite number of layers is shown in Fig. 2.9, which depicts a spherical shell model for the structure of the atmospheric medium and a straight line model for the path of the radiation.

A line-by-line method models attenuation of radiation in each layer of the modeled atmosphere by applying broadening profiles based on the atmospheric conditions in that atmospheric layer (Thomas and Starnes, 2002). The FASCODE RTC uses the HITRAN database of spectral line data and applies Voigt broadening in its line-by-line computations so that both the pressure effects dominant at lower altitudes (Lorentz broadening) and the temperature effects dominant at higher altitudes (Doppler broadening) are captured (Smith et al.,

1978).

FASCODE was developed to offer increased speed over previous line-by-line codes by more efficiently forming the Voigt profiles for each band using layered sub-profiles. The attenuation parameters calculated for each layer of the atmosphere are determined at different spectral resolutions based on the properties of each layer to further improve computational efficiency. This leads to some layers having a higher spectral resolution than others, so the results from the layers are interpolated using Lagrangian interpolation to give the spectral resolution of the most finely divided layer. Line-by-line methods like FASCODE are computationally expensive, but offer high precision and spectral resolution.

### Spectral band methods - MODTRAN and LOWTRAN

The spectral band radiative transfer methods presented in this section are based on the same fundamental framework as line-by-line methods. Like FASCODE, the MODTRAN RTC uses the HITRAN database of spectral line data (Berk et al., 1989). However, the HITRAN data is not used directly in MODTRAN and is instead used to generate databases specifically for these codes. These newer methods are less accurate than line-by-line RTCs like FASCODE, but offer increased computing speed by grouping the effects of spectral lines from HITRAN into larger bins (spectral bands) (Berk et al. 2005, Kneizys et al. 1988).

LOWTRAN, the predecessor to MODTRAN, uses a single parameter, an absorption coefficient for each spectral attenuation band being modeled. As a result, the spectral resolution of LOWTRAN is generally limited to  $20\text{ cm}^{-1}$  (Anderson et al. 1993, Kneizys et al. 1988). MODTRAN uses an improved two-parameter model that includes an absorption coefficient and a line density parameter to increase the spectral resolution of the LOWTRAN7 code to  $2\text{ cm}^{-1}$  (Anderson et al. 1993, Kneizys et al. 1988, Gueymard 2001). MODTRAN uses the more robust Voigt line broadening profiles rather than the Lorentz profiles used by LOWTRAN. The MODTRAN RTC includes the latest version of LOWTRAN, and uses LOWTRAN at low altitudes where the HITRAN based MODTRAN database is missing data and where neglecting temperature dependent Doppler broadening of spectral lines is not detrimental to the spectral resolution of results (Anderson et al. 1993, Thomas and Stammes 2002).

MODTRAN is a very popular and widely available code that has been evaluated for a variety of applications. The study presented in Anderson et al. (1993) assesses the suitability of MODTRAN for remote sensing applications. In this study, results from the more rigorous FASCODE line-by-line method are compared with MODTRAN2 results. One of the comparisons from this study is shown in Fig. 2.10, and indicates that the MODTRAN2 RTC performs very similarly to the FASCODE RTC as long as a more complex temperature model is used with MODTRAN. This study concluded that MODTRAN could be used in place of more computationally expensive and rigorous codes, even for a demanding application like remote sensing.

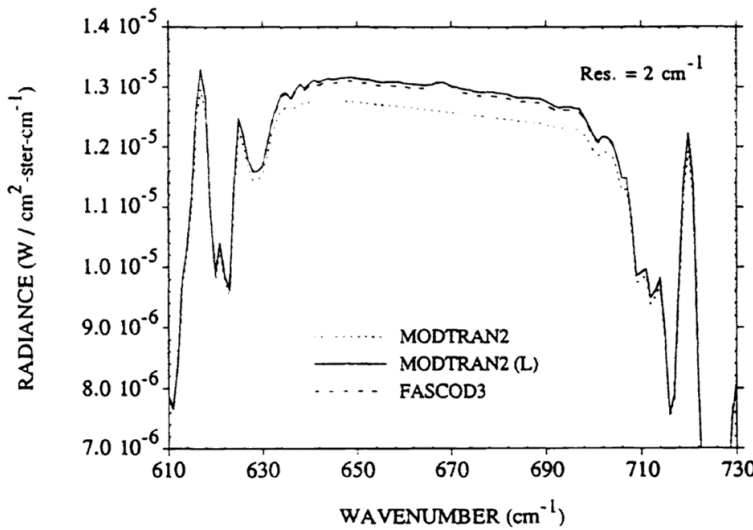


Figure 2.10: Comparison of Results from MODTRAN2 and FASCODE from Anderson et al. (1993). The line labeled “MODTRAN2(L)” shows results from using a more complex temperature model than the model with results labeled “MODTRAN2”. This comparison indicates that the MODTRAN2 RTC, using a more detailed temperature model, shows strong correlation with FASCODE results.

### Simple transmittance parameterization methods - SMARTS2 and SPCTRAL2

Radiative transfer codes based on transmittance parameterization models offer a significant computational cost advantage over the other, more rigorous RTCs described in this review by treating the atmosphere as a single homogenous layer. Solar spectral datasets and early modeling work introduced by Gates (1966) and Moon (1940), in conjunction with earlier rigorous RTC development (namely LOWTRAN) led some to pursue simpler models for practical engineering applications. The foundational work for the current state-of-the-art in simple, practical models for radiative transfer of sunlight in the atmosphere is presented by Leckner (1978).

The two models that will be the focus of this section are the most widely used and recently developed transmittance parameterization codes: SMARTS2 and SPCTRAL2. SPCTRAL2 is an updated version of the first SPCTRAL RTC presented in Bird and Riordan (1986) and based on the model proposed in Bird (1984). Birds proposed model was based on earlier work by Brine and Iqbal (1983) and the aforementioned foundational work by Leckner. Following the foundational work by Leckner, these codes use parameterized equations to define transmittance functions for Rayleigh scattering, ozone absorption, absorption by uniformly mixed gases, water vapor absorption, and aerosol attenuation. Tabulated parameters that are built into these codes are selected based on the properties of the homogenous atmosphere model, the wavelength of radiation, and the position of the Sun. This parameterization and table-lookup process greatly increases the speed of these types of codes when compared to

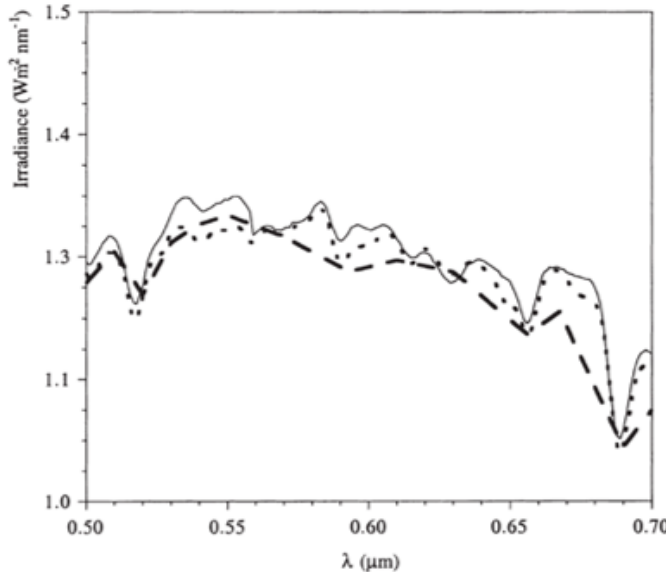


Figure 2.11: Comparison of Experimental (—), SPCTRAL2 (---), and SMARTS2 (···) Irradiance Results In Valencia, Spain from Utrillas et al. (1998). These results indicate that the more recent SMARTS2 model performs better. Note that over other spectral ranges, the two models performed more consistently and both produced better correlation with experimental results than over the range shown here.

the more rigorous RTCs covered in this review.

Gueymard (2001) presents the most recent state-of-the-art transmittance parameterized model: Simple Model of the Atmospheric Radiative Transfer 2 (SMARTS2). SMARTS2 was developed to take advantage of improved experimental data from observations of the atmosphere and the extraterrestrial solar spectral irradiance to improve upon the SPCTRAL2 model. Utrillas et al. (1998) describes a study to compare the results of both SMARTS2 and SPCTRAL2 to measurements in Valencia, Spain. Fig. 2.11 shows one set of results from this study that illustrates the improvements gained by the more accurate constants and parameterizations included in the SMARTS2 model.

Even simpler models that may be of interest in penumbra SRP applications have been developed which take the simplification of these methods further. These methods offer a valuable alternative to the other transmittance parameterization codes in certain applications where many evaluations of the model are needed or computing power is limited. Justus and Paris (1985) implement a simpler model focused on a narrow spectral band from 0.29 to 4  $\mu\text{m}$  and ignore the influence of clouds. The Justus and Paris model shows good performance when compared to experimental data and a significant reduction of computational cost over the other models outlined in this section. Gregg and Carder (1990) developed a simplified model based on SPCTRAL and specifically designed for maritime atmospheres. This model successfully takes advantage of the simpler surface properties of the ocean and different

aerosol environment above the ocean to simplify the SPCTRAL model. An earlier model by Gueymard, developed prior to his SMARTS models and described in Gueymard (1989), was introduced in 1989 and treats the radiation very simply as just two bands, one IR and one Visible/UV. The simplicity of this model reduces significantly its utility for more complex applications, but, again, it may be useful in certain engineering applications, especially where output spectral resolution is not important.

### Monte Carlo methods - BRITE and FLASH

Monte Carlo methods are very computationally expensive but effective approaches to modeling absorption and scattering of solar radiation in the atmosphere. These models use a statistically significant, large number of simulations of individual photon trajectories through a model atmosphere to estimate the overall results of radiative transfer. Photons are released into the modeling space and propagated from interaction point to interaction point in increments of mean free photon paths, a distance that is dependent on the properties of the model atmosphere. At each of these interaction points, a probability density function describing the probabilities of absorption, scattering, or no interaction at all is sampled using a randomly generated number. Once the photon is absorbed or meets some target location, then the simulation of that particle is finished and the result contributes to the statistical results. If the photon is scattered, then its new scattered direction is determined by randomly sampling from another statistical distribution describing the scattering pattern being modeled.

The BRITE and FLASH Monte Carlo RTCs have been thoroughly evaluated and applied to a number of problems (Bird, 1982). These codes were developed together but differ in their modeling of the atmosphere. BRITE uses infinite parallel planes to model layers of the atmosphere while FLASH uses spherical shell layers. Fig. 2.12 illustrates a few simulated photon paths through the FLASH model atmosphere. Bird (1982) points out that the BRITE model is much faster, but FLASH is necessary for accuracy as the Sun approaches the horizon.

The major advantage of Monte Carlo modeling is that it can be applied to model atmospheres with irregular layer boundaries and it is the only method that can rigorously capture the complex geometrical effects present in radiative transfer in the atmosphere (e.g. the multiple scattered and reflected photons shown in Fig. 2.12). In Bird (1982), Monte Carlo models are compared with other rigorous models and experimental data and show good correlation. BRITE was proven effective for practical applications in Riordan (1986) and used to update ASTM standards for sea level solar radiation.

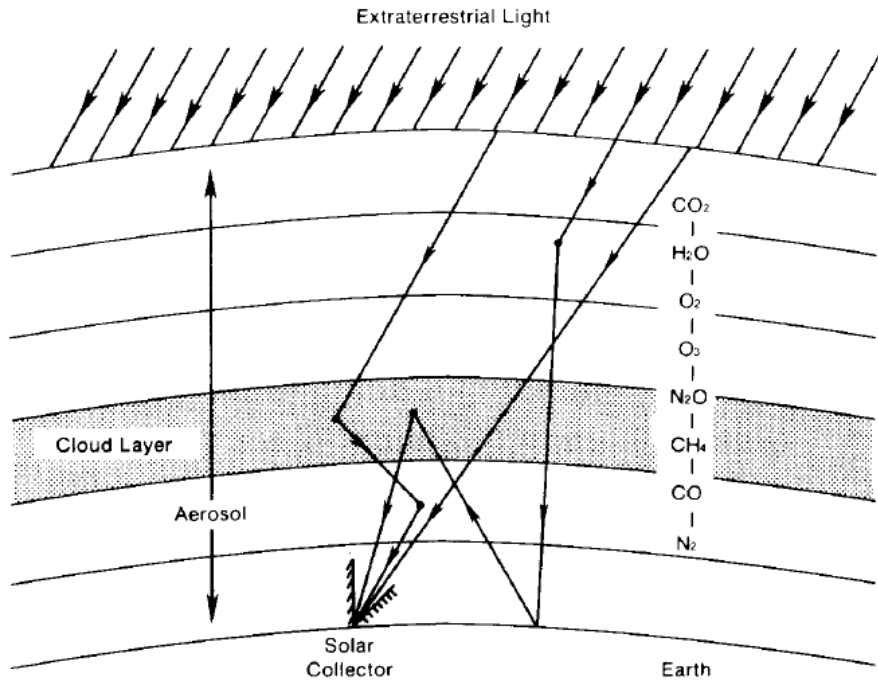


Figure 2.12: Simulated photon paths in a Monte Carlo model from Bird 1982. The spherical shell atmosphere shown here is the model atmosphere for the BRITE Monte Carlo RTC.

## 2.5 Summary

Most of the penumbra SRP models presented to this point lie at two extremes of complexity and computational cost. The most complex and accurate models (most notably those presented by Vokrouhlický et al. from 1993-1996), which this work aims to build upon, consider the effects of the atmosphere and the oblate shape of Earth. The effect of Earth oblateness on penumbra SRP is usually ignored, however a few useful approaches have been developed to consider this important geometric factor. Significantly more attention has been given to atmospheric refraction and extinction, as there are many more applications of this modeling. Atmospheric extinction in particular has been the topic of many unique models, offering many options for addressing this complex factor which significantly influences penumbra SRP.

# Chapter 3

## Theory and modeling

Each solar photon passing through Earth's atmosphere to strike a satellite in penumbra is taking a unique path through the atmosphere. With its unique path, each photon is exposed differently to the various constituents of the atmosphere, causing spatial variations in penumbra solar radiation fields (i.e. the image of Sun in penumbra is no longer circularly symmetric in shape, brightness, or specular composition). To account for this, like Vokrouhlický et al. (1993), we separate the solar radiation field into a finite number of light rays. The result of this approach is essentially an image of the solar disc from the perspective of the satellite. Fig. 3.1 is a preview of one of the outputs of the SOLAARS model, to be explained in detail in this section. The shape of the solar discs and of the penumbra region illustrated in Fig. 3.1 show the significant influence that atmospheric refraction has on penumbra solar radiation fields, and, in turn, the SRP accelerations of an object in penumbra.

We model atmospheric refraction and extinction to determine the direction, radiance, and spectral composition of each light ray in a modeled solar radiation field, so that we can precisely determine the resulting SRP accelerations. Fig. 3.1 introduces the light ray grazing height ( $h_g$ ) which is the lowest altitude of a light ray above the solid Earth during its path from the Sun. This grazing height is a key parameter in the SOLAARS model. The full sunlight boundary of the penumbra region occurs where the bottom of the solar image enters the top of the atmosphere at the atmosphere height ( $h_T$ ), and the umbra boundary occurs where the top of the solar image, refracted in the atmosphere, grazes the solid Earth. As introduced in Section 1.4, one of the important innovations of this research is the finding that all parameters describing atmospheric effects can be calculated and tabulated based on this single geometric variable. As a result, we are able to generate tables of atmospheric refraction and extinction parameters as a function of grazing height ( $h_g$ ) for a given description of the atmosphere, and use these tables in SRP modeling. This isolation of atmospheric effects modeling is key, because it allows us to add significantly to the precision of atmospheric effects modeling without increasing the computational cost of SRP modeling.

Fig. 3.2 shows the flow of inputs to various stages in the model. Atmospheric effects modeling

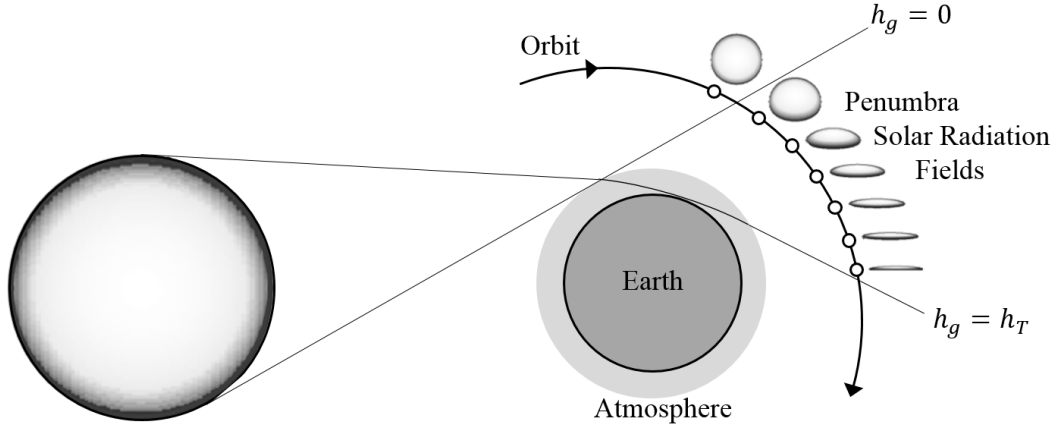


Figure 3.1: A satellite penumbra transition with atmospheric effects. The boundaries of the penumbra region are extended by the atmosphere in the full sunlight and umbra directions. Note the significant compression of the SOLAARS modeled solar radiation fields in penumbra due to atmospheric refraction.

produces tables of refraction and extinction parameters as a function of grazing height ( $h_g$ ), which we use in SOLAARS without repeating this stage. Earth oblateness modeling uses the Earth polar flattening coefficient and the positions of the satellite and Sun to assign the Spherical Earth radius and adjust satellite and Sun positions to account for a new, shifted geocenter. This adjustment allows us to accurately approximate the oblate Earth with a spherical one. We use these tables, the mean solar radiance, and geometric variables to model the solar radiation field incident on the satellite. Finally, we model the interaction of these light rays with the satellite to calculate the SRP acceleration. While many of these variables have not been described, it is useful to clearly present the flow of information now so that, as we move forward, the role of each step in the SOLAARS modeling process is clear.

This chapter includes all of the formulas and derivations involved in the full SOLAARS model. Sufficient detail is included, and formulas are presented in a sufficiently general way, so that others may make decisions regarding implementation of SOLAARS to suit their application. The final section of this chapter presents the development and implementation of the simpler SOLAARS-CF model.

### 3.1 Earth oblateness

As readers will see in the following sections of this chapter, the solar radiation field modeling in SOLAARS is based on the assumption of a spherical Earth and spherically symmetric atmosphere. Therefore, to consider the oblate shape of Earth, we must approximate the oblate Earth with a spherical one. The position and radius of this sphere are assigned to

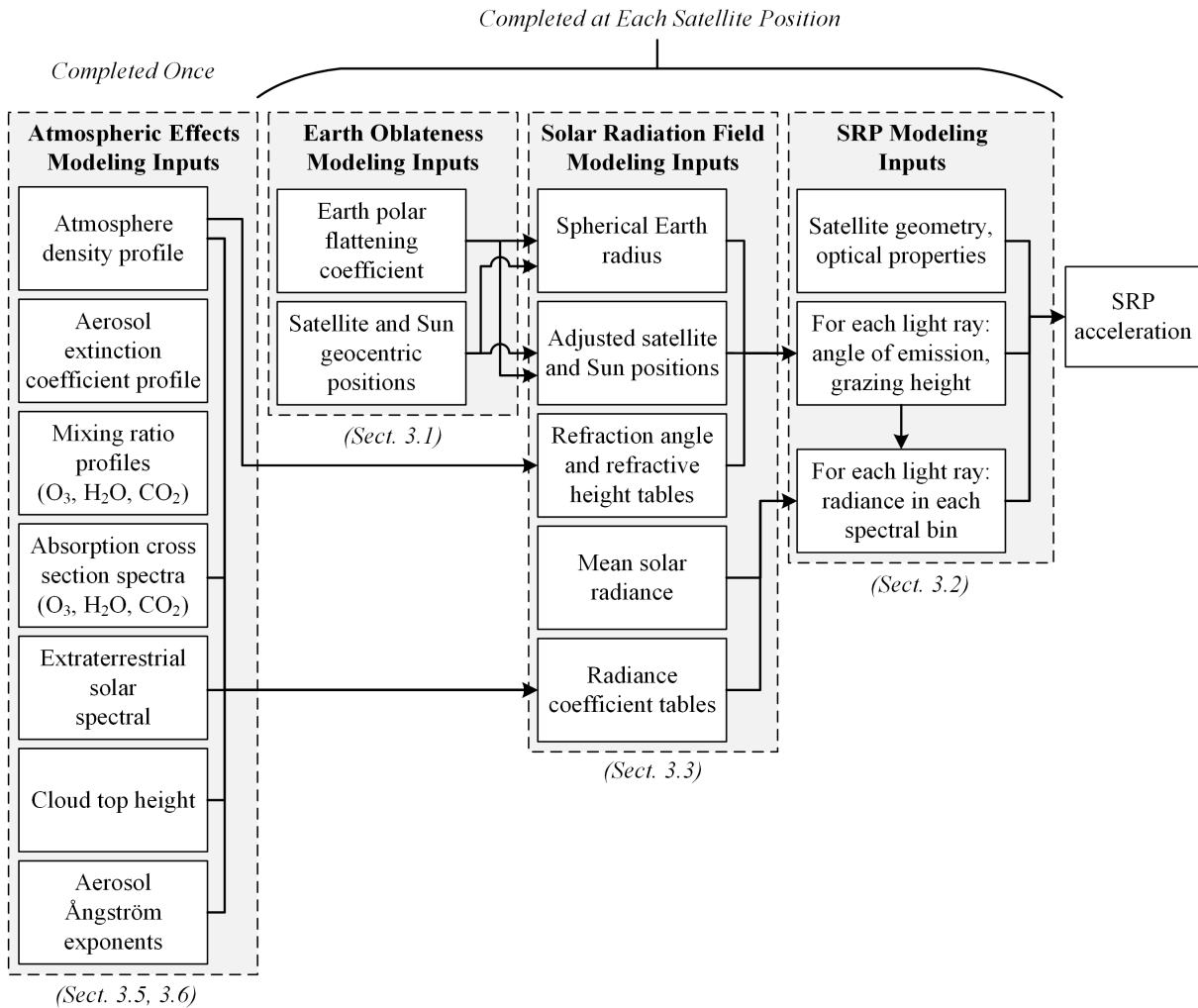


Figure 3.2: Flow of inputs and intermediate results for computing penumbra SRP accelerations. We tabulate the output of atmospheric effects modeling, where the most computationally intensive steps take place, so that we can do this very precisely without influencing the speed of SRP acceleration calculations.

best approximate the Earth horizon presented to the satellite at each position in penumbra.

The method from Adhya et al. (2004) is not directly applicable to SOLAARS modeling because it only considers the solid Earth, and is intended as a binary check at each satellite position for penumbra state rather than a method to accurately position some representative Earth geometry for precise SRP calculations. Additionally, because we separate and tabulate atmospheric effects to significantly reduce computational cost, the approach from Vokrouhlický et al. (1996) cannot be used to completely integrate oblateness into our geometric formulas.

To accurately account for the influence of Earth oblateness on penumbra SRP, we apply elements from both Adhya et al. (2004) and Vokrouhlický et al. (1996). We define a spherical Earth by its radius ( $R_{\oplus}$ ) and position relative to the actual geocenter ( $\vec{p}_{\oplus}$ ) which best represents the horizon from the perspective of the satellite. This is a two step process which is carried out at each satellite position:

1. An approach similar to that of Adhya et al. (2004) is used to determine a characteristic solar grazing point on an oblate spheroid approximation of the solid Earth.
2. An approach similar to the one presented in Vokrouhlický et al. (1996) is used to define a new geocenter and Earth radius for use in SRP modeling.

### 3.1.1 Locating the characteristic grazing point

The geometry involved in considering oblateness is illustrated in Fig. 3.3. The three dimensional diagram on the left of Fig. 3.3 illustrates how the characteristic grazing point is selected. The characteristic grazing point vector ( $\vec{G}$ ) points to the location on a scaled version of the oblate spheroid (scaled by the factor  $k_s$ ) which results in a single intersection with the satellite to Sun vector ( $\vec{d}$ ). The  $\hat{N}$  plane in Fig. 3.3 is the plane containing the geocenter, satellite, and grazing point vector. The objective of SOLAARS oblateness modeling is to approximate the oblate Earth position and curvature at the point on the spheroid intersected by  $\vec{G}$  in the  $\hat{N}$  plane. In this section, we will apply is approach similar to that of Adhya et al. (2004) to determine the characteristic grazing point vector ( $\vec{G}$ ).

To determine,  $\vec{G}$ , we impose two conditions. First,  $\vec{G}$  satisfies the equation of  $\vec{d}$ :

$$\vec{G} = \vec{r} + \vec{d} \quad (3.1)$$

and therefore:

$$\frac{G_1 - r_1}{d_1} = \frac{G_2 - r_2}{d_2} = \frac{G_3 - r_3}{d_3} \quad (3.2)$$

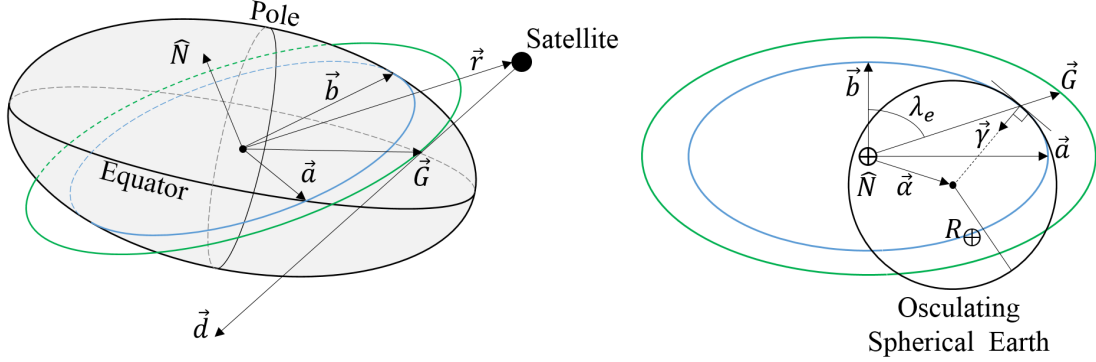


Figure 3.3: Geometry involved in SOLAARS Earth oblateness modeling. The satellite position ( $\vec{r}$ ) and satellite to Sun vector ( $\vec{d}$ ) are used to find the grazing point vector ( $\vec{G}$ ). The  $\hat{N}$  plane defines the slice of the spheroid described in the two dimensional illustration on the right. The blue ellipse is a slice by the  $\hat{N}$  plane of the Earth oblate spheroid, and the green ellipse is a scaled version of the blue ellipse which results in a single intersection with  $\vec{d}$ . The blue ellipse is parameterized by its semimajor ( $\vec{a}$ ) and semiminor ( $\vec{b}$ ) axis vectors, and the angle  $\lambda_e$  describes the orientation of  $G$  in this ellipse.  $\vec{\gamma}$  is the normal to the ellipse at the angle  $\lambda_e$ .  $R_{\oplus}$  and  $\vec{\alpha}$  are the radius and center of the osculating spherical Earth.

where the numerical subscripts 1, 2, 3 denote the  $x$ ,  $y$ , and  $z$  components of each vector in any reference frame where  $z$  points to a pole. From Eq. 3.2, we can define  $G_2$  and  $G_3$  in terms of  $G_1$ :

$$G_2 = \frac{d_2}{d_1}(G_1 - r_1) + r_2 \quad (3.3)$$

$$G_3 = \frac{d_3}{d_1}(G_1 - r_1) + r_3 \quad (3.4)$$

Second,  $\vec{G}$  satisfies the equation of a scaled version of the oblate spheroid (scaled by the factor  $k_s$ ):

$$\frac{G_1^2 + G_2^2}{k_s^2 R_{\oplus e}^2} + \frac{G_3^2}{k_s^2 R_{\oplus p}^2} = 1 \quad (3.5)$$

By substituting Eqs. 3.3 and 3.4 into Eq. 3.5, like Adhya et al. (2004), we develop a quadratic in  $G_1$ :

$$\begin{aligned}
& AG_1^2 + BG_1 + C = 0 \quad (3.6) \\
A &\equiv d_3^2 k_s^2 R_{\oplus e}^2 + d_1^2 k_s^2 R_{\oplus p}^2 + d_2^2 k_s^2 R_{\oplus p}^2 \\
B &\equiv 2k_s^2 R_{\oplus e}^2 d_1 d_3 r_3 + 2r_2 d_1 d_2 k_s^2 R_{\oplus p}^2 - 2r_1 d_3^2 k_s^2 R_{\oplus e}^2 - 2r_1 d_2^2 k_s^2 R_{\oplus p}^2 \\
C &\equiv k_s^2 R_{\oplus p}^2 (d_1^2 r_2^2 + r_1^2 d_2^2 - 2r_1 r_2 d_1 d_2) + k_s^2 R_{\oplus e}^2 (r_3^2 d_1^2 - 2r_1 r_3 d_1 d_3 + r_1^2 d_3^2) - d_1^2 k_s^2 R_{\oplus e}^2 k_s^2 R_{\oplus p}^2
\end{aligned}$$

This quadratic is equivalent to the quadratic in Adhya et al. (2004), but with the added scale factor terms. Note that Adhya et al. (2004) has errors in the  $B$  and  $C$  terms. We can then apply the quadratic equation to solve for  $G_1$ :

$$G_1 = \frac{-B \pm \sqrt{B^2 - 4AC}}{2A} \quad (3.7)$$

However, we first need to solve for the scaling factor ( $k_s$ ). To impose the condition of a single intersection point with the scaled spheroid and locate our characteristic grazing point, we simply set  $\sqrt{B^2 - 4AC} = 0$ . From this relation, we can form a new quadratic in  $k_s$ :

$$\begin{aligned}
& Dk_s^2 + E = 0 \quad (3.8) \\
D &\equiv 4d_1^2 R_{\oplus p}^2 (d_3^2 R_{\oplus e}^4 + d_1^2 R_{\oplus e}^2 R_{\oplus p}^2 + d_2^2 R_{\oplus e}^2 R_{\oplus p}^2) \\
E &\equiv 4d_1^2 R_{\oplus p}^2 [r_3^2 (d_1^2 + d_2^2) R_{\oplus e}^2 + 2r_3 d_3 (d_1 r_1 + d_2 r_2) R_{\oplus e}^2 + r_2^2 d_3^2 R_{\oplus e}^2 + r_2^2 d_1^2 R_{\oplus p}^2 - 2r_1 r_2 d_1 d_2 R_{\oplus p}^2 \\
&\quad + r_1^2 (d_3^2 R_{\oplus e}^2 + d_2^2 R_{\oplus p}^2)]
\end{aligned}$$

We then solve this quadratic for the scaling factor,  $k_s$ :

$$k_s = \sqrt{\frac{-E}{D}} \quad (3.9)$$

With the scaling factor defined, we can finally solve Eq. 3.6 for  $G_1$ . Since we solved for  $k_s$  to force the root term in the quadratic formula solution to Eq. 3.6 to zero, the solution for  $G_1$  becomes:

$$G_1 = \frac{-B}{2A} \quad (3.10)$$

This solution is then used with Eqs. 3.3 and 3.4 to complete the solution for the vector pointing to the characteristic grazing point,  $\vec{G}$ .

### 3.1.2 Describing the osculating spherical Earth

In the previous section, we determined the location on the oblate Earth that we would like to approximate using a sphere. The right diagram in Figure 3.3 illustrates how the osculating sphere is defined. The osculating sphere we use to approximate Earth is tangent to and matches the radius of curvature of the elliptical oblate Earth slice in the plane,  $\hat{N}$ , which contains  $\vec{r}$  and  $\vec{G}$ :

$$\hat{N} = \frac{\vec{G} \times \vec{r}}{\|\vec{G} \times \vec{r}\|} \quad (3.11)$$

To determine the location and radius of our osculating sphere, we need to compute the semimajor axis and semiminor axis vectors of the elliptical slice of the oblate spheroid by the plane  $\hat{N}$ . First, we solve for the semimajor axis vector,  $\vec{a}$ . We know that the semimajor axis vector lies in the  $\hat{N}$  plane. In addition, we can demonstrate that  $\vec{a}$  lies in the equatorial plane of the oblate spheroid. Any slice through the oblate Earth which includes the geocenter will cross the equatorial plane. Since the oblate spheroid radius is maximum in the equatorial plane, it must be the location of the semimajor axis. By setting  $a_3 = 0$ , the equation of the  $\hat{N}$  plane gives the following:

$$a_1 = \frac{-N_2}{N_1} a_2 \quad (3.12)$$

Next, we impose the condition that  $\vec{a}$  points to a location on the oblate spheroid and again set  $a_3 = 0$ , eliminating the  $\frac{1}{R_{\oplus p}^2}$  term from the equation of the oblate spheroid:

$$\frac{a_1^2 + a_2^2}{R_{\oplus e}^2} = 1 \quad (3.13)$$

Using Eqs. 3.12 and 3.13 we can solve for  $\vec{a}$ :

$$\vec{a} = \begin{bmatrix} \frac{-N_2 R_{\oplus e}}{\sqrt{N_1^2 + N_2^2}} \\ \frac{N_1 R_{\oplus e}}{\sqrt{N_1^2 + N_2^2}} \\ 0 \end{bmatrix} \quad (3.14)$$

The semiminor axis vector,  $\vec{b}$ , is perpendicular to  $\vec{a}$  and in the  $\hat{N}$  plane. So, we know the direction of  $\vec{b}$ , but must solve for its magnitude using the equation of the oblate spheroid. We define  $\vec{b}$  as a function of a scaling factor,  $k_b$ :

$$\vec{b} = k_b \hat{N} \times \vec{a} = \begin{bmatrix} \frac{-k_b N_3 N_1 R_{\oplus e}}{\sqrt{N_1^2 + N_2^2}} \\ \frac{-k_b N_3 N_2 R_{\oplus e}}{\sqrt{N_1^2 + N_2^2}} \\ k_b R_{\oplus e} (N_1^2 + N_2^2)^{3/2} \end{bmatrix} \quad (3.15)$$

To solve for  $k_b$ , we insert the components of  $\vec{b}$  from Eq. 3.15 into the equation of the oblate spheroid:

$$\frac{b_1^2 + b_2^2}{R_{\oplus e}^2} + \frac{b_3^2}{R_{\oplus p}^2} = 1 \quad (3.16)$$

Solving for  $k_b$  gives:

$$k_b = \left[ N_3^2 + \frac{R_{\oplus e}}{R_{\oplus p}} (N_1^2 + N_2^2) \right]^{-1/2} \quad (3.17)$$

The angle  $\lambda_e$  associated with our characteristic grazing point  $\vec{G}$  is measured from the semimajor axis:

$$\lambda_e = \arccos \left( \frac{\vec{G} \cdot \vec{b}}{\|\vec{G}\| \|\vec{b}\|} \right) \quad (3.18)$$

Like Vokrouhlický et al. (1996), we use the angle  $\lambda_e$  to compute our osculating Earth radius as the radius of curvature of the ellipse at  $\lambda_e$ :

$$R_{\oplus} = b^2 a^2 \left( \frac{\sin^2 \lambda_e}{a^2} + \frac{\cos^2 \lambda_e}{b^2} \right) \quad (3.19)$$

where  $a$  and  $b$  are the lengths of the semimajor and semiminor axes.

The final step is to solve for the location of the center of our osculating spherical Earth. The center is found by calculating the normal vector of the ellipse,  $\vec{\gamma}$ , at  $\lambda_e$  and moving in that direction the distance  $R_{\oplus}$  as shown in Fig. 3.3. This places the osculating sphere such that it is tangent to the elliptical slice at the point intersected by  $\vec{G}$  on the oblate spheroid. We again follow the approach of Vokrouhlický et al. (1996) and calculate components of  $\vec{\gamma}$  in the directions described by  $\vec{a}$  and  $\vec{b}$ :

$$\vec{\gamma} = \gamma_a \frac{\vec{a}}{a} + \gamma_b \frac{\vec{b}}{b} \quad (3.20)$$

where we calculate the  $\gamma_a$  and  $\gamma_b$  components using  $\lambda_e$ :

$$\gamma_a = a \sin \lambda_e [(a^2 - b^2) \cos^2 \lambda_e (\cos^2 \lambda_e + b^2 \sin^2 \lambda_e)^{-3/2} - (\cos^2 \lambda_e + b^2 \sin^2 \lambda_e)^{-1/2}] \quad (3.21a)$$

$$\gamma_b = b \cos \lambda_e [(b^2 - a^2) \sin^2 \lambda_e (\cos^2 \lambda_e + b^2 \sin^2 \lambda_e)^{-3/2} - (\cos^2 \lambda_e + b^2 \sin^2 \lambda_e)^{-1/2}] \quad (3.21b)$$

As previously mentioned, the location of the new geocenter is found by moving along this normal direction a distance  $R_{\oplus}$  from the intersection of  $\vec{G}$  and the oblate spheroid. This intersection point on the surface of the spheroid is found by simply scaling  $\vec{G}$  with the  $k_s$  factor to give  $\frac{\vec{G}}{k_s}$ . The osculating sphere geocenter is then:

$$\vec{\alpha} = \frac{\vec{G}}{k_s} + \frac{\vec{\gamma} R_{\oplus}}{\|\vec{\gamma}\|} \quad (3.22)$$

Finally, we redefine the Sun ( $\vec{R}$ ) and satellite ( $\vec{r}$ ) position vectors to account for the new geocenter location:

$$\vec{R}' = \vec{R} - \vec{\alpha} \quad (3.23a)$$

$$\vec{r}' = \vec{r} - \vec{\alpha} \quad (3.23b)$$

### 3.1.3 Implementation

The flowchart in Fig. 3.4 describes the software implementation of the SOLAARS oblateness model. The satellite and Sun positions are used to determine the characteristic grazing point and  $\hat{N}$  plane illustrated in the right of Fig. 3.3. The properties of the elliptical slice of the spheroid are then used to determine the position and radius of the osculating spherical Earth. Finally, the satellite and Sun position vectors are shifted to effectively move the geocenter to the center of the osculating spherical Earth. This process is carried out at each satellite position. In the interest of isolating oblateness modeling from the remainder of the complex geometric formulas presented in the remainder of this chapter, these new positions, defined in Eqs. 3.23a and 3.23b, will be referred to using their un-adjusted symbols:  $\vec{R}$  and  $\vec{r}$ .

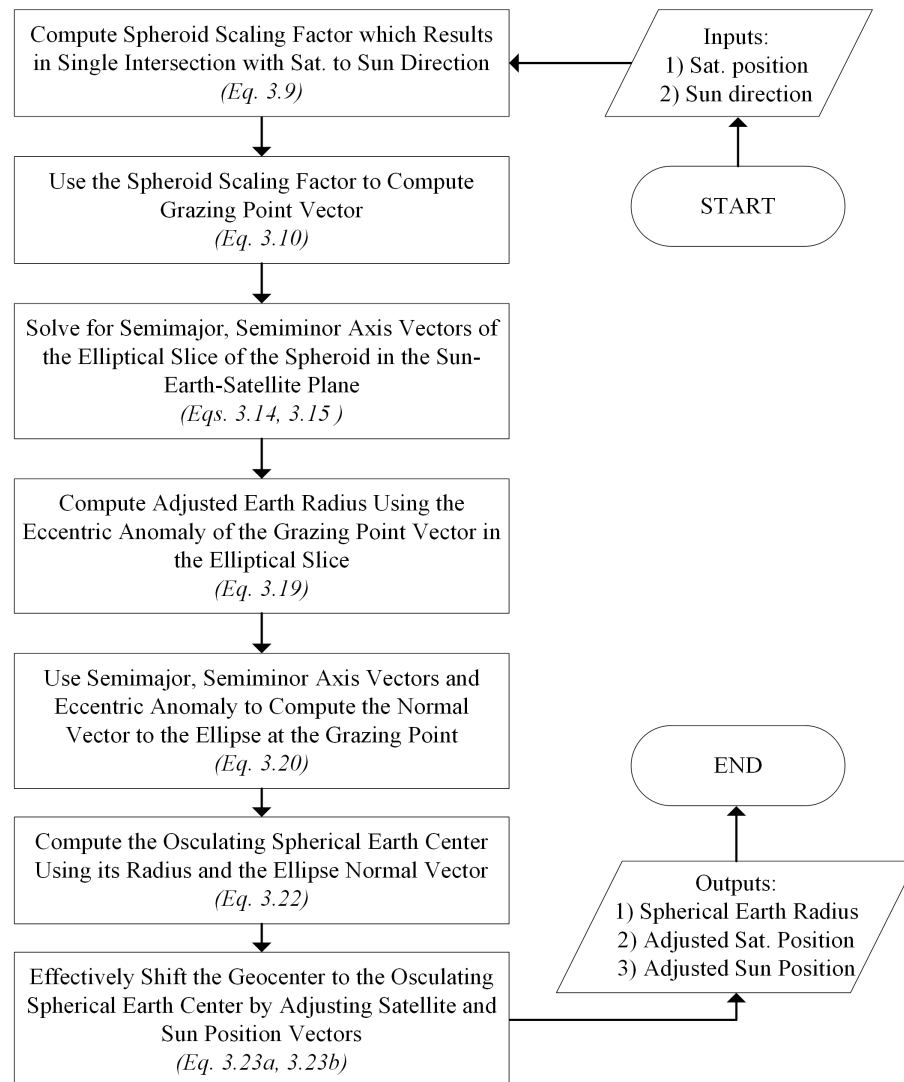


Figure 3.4: Flowchart outlining the process for adjusting geometric parameters for Earth oblateness at each satellite position.

## 3.2 Fundamental SRP acceleration formula

Each light ray represents a solid angle portion of the solar radiation field ( $\Delta\Omega_i$ ) and has some radiance ( $L_i$ ) and direction at the satellite position ( $\hat{n}_i$ ). The acceleration of the satellite in response to the  $i_{th}$  light ray is:

$$\vec{a}_i = \frac{1}{mc} L_i \vec{O}(\hat{n}_i) \Delta\Omega_i \quad (3.24)$$

where  $m$  is the satellite mass,  $c$  is the speed of light, and  $\vec{O}$  is the optics function, which describes the interaction of light with the satellite (i.e. reflection and absorption).

Since the radiance of sunlight and optical properties of satellite surfaces vary with wavelength, the accuracy of SRP modeling can be improved by treating spectral bands separately. We separate the radiance of each light ray into  $N_b$  spectral bins, with a separate radiance for each bin ( $L_{i,j}$ ) describing the optical power in its respective band of the solar spectrum. Eq. 3.24 becomes:

$$\vec{a}_i = \frac{1}{mc} \sum_{j=1}^{N_b} \left[ L_{i,j} \vec{O}_j(\hat{n}_i) \right] \Delta\Omega_i \quad (3.25)$$

Treating light ray radiances separately for each spectral bin captures the changes in sunlight spectral composition as it passes through the atmosphere. Treating the optics function separately for each spectral bin captures the varying optical properties of the satellite (e.g. reflectivity coefficients) with wavelength. There are a variety of approaches to modeling the SRP acceleration of an object when subjected to light of a particular radiance and direction, which is why we do not explicitly define the optics function ( $\vec{O}$ ) or number of spectral bins ( $N_b$ ) here. These approaches differ significantly based on the level of accuracy required, knowledge of the object's optical properties and geometry, and allowable computational cost.

For a simple optics function, we can approximate the satellite geometry as a sphere with a cross sectional area ( $A$ ) equal to the average area exposed to the Sun, describe the fraction of reflected light using a single reflectivity coefficient ( $C_r$ ), and use one spectral bin (i.e.  $N_b = 1$ ). In this simple “cannonball” case, the optics function is independent of satellite orientation relative to incident light rays, and the SRP force simply acts in the direction of the incident ray:

$$\vec{O} = \hat{n} A C_r \quad (3.26)$$

Significantly more accurate methods are possible when the object geometry is documented and attitude data are available. In this case, we can treat the geometry as a number of primitive shapes (e.g. flat plates, hemispheres, etc.) and use each primitive's area, optical

properties, and orientation to model its contribution to the optics function. Monte Carlo type statistical methods (see Doornbos et al. 2002) or ray tracing algorithms (see Ziebart 2004) can be applied to this approximation of the object geometry to consider complex, but potentially significant effects such as self shadowing of surfaces, multiple reflections, and thermal reradiation. A detailed mathematical description of these methods is beyond the scope of this dissertation, as our focus is precisely modeling the solar radiation field rather than the satellite geometry and optical properties.

The light ray radiance in a given spectral bin ( $L_{i,j}$ ) is influenced by:

1. Atmospheric extinction due to its path through the atmosphere
2. The angle of emission from the Sun ( $\beta$ )
3. Temporal variations in solar activity affecting the mean solar radiance ( $L_\odot$ )

Radiance coefficients ( $\bar{L}_j$ ), which we will tabulate as a function of grazing height ( $h_g$ ), capture the effects of atmospheric extinction. A solar limb darkening coefficient ( $\mathbb{L}$ ) captures the decrease in radiance with lower angles of emission ( $\beta$ ) from the Sun's surface. Like Vokrouhlický et al. (1993), we use Eddington's approximation to assign a limb darkening coefficient:

$$\mathbb{L} = \frac{3}{4} \left[ \frac{7}{12} + \frac{1}{2}\mu + \mu \left( \frac{1}{3} + \frac{1}{2}\mu \right) \ln \left( \frac{1+\mu}{\mu} \right) \right] \quad (3.27)$$

$$\mu = \cos(\beta)$$

The mean solar radiance ( $L_\odot$ ) can be set based on measured or forecasted values to account for variations in solar activity with time. A common measure of solar activity, daily total solar irradiance ( $I_\odot$ ), can be converted to  $L_\odot$ , using the following from McCartney (1976):

$$L_\odot = I_\odot \frac{4AU}{A_\odot} \quad (3.28)$$

where  $AU$  is one astronomical unit and  $A_\odot$  is the surface area of the Solar photosphere. We compute light ray radiance in each spectral bin ( $L_{i,j}$ ) as the product of the radiance coefficient ( $\bar{L}_j$ ), limb darkening coefficient ( $\mathbb{L}$ ), and the mean solar radiance ( $L_\odot$ ). Eq. 3.25 becomes:

$$\vec{a}_i = \frac{1}{mc} \sum_{j=1}^{\mathbb{N}_b} \left[ \mathbb{L}(\beta) \bar{L}_j(h_g) L_\odot \vec{O}_j(\hat{n}_i) \Delta\Omega_i \right] \quad (3.29)$$

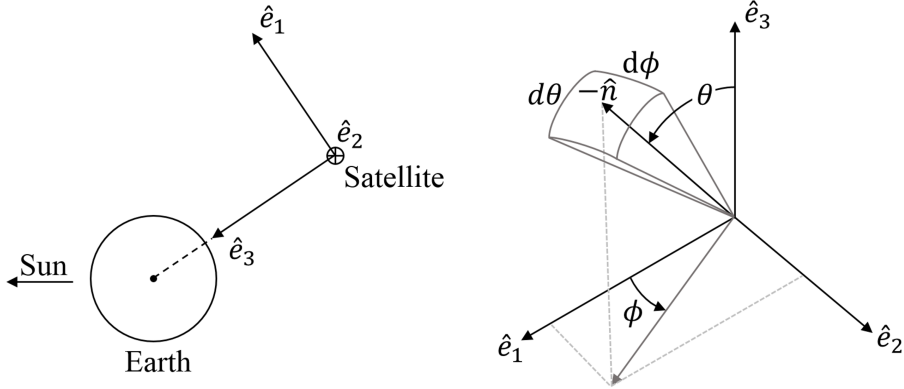


Figure 3.5: Earth pointing reference frame ( $\{e\}$ ) for SRP calculations and spherical coordinates  $\theta$  and  $\phi$ . Note that in the left view, the Sun-Earth-satellite plane is the plane of the page.  $\Delta\phi$  and  $\Delta\theta$  are used in numerical integration in the place of the differential solid angle  $\Delta\Omega$  in Eq. 3.30.

Finally, to solve for the total SRP acceleration, we sum over the finite number of light rays ( $N_r$ ) which make up our model of the solar radiation field:

$$\vec{a} = \frac{L_\odot}{mc} \sum_{i=1}^{N_r} \sum_{j=1}^{N_b} \left[ \mathbb{L}(\beta_i) \bar{L}_j(h_{g,i}) \vec{O}_j(\hat{n}_i) \Delta\Omega_i \right] \quad (3.30)$$

Once we have tables of atmospheric refraction and extinction parameters, we can evaluate Eq. 3.30 based on the geometry of the light ray path from the Sun to the satellite, which determines the light ray angle of emission ( $\beta$ ), grazing height ( $h_g$ ), and direction at the satellite ( $\hat{n}$ ). We define the geometric parameters describing the path of each light ray using the Earth pointing reference frame ( $\{e\}$ ) shown in Fig. 3.5. In this reference frame, the origin is fixed at the satellite position, the  $\hat{e}_3$  component points towards Earth center and the  $\hat{e}_1$  and  $\hat{e}_3$  components lie in the Sun-Earth-satellite plane. The  $\hat{e}_2$  component is defined to complete a right-handed triad. Note that the  $\hat{e}_1$  projection on the Sun-Earth vector must point to the Sun. Each light ray unit vector is defined in terms of the spherical coordinates  $\theta$  and  $\phi$  in the Earth pointing frame as:

$$\hat{n}_i = - \begin{bmatrix} \sin(\theta)\cos(\phi) \\ \sin(\theta)\sin(\phi) \\ \cos(\theta) \end{bmatrix} \quad (3.31)$$

Implementation of the Earth pointing frame ( $\{e\}$ ) allows us to express the solid angle term ( $\Delta\Omega$ ) in Eq. 3.30 with the equivalent expression:  $\sin\theta\Delta\theta\Delta\phi$ . Eq. 3.30 becomes:

$$\vec{a} = \frac{1}{mc} \sum_{i=1}^{N_r} \sum_{j=1}^{N_b} \left[ \mathbb{L}(\beta_i) \bar{L}_j(h_{g,i}) L_{\odot} \vec{O}_j(\hat{n}_i) \sin(\theta_i) \Delta\theta_i \Delta\phi_i \right] \quad (3.32)$$

In order to evaluate Eq. 3.32, we need to compute:

1. The shape of the solar radiation field from the perspective of the satellite (i.e. boundaries in spherical angles  $\theta$  and  $\phi$ )
2. For each light ray with some direction in  $\theta$  and  $\phi$  within the solar radiation field, its grazing height ( $h_g$ ) and angle of emission from the Sun ( $\beta$ )
3. Atmospheric refraction angle ( $Re$ ) and refractive height ( $S$ ) tables needed for items (1) and (2)
4. Radiance coefficient ( $\bar{L}_j$ ) tables which capture the effects of atmospheric extinction

We will start by deriving the necessary geometric formulas to accomplish (1) and (2) in Sect. 3.3. Establishing these geometric formulas allows us to describe the software implementation of SOLAARS in Sec. 3.4. In Sects. 3.5 and 3.6, we will determine how atmospheric refraction parameters and radiance coefficients, respectively, are computed as a function of light ray grazing height ( $h_g$ ) to accomplish (3) and (4). Finally, in Sect. 3.7, we will describe the development and implementation of the simpler SOLAARS-CF model.

### 3.3 Light ray geometry

Vokrouhlický et al. (1993) introduced a set of geometric parameters and relations to compute the limits of the local solar radiation field (i.e. boundaries in  $\theta$  and  $\phi$ ) and the angle of emission ( $\beta$ ) and grazing height ( $h_g$ ) of each light ray. Here we will introduce an equivalent set of geometrical parameters and relations to accomplish the same goals; however, we provide additional details and attempt to describe the light ray geometry in a more intuitive way. In this section, we will:

1. Develop an equation to solve for light ray grazing height ( $h_g$ ) as a function of  $\theta$
2. Solve for the overall  $\theta$  limits of the solar radiation field
3. Solve for the overall  $\phi$  limits of the solar radiation field
4. Address the effects of non-zero  $\phi$  angles on various geometric parameters, allowing us to complete our definition of the solar radiation field limits and compute light ray angle of angle of emission ( $\beta$ )

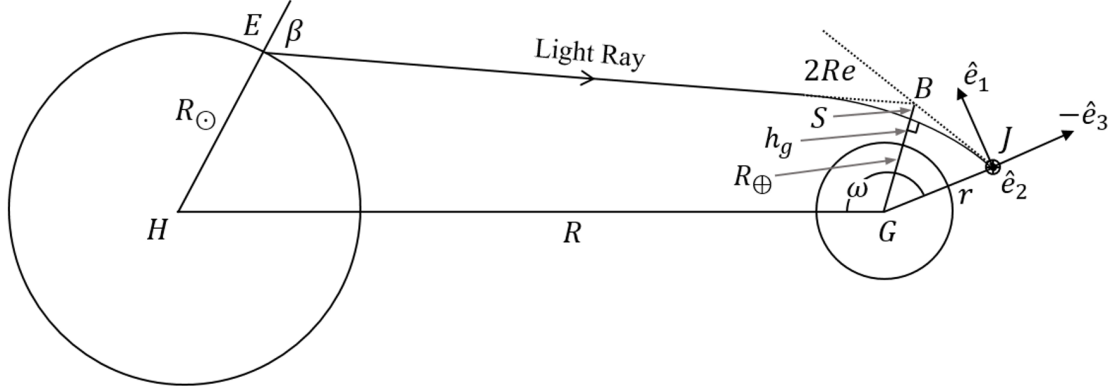


Figure 3.6: Light ray geometry in the  $\phi = 0$  plane. Points  $H$ ,  $E$ ,  $G$ ,  $B$ , and  $J$  are the center of the Sun, location of emission, geocenter, vertex of refraction, and satellite position, respectively. The line from the geocenter to the vertex of refraction has three segments: the Earth radius ( $R_{\oplus}$ ), grazing height ( $h_g$ ), and refractive height ( $S$ ).  $R$  and  $r$  are the geocentric distances to the Sun and satellite, respectively.  $Re$  is the light ray refraction angle and  $\omega$  is geocentric Sun-satellite angle.

Fig. 3.6 introduces the light ray geometry, including the angle of emission ( $\beta$ ) and grazing height ( $h_g$ ) which we are interested in solving for as a function of  $\theta$  and  $\phi$ . As shown in Fig. 3.6, we describe the refracted light ray path using the refraction angle ( $Re$ ), which acts about the vertex of refraction ( $B$ ), and the refractive height ( $S$ ).

We simplify the geometry in Fig. 3.6 by defining a refraction corrected or atmosphere-free Sun-satellite angle ( $\bar{\omega}$ ). We show the geometry relating  $\omega$  to  $\bar{\omega}$  in Fig. 3.7. Because the ray geometry is symmetric to the axis  $GB$ , both  $GA$  and  $GC$  have the length  $r \sin \theta$ . We find the angle  $\theta$  both in  $J$  (the satellite) and in  $D$  (the point on the un-refracted ray that has the distance  $r$  to the Earth center at  $G$ ). The angles  $\angle CGJ$  and  $\angle AGD$  are the same, and as a consequence we have:

$$\bar{\omega} = \omega - 2Re(h_g) \quad (3.33)$$

This means that, when we know refraction angle ( $Re$ ), we can make the transition to the atmosphere-free case with  $\theta$  in  $D$ , and we can use  $\bar{\omega}$  instead of  $\omega$  in the geometric formulas going forward. Using triangle  $GBJ$  in Fig. 3.7, we can prove that the following equation must be satisfied for the light ray grazing height:

$$h_g = \frac{r \sin \theta}{\cos Re(h_g)} - R_{\oplus} - S(h_g) \quad (3.34)$$

Once refraction angle ( $Re$ ) and refractive height ( $S$ ) have been parameterized as a function of grazing height (see Section 2.3), we can iteratively solve for the grazing height of each

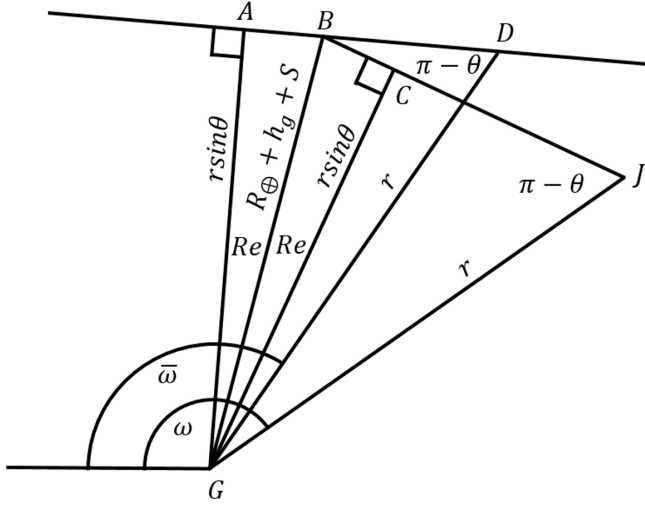


Figure 3.7: Geometry for transitioning from the actual geocentric Sun-satellite angle ( $\omega$ ) to the atmosphere-free angle ( $\bar{\omega}$ ) which simplifies our geometric relations. Point  $J$  is the satellite position and point  $D$  is the atmosphere-free position along the un-refracted ray with the same  $\theta$  angle and satellite-Earth distance ( $r$ ). Point  $B$  is the vertex of refraction and points  $A$  and  $C$  form equivalent right triangles with  $B$  and the geocenter at point  $G$ . The distance to the vertex of refraction is the sum of the Earth radius ( $R_{\oplus}$ ), grazing height ( $h_G$ ), and refractive height ( $S$ ).

ray using Eq. 3.34. Note that Eq. 3.34 is equivalent to the solution of the two expressions for the variable  $\Psi$  in Eqs. 24 and 37 in Vokrouhlický et al. (1993). Additionally, note that Eq. 37 in Vokrouhlický et al. (1993) is a misprint which is corrected in Vokrouhlický et al. (1996).

Fig. 3.8 illustrates the geometric parameters we use to solve for the overall  $\theta$  limits of the solar radiation field (which lie in the  $\phi = 0$  plane). Note that we are using the simplified un-refracted light ray geometry with  $\bar{\omega}$  instead of  $\omega$  representing the Sun-satellite angle and  $D$  instead of  $J$  representing the satellite position. Since  $D$  is now representing the satellite position,  $\theta$  is measured from  $\overline{DG}$ , and so we can use this geometry to find the overall  $\theta$  limits ( $\theta_{min}$  and  $\theta_{max}$ ). Using the triangles in Fig. 3.8 we can solve for the  $\delta$  and  $\gamma$  angles and distance  $d$ :

$$d = \sqrt{R^2 + r^2 - 2Rr \cos \bar{\omega}} \quad (3.35)$$

$$\sin \gamma = \frac{R \sin \bar{\omega}}{d} \quad (3.36)$$

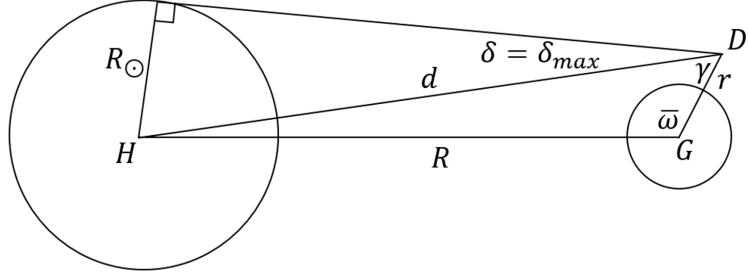


Figure 3.8: Geometry involved in computing the overall  $\theta$  limits of the solar radiation field, which lie in the  $\phi = 0$  plane. Points  $H$  and  $G$  are the center of the Sun and geocenter, respectively. Point  $D$  and angle  $\bar{\omega}$  are the atmosphere-free satellite position and Sun-satellite angle illustrated in Fig. 3.7. The angles  $\gamma$  and  $\delta_{max}$  are computed based on the satellite-Sun distance ( $d$ ), satellite-Earth distance ( $r$ ), and the Sun-Earth distance ( $R$ ) and used to compute the overall  $\theta$  limits.

$$\delta = \begin{cases} \theta - \gamma & \text{if } \theta \geq \gamma \\ \gamma - \theta & \text{if } \theta < \gamma \end{cases} \quad (3.37)$$

To solve for the  $\theta$  limits, we use the  $\delta = \delta_{max}$  geometry in Fig. 3.8 and Eqs. 3.35 and 3.36 to show that:

$$\sin \delta_{max} = \frac{R_\odot}{d} \quad (3.38)$$

$$\theta_{max} = \gamma + \delta_{max} = \arcsin\left(\frac{R \sin \bar{\omega}}{d}\right) + \arcsin\left(\frac{R_\odot}{d}\right) \quad (3.39)$$

Similarly, we can compute the lower  $\theta$  limit by subtracting  $\delta_{max}$ :

$$\theta_{min} = \gamma - \delta_{max} = \arcsin\left(\frac{R \sin \bar{\omega}}{d}\right) - \arcsin\left(\frac{R_\odot}{d}\right) \quad (3.40)$$

Note that the presence of  $\bar{\omega}$  in the above equations for  $\theta_{min}$  and  $\theta_{max}$  connects the solution of these parameters to refraction angle ( $Re$ ) (see Eq. 3.33) and therefore grazing height ( $h_g$ ). The expression for grazing height must be fed into this solution process and solving the  $\theta$  limits requires an iterative method driven by refraction angle ( $Re$ ) and refractive height ( $S$ ) tables.

Due to our choice of reference frame and spherical coordinates, solving for the overall  $\phi$  limits of the solar radiation field is relatively simple. Changes in  $\phi$  do not result in changes in grazing height. Therefore, there is no atmospheric distortion of the overall limits of the

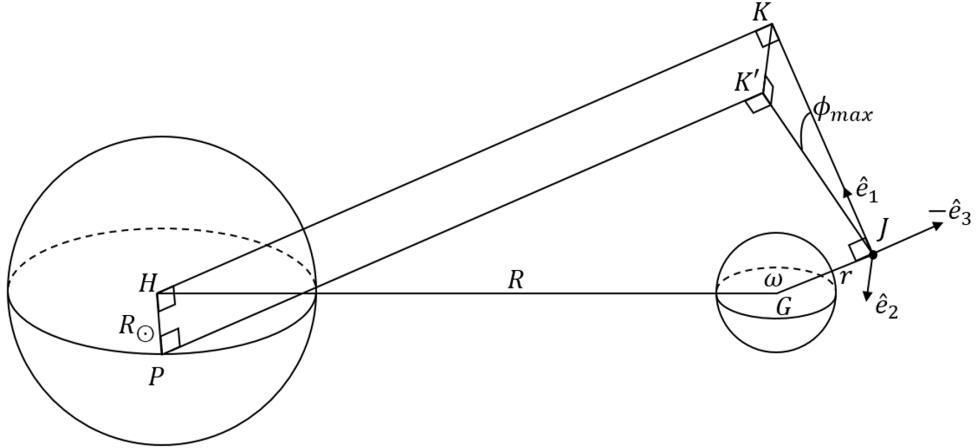


Figure 3.9: Geometry involved in computing the overall  $\phi$  limits of the solar radiation field, which occur at  $\pm\phi_{max}$  where the light ray is emitted from and tangent to point  $P$  on the Sun. Points  $H$ ,  $G$ , and  $J$  are the Sun center, geocenter, and satellite position, respectively.  $K$  is the projection the Sun center onto the  $\hat{e}_1$ - $\hat{e}_2$  plane.  $R$  is the Sun-Earth distance,  $R_\odot$  is the Solar radius,  $r$  is the satellite-Earth distance, and  $\omega$  is the Sun-satellite angle.

solar radiation field in  $\phi$ , and solar radiation fields are symmetric such that the  $\phi$  limits are simply  $\pm\phi_{max}$ . Using the shape in Fig. 3.9 defined by points  $H$ ,  $G$ ,  $J$ , and  $K$ , we can show that  $\overline{KJ} = R \sin(\omega)$ . With this side length of triangle  $KJK'$ , which lies in the  $\hat{e}_1$ - $\hat{e}_2$  plane, we can show that:

$$\phi_{max} = \angle KJK' = \arcsin \left( \frac{R_\odot}{R \sin \omega} \right) \quad (3.41)$$

For non-zero  $\phi$  slices of the solar radiation field, we must generalize the geometric formulas we developed for  $\phi = 0$  (i.e. Eqs. 3.35 through 3.40) to allow the calculation of  $\theta$  limits and the angle of emission ( $\beta$ ). To accomplish this, we slice the Sun in  $\phi$ , and replace the solar radius ( $R_\odot$ ), geocentric distance to the Sun ( $R$ ), and atmosphere-free Sun-satellite angle ( $\bar{\omega}$ ) with the corresponding parameters in this 2-dimensional  $\phi$  plane. Using these adjusted values for the constant  $\phi$  plane ( $R'_\odot$ ,  $R'$ , and  $\bar{\omega}'$ ) in the place of their corresponding values in Eqs. 3.35 to 3.40 accounts for non-zero  $\phi$  angles.

Fig. 3.10 illustrates the geometry involved in this generalization to non-zero  $\phi$  angles. Using triangle  $HGH'$  in Fig. 3.10, where the angle  $\angle HGH'$  is  $\phi$ , we can compute the distance  $\overline{HH'}$  as:

$$\overline{HH'} = R \sin \bar{\omega} \sin \phi \quad (3.42)$$

With this  $\overline{HH'}$  distance and the triangle  $HE'H'$ , we can define the radius of a  $\phi$  slice of the

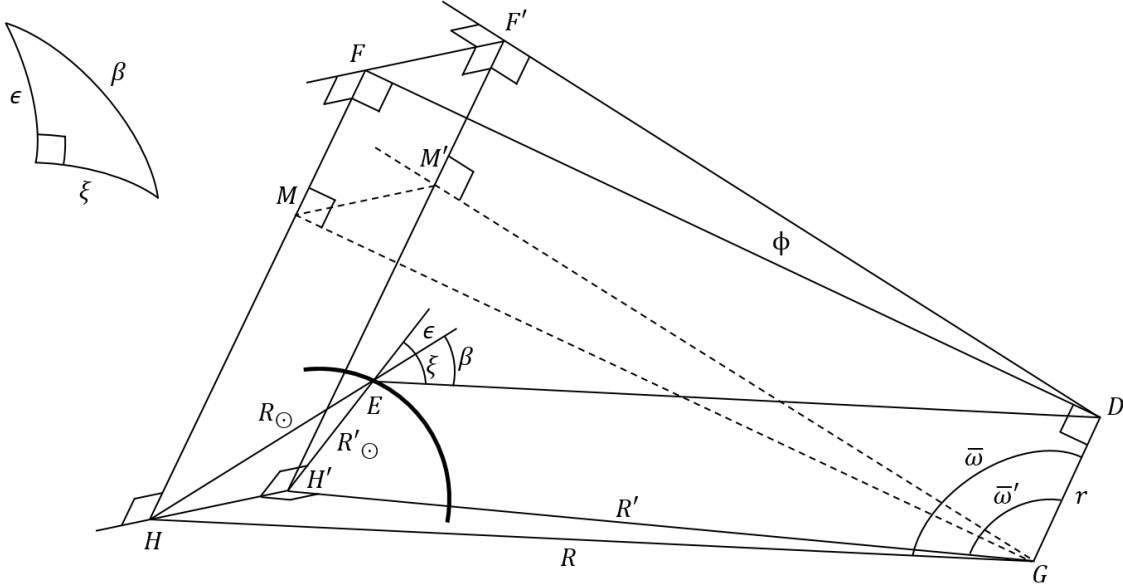


Figure 3.10: Geometry involved in slicing the Sun in  $\phi$  to compute  $\theta$  limits for non-zero  $\phi$  angles and light ray angles of emission ( $\beta$ ). Points  $H$ ,  $G$ ,  $E$ , and  $D$  are the Sun center, geocenter, location of emission, and atmosphere-free satellite position, respectively.  $R_{\odot}$  is the solar radius,  $R$  is the geocentric distance to the Sun center,  $r$  is the satellite-Earth distance, and  $\bar{\omega}$  is the atmosphere-free Sun-satellite angle. Points  $F$  and  $M$  and angles  $\epsilon$  and  $\xi$  are used in intermediate steps towards describing the non-zero  $\phi$  geometry. Parameters with a prime ('') denote values in the non-zero  $\phi$  plane corresponding to those in the  $\phi = 0$  plane.

Sun as:

$$R'_{\odot} = \sqrt{R_{\odot}^2 - \overline{HH'}^2} = R_{\odot} \sqrt{1 - \frac{R^2}{R_{\odot}^2} \sin^2 \bar{\omega} \sin^2 \phi} \quad (3.43)$$

Again using the triangle  $HGH'$ , we can define the distance to the center of a  $\phi$  slice on the Sun as:

$$R' = \sqrt{R^2 - \overline{HH'}^2} = R \sqrt{1 - \sin^2 \bar{\omega} \sin^2 \phi} \quad (3.44)$$

To develop an equation for atmosphere-free Sun-satellite angle for a  $\phi$  slice of the Sun ( $\bar{\omega}'$ ), we first use the distance  $\overline{MG} = R \sin \bar{\omega}$  and triangle  $HGM$  from Fig. 3.10 to show that:

$$\overline{HM} = \overline{H'M'} = R \cos(\bar{\omega}) = R' \cos(\bar{\omega}') \quad (3.45)$$

With this distance and Eq. 3.44, we can define the  $\bar{\omega}$  angle for a  $\phi$  slice of the Sun as:

$$\bar{\omega}' = \arccos [\cos \bar{\omega} (1 - \sin^2 \bar{\omega} \sin^2 \phi)^{-0.5}] \quad (3.46)$$

Note that Vokrouhlický et al. (1993) erroneously include a factor  $R_\odot$  in Eq. 3.46. This misprint is corrected in Vokrouhlický et al. (1996).

We replace the solar parameters in Eqs. 3.35, 3.39, and 3.40 with their adjusted values to give the  $\theta$  limits for arbitrary  $\phi$  angles ( $\theta'_{min}$  and  $\theta'_{max}$ ):

$$d' = \sqrt{R'^2 + r^2 - 2R'r \cos \bar{\omega}} \quad (3.47)$$

$$\theta'_{max} = \arcsin \left( \frac{R' \sin \bar{\omega}'}{d'} \right) + \arcsin \left( \frac{R'_\odot}{d'} \right) \quad (3.48)$$

$$\theta'_{min} = \arcsin \left( \frac{R' \sin \bar{\omega}'}{d'} \right) - \arcsin \left( \frac{R'_\odot}{d'} \right) \quad (3.49)$$

Now, we can define a complete  $\theta$ - $\phi$  boundary of the solar radiation field by first computing the overall  $\phi$  limits using Eq. 3.41 and then computing the  $\theta$  limits at each value of  $\phi$  using Eqs. 3.48 and 3.49.

Finally, we have to define an expression for the light ray angle of emission ( $\beta$ ) so that we can account for solar limb darkening (see Eq. 3.27). At the light ray emission point ( $E$ ) on the surface of a solar  $\phi$  slice, we define the projection of the angle of emission ( $\beta$ ) onto the constant  $\phi$  plane ( $\xi$ ). This projection of  $\beta$  is computed using  $d'$  and the  $\phi$  solar slice  $\gamma$  and  $\delta$  angles ( $\gamma'$  and  $\delta'$ ) which are obtained in analogy to Eqs. 3.36 and 3.37 for  $\phi = 0$ :

$$\gamma' = \arcsin \left( \frac{R' \sin \bar{\omega}'}{d'} \right) \quad (3.50)$$

$$\delta' = \begin{cases} \theta - \gamma' & \text{if } \theta \geq \gamma' \\ \gamma' - \theta & \text{if } \theta < \gamma' \end{cases} \quad (3.51)$$

$$\sin \xi = \frac{d' \sin \delta'}{R'_\odot} \quad (3.52)$$

The angle  $\epsilon$  between the solar surface normal at the location of emission and the constant  $\phi$  plane and is obtained with:

$$\cos \epsilon = \frac{R'_\odot}{R_\odot} = \sqrt{1 - \frac{R^2}{R_\odot^2} \sin^2 \bar{\omega} \sin^2 \phi} \quad (3.53)$$

where Eq. 3.44 has been used. The relation between  $\xi$ ,  $\beta$ , and  $\epsilon$  is obtained using the spherical geometry in the upper left of Fig. 3.10 (Napier's Rule at the location of emission ( $E$ )):

$$\cos \beta = \cos \epsilon \cos \xi \quad (3.54)$$

## 3.4 SOLAARS Implementation

We now have the key formulas needed to establish a computational framework for the SOLAARS penumbra SRP model. Fig. 3.11 illustrates the steps used to compute SRP acceleration at a given location during a penumbra transition. The flowchart includes references to the key equations required to complete each part of the process. First, we input a mean solar radiance, satellite and Sun position, and set of atmospheric effects tables to use in SRP modeling (developed in the following Sections 3.5 and 3.6). The atmospheric effects tables are grazing height profiles of refraction angle ( $Re$ ), refractive height ( $S$ ), and radiance coefficients for each spectral bin ( $\bar{L}_j$ ). The process outlined in the oblateness modeling implementation flowchart (Fig. 3.4) is used to set a spherical Earth radius and adjusted Sun and satellite positions. Eq. 3.41 is used to compute the  $\phi$  limits of the solar disc ( $\pm\phi_{max}$ ). Note that the un-adjusted values of solar radius ( $R_\odot$ ) and Sun-satellite angle ( $\omega$ ) are used in Eq. 3.41. Then, we iterate over a finite number of  $\phi$  angles distributed over  $\pm\phi_{max}$ .

In the "iterate over  $\phi$ " loop, we first compute the adjusted non-zero  $\phi$  values of solar radius ( $R'_\odot$ ), Earth-Sun distance ( $R'$ ), and atmosphere-free Sun-satellite angle ( $\bar{\omega}'$ ). We use these adjusted variables to numerically solve for the  $\theta$  limits of each  $\phi$  slice of the solar disc ( $\theta'_{min}$  and  $\theta'_{max}$ ), then iterate over a finite number of  $\theta$  angles distributed over these limits. In the "iterate over  $\theta$ " loop, we compute the properties and differential contribution of a single light ray to the total SRP acceleration. After the  $\theta$  and  $\phi$  loops are complete, and the differential contribution of each light ray used to approximate the solar radiation field has been computed, these values are added according to Eq. 3.32 to yield the total SRP acceleration of the satellite. What remains is to create the atmospheric effects tables.

## 3.5 Refraction parameters

As we described in the previous section, we capture the effects of atmospheric refraction on the path of a light ray using two parameters: refraction angle ( $Re$ ) and refractive height ( $S$ ). Using the method presented by Auer and Standish (2000), we can solve for and tabulate refraction angle ( $Re$ ) and refractive height ( $S$ ) as a function of grazing height ( $h_g$ ).

We apply the method from Auer and Standish (2000) with different, tabulated atmospheric density profiles. This approach allows us to precisely calculate the refracted light ray path

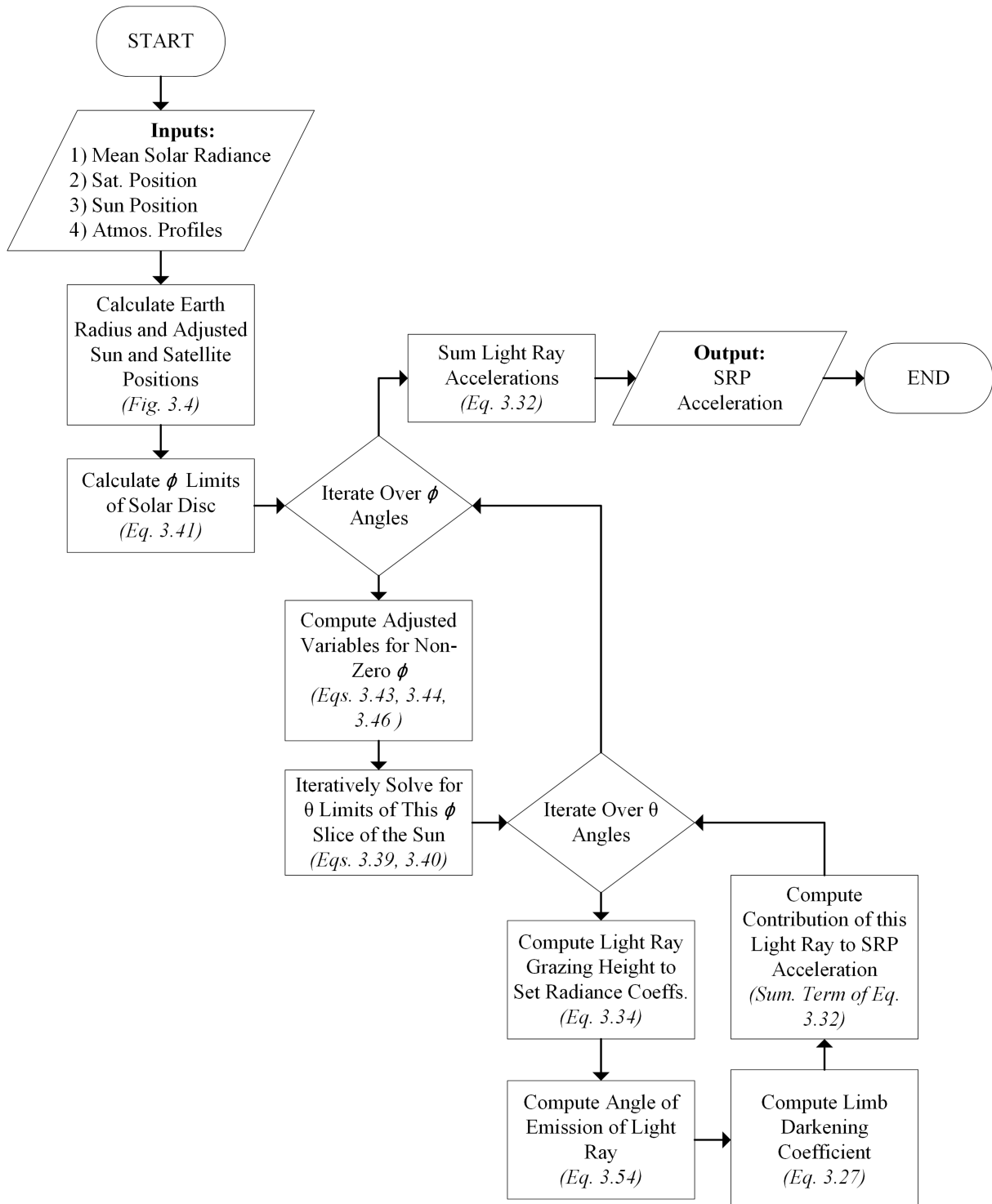


Figure 3.11: Flowchart for software implementation of the SOLAARS model. This process is repeated at each satellite position.

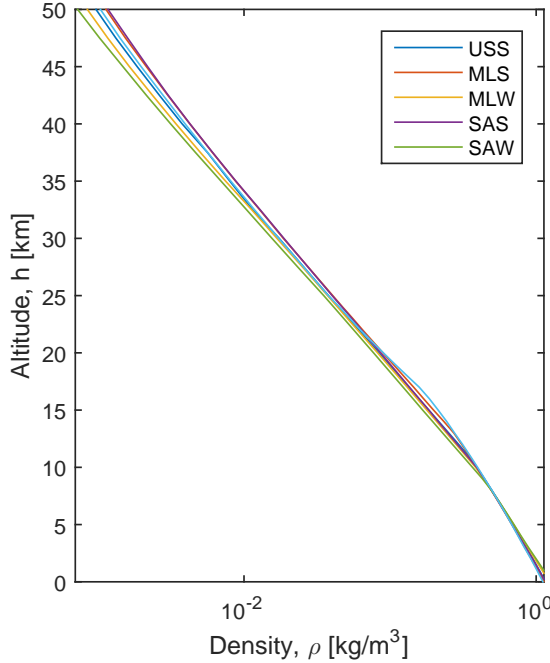


Figure 3.12: Density profiles for the standard atmosphere profiles used in the SOLAARS model.

through the atmosphere, and, unlike the other methods mentioned, allows us to use the atmospheric density profile of our choice. In our modeling of atmospheric effects, we use an atmosphere height of  $h_T = 50$  km and the atmosphere profiles from the 1966 US standard atmosphere supplements (COESA, 1966), which include tropical (T), subarctic winter (SAW), subarctic summer (SAS), midlatitude winter (MLW), midlatitude summer (MLS), and US standard (USS) atmospheres. Fig. 3.12 shows the density profiles of these different standard atmospheres.

The method from Auer and Standish (2000) involves numerical integration over the light ray path in the angle  $\psi$ , which is illustrated in Fig. 3.13. We compute indices of refraction at each  $\psi$  angle ( $\eta_\psi$ ) as a function of atmospheric density ( $\rho$ ) at the corresponding altitude ( $h_\psi$ ) using the Gladstone-Dale relation:

$$\eta_\psi = 1 + \alpha \rho(h_\psi) \quad (3.55)$$

$$\alpha = 0.00029241$$

where the value of  $\alpha$  given here is the correct value, different from the one given in Auer and Standish (2000), which is a misprint.

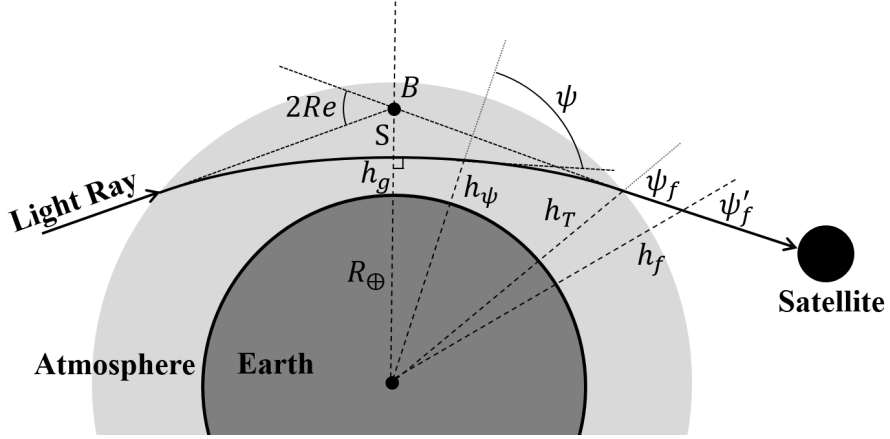


Figure 3.13: Geometric parameters involved in modeling refraction. In this illustration, point  $B$  is the vertex of refraction,  $h_g$  is the light ray grazing height,  $\psi$  is the angle of the light ray with respect to the local vertical, and  $h_\psi$  is the height of the light ray at a particular  $\psi$  angle. The angle  $\psi_f$  is the final value of  $\psi$  where the light ray has left the atmosphere at the atmosphere height ( $h_T = 50\text{ km}$ ) and  $\psi'_f$  is the value of  $\psi$  which we use in the place of  $\psi_f$  which is located at some height  $h_f > h_T$ . The refractive height ( $S$ ) is the distance between the point  $B$  and the light ray grazing point at the grazing height ( $h_g$ ).

The following equation from Auer and Standish (2000) provides refraction angles based on numerical integration over the angle  $\psi$ :

$$Re(h_g) = - \int_{\frac{\pi}{2}}^{\psi_f} \frac{-\frac{d\ln(\eta_\psi)}{d\ln(r_\psi)}}{1 + \frac{d\ln(\eta_\psi)}{d\ln(r_\psi)}} d\psi \quad (3.56)$$

where:

$$r_\psi = R_\oplus + h_\psi$$

Due to the geometry of our problem shown in Fig. 3.13, the upper limit in the refraction angle integrand ( $\psi_f$ ) is related to refraction angle ( $Re$ ) and refractive height ( $S$ ):

$$\psi_f = \arcsin \left( \frac{(R_\oplus + h_g + S) \cos(Re)}{R_\oplus + h_T} \right) \quad (3.57)$$

Clearly, we do not yet know the refraction angle or refractive height. Alternatively, we could integrate all the way to the satellite location, where  $\psi = \pi - \theta$ . However, since it is necessary to calculate refraction angles as a function of grazing height alone,  $\theta$  is not known at the time of refraction angle calculation. The refraction angle can be computed for arbitrary  $\theta$

values by simply setting it to a conservatively low value ( $\psi'_f$ ). We define this conservatively low value as the value of  $\psi$  at the top of the atmosphere for an unrefracted light ray:

$$\psi'_f = \arcsin \left( \frac{R_{\oplus} + h_g}{R_{\oplus} + h_T} \right) \leq \psi_0 \quad (3.58)$$

Using this upper integration limit guarantees that the ray has left the atmosphere and the integrand has gone to zero before integration is complete. The natural log derivatives can be computed using the height associated with each  $\psi$  angle and the corresponding refractive index ( $\eta_{\psi}$ ) and refractive index derivative ( $\frac{d\eta_{\psi}}{dh_{\psi}}$ ) at that height as:

$$\frac{d\ln(\eta_{\psi})}{d\ln(r_{\psi})} = \frac{d\ln(\eta_{\psi})}{d\eta_{\psi}} \frac{d\eta_{\psi}}{dr_{\psi}} \frac{dr_{\psi}}{d\ln(r_{\psi})} = \frac{(h_{\psi} + R_{\oplus})}{\eta_{\psi}} \frac{d\eta_{\psi}}{dh_{\psi}} \quad (3.59)$$

The height of the light ray at each angle  $\psi$  must be computed using a numerical method. Auer and Standish provide a light ray height error function ( $f$ ) and its derivative ( $\frac{df}{dh_{\psi}}$ ), which can be used in a Newton-Raphson iterative scheme to compute the ray height ( $h_{\psi}$ ) for each evaluation of the integrand in Eq. 3.56:

$$f(h_{\psi}) = \eta_{\psi}(R_{\oplus} + h_{\psi}) - \frac{\eta_{\psi}(R_{\oplus} + h_{\psi})\sin(\psi'_f)}{\sin(\psi)} \quad (3.60)$$

$$\frac{df}{dh_{\psi}}(h_{\psi}) = \frac{d\eta_{\psi}}{dh_{\psi}}(R_{\oplus} + h_{\psi}) + \eta_{\psi} \quad (3.61)$$

As we have shown in Section 2.2, we use the straight-line light ray geometry occurring about the point  $B$  to address the effects of refraction. As a result of this approach, we must tabulate the refractive height ( $S$ ) as a function of grazing height to give us the location of the vertex of refraction. Once refraction angle has been computed, we calculate the refractive height using the geometry in Fig. 3.13:

$$S(h_g) = (R_{\oplus} + h_f) \frac{\sin(\psi'_f)}{\cos Re} - R_{\oplus} - h_g \quad (3.62)$$

where  $h_f$  is the height computed in using Newton-Raphson iteration for  $\psi = \psi'_f$ .

The different refraction angle profiles which result from each of these standard atmospheres are shown in Fig. 3.14. The differences in density profiles shown in Fig. 3.12 have clearly translated into these refraction modeling results, especially at lower altitudes. The subarctic winter and tropical atmospheres, which lie at opposite extremes of climate, show the most significant levels of disagreement. Fig. 4.10a compares penumbra SRP results from these various atmosphere models. In all cases shown in Fig. 3.14, the refraction parameters have

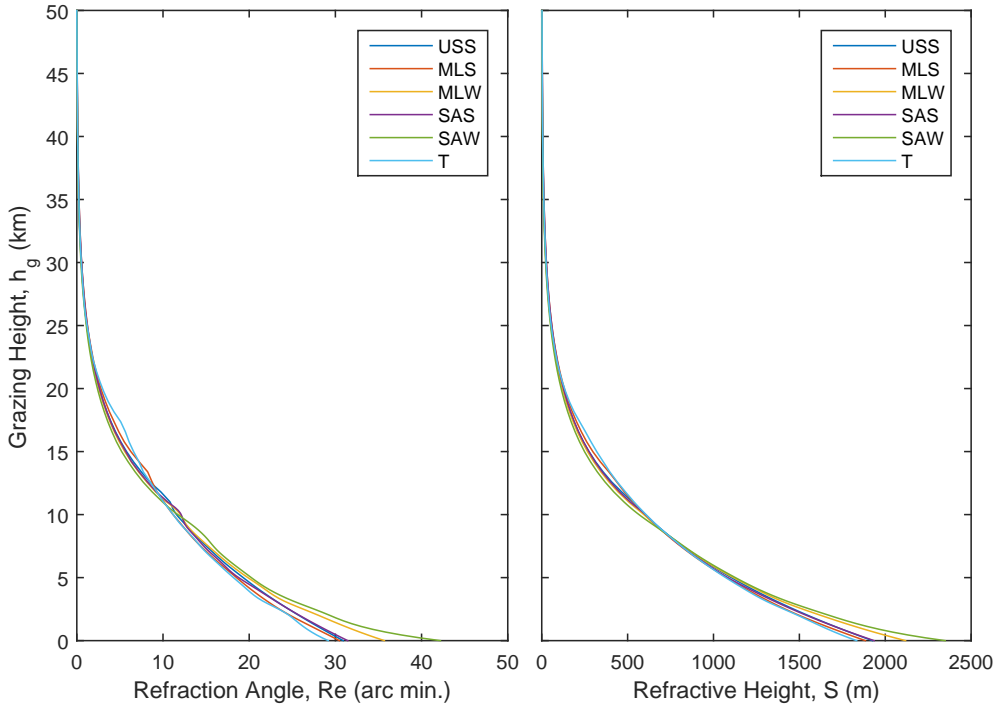


Figure 3.14: Refraction angle ( $Re$ ) and refractive height ( $S$ ) profiles computed using each of the standard atmospheres used in the SOLAARS model.

gone close to zero before 50 km which shows that we are modeling using a sufficiently high atmosphere height to capture the effects of atmospheric refraction.

## 3.6 Radiance coefficients

Our objective in this section is to generate radiance coefficients as a function of light ray grazing height, which we can use to calculate the radiance of each light ray in each spectral bin. These radiance coefficients are unitless numbers between zero and one which, when multiplied by the mean solar radiance ( $L_{\odot}$ ), account for the spectral composition of sunlight (i.e. the fraction of sunlight in the  $j^{th}$  spectral bin) and atmospheric extinction effects. Four processes contribute significantly to total atmospheric extinction: Rayleigh scattering by dry air, molecular absorption, aerosol extinction, and cloud extinction. We will begin by introducing the geometry and high level formulas that we use to consider these effects, then we will describe how the transmittance coefficient ( $\mathbb{T}$ ) for each process is computed as a function of grazing height ( $h_g$ ) and spectral bin wavelength boundaries ( $\lambda_j^-$  and  $\lambda_j^+$ ). Finally, we will use results from an established atmospheric radiative transfer code to validate our

extinction model.

In their modeling of atmospheric extinction, Vokrouhlický et al. (1993) only consider Rayleigh scattering, and experiment with cloud effects by increasing their Rayleigh scattering coefficient at certain altitudes. While Rayleigh scattering is the primary source of atmospheric extinction at grazing heights below 30 km, our results show that the other processes mentioned above contribute significantly. Fig. 3.15 illustrates the significance of these other processes by comparing the solar spectra computed with only Rayleigh scattering effects to those computed using the full SOLAARS model. While the significance of neglecting other extinction processes varies with grazing height, even under the assumption of a cloudless atmosphere, modeling only Rayleigh scattering leads to an underestimate of total extinction by at least 35%.

Three of the extinction processes we model have strong spectral dependence. Therefore, it is necessary to consider the spectral distribution of solar radiation incident on the atmosphere. One could use a black body description of the extraterrestrial solar spectral irradiance (SSI) for this, as Vokrouhlický et al. (1993) did, to give analytical formulas for some of the extinction parameters. However, computational cost is not a concern in this step (see Fig. 3.2), and so it is logical to take advantage of a more accurate SSI data set. We use the American Society for Testing and Materials (ASTM) standard zero-air-mass SSI tables, which are based on modeling and ground based, spacecraft, and high-altitude aircraft measurements (ASTM, 2014). We use the ASTM SSI ( $E_0$ ), tabulated as a function of wavelength ( $\lambda$ ) and normalize it to yield a normalized extraterrestrial SSI ( $\bar{E}_0$ ):

$$\bar{E}_0(\lambda) = \frac{E_0(\lambda)}{\int_{119.5\text{nm}}^{6000\text{nm}} E_0(\lambda) d\lambda} \quad (3.63)$$

Note that the integral in Eq. 3.63 is evaluated numerically from the smallest wavelength of 119.5 nm in the ASTM tables to 6000 nm, which does not include the tabulated ASTM irradiances between above 6000 nm, but captures over 99.7 % of the optical power. By normalizing the ASTM data set such that its corresponding wavelength integrated value (or total solar irradiance) is equal to 1, we always assume the ASTM spectral distribution, but can account for variations in the mean solar radiance ( $L_\odot$ ) with solar activity.

We calculate the normalized SSI after atmospheric extinction ( $\bar{E}$ ) for a light ray with a particular grazing height ( $h_g$ ) by multiplying the normalized extraterrestrial SSI ( $\bar{E}_0$ ) by the transmittances associated with each extinction process:

$$\bar{E}(\lambda, h_g) = \bar{E}_0(\lambda) \mathbb{T}_r(\lambda, h_g) \mathbb{T}_a(\lambda, h_g) \mathbb{T}_m(\lambda, h_g) \mathbb{T}_c(h_g) \quad (3.64)$$

where  $\mathbb{T}_r$ ,  $\mathbb{T}_a$ ,  $\mathbb{T}_m$  and  $\mathbb{T}_c$  are the transmittances associated with Rayleigh scattering, aerosol extinction, molecular absorption, and cloud extinction, respectively. Once this spectrum after extinction ( $\bar{E}$ ) is computed, we numerically integrate over our desired spectral bins to

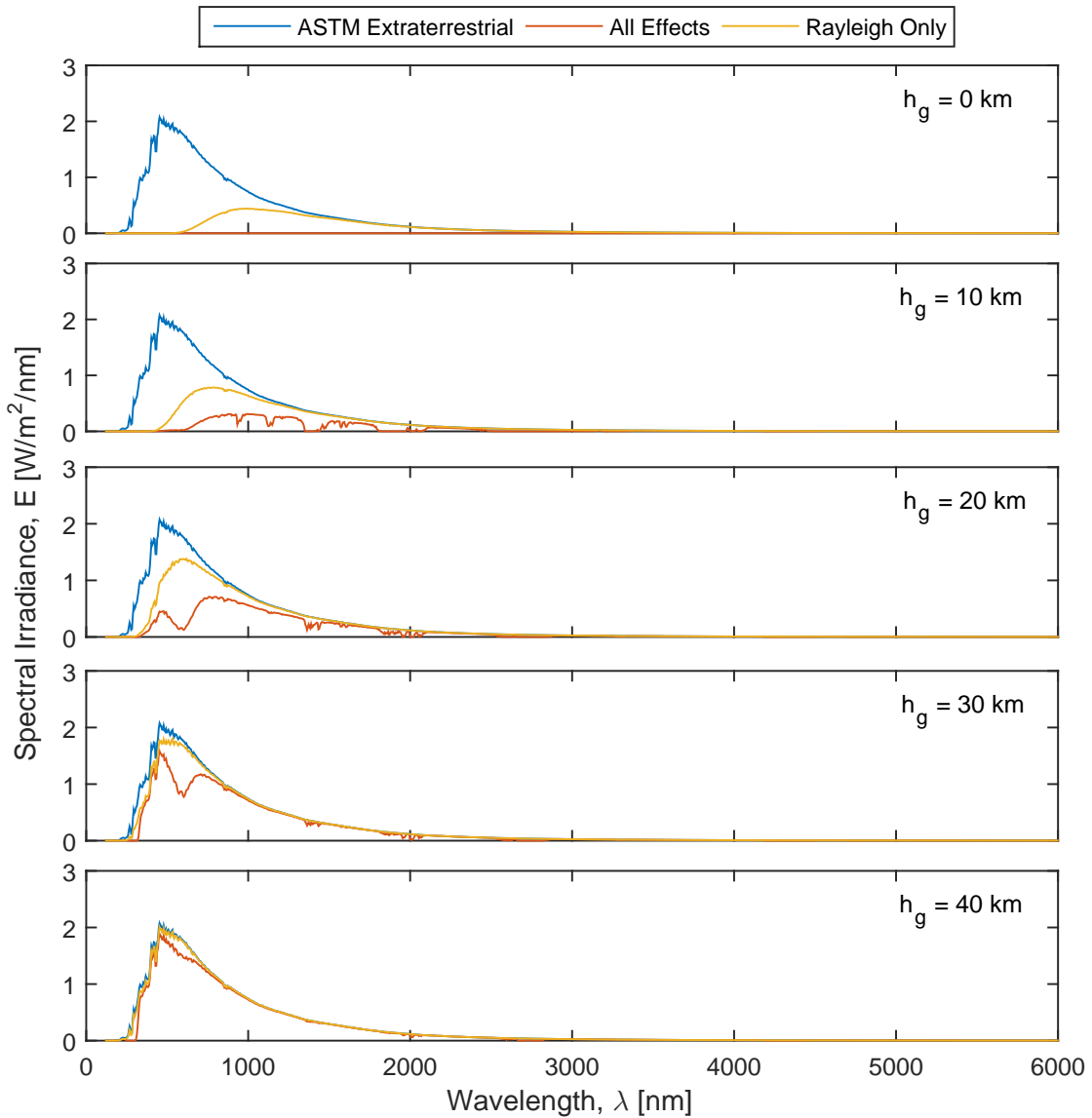


Figure 3.15: Solar spectrals for light rays with different grazing heights. The initial, extraterrestrial spectrum and spectra computed with only Rayleigh scattering effects are included for comparison.

compute the radiance coefficient for each bin:

$$\bar{L}_j(h_g) = \int_{\lambda_j^-}^{\lambda_j^+} \bar{E}(\lambda, h_g) d\lambda \quad (3.65)$$

where  $\lambda_j^-$  and  $\lambda_j^+$  are the upper and lower limits of the  $j_{th}$  bin, respectively and  $\lambda_j$  is the center wavelength. This integral is evaluated numerically over  $\bar{E}$  which, for each value of grazing height in the extinction parameter tables, is computed over the entire spectrum of  $\bar{E}_0$  with a spectral bin of width ( $\Delta\lambda$ ) of 5 nm. With this very fine spectral resolution of the attenuated SSI spectrum, we can assume it will not limit the accuracy of our numerical integration in Eq. 3.65, which will separate the solar spectrum into much larger spectral bins for SRP modeling (i.e.  $\lambda_j^+ - \lambda_j^- \gg \Delta\lambda$ ).

We compute transmittances for a particular wavelength ( $\lambda$ ) from the wavelength integrated average of Bouguers law for transmittance with the spectral bin centered at  $\lambda$ :

$$\mathbb{T}(\lambda, h_g) = \frac{1}{\Delta\lambda} \int_{\lambda-\Delta\lambda/2}^{\lambda+\Delta\lambda/2} e^{-2\tau(\lambda, h_g)} d\lambda \quad (3.66)$$

where  $\tau$  is the half optical thickness associated with the extinction process being addressed. For each process, we assume the same path through the atmosphere, which we must integrate over to compute  $\tau$ . Like Vokrouhlický et al. (1993), we assume a spherically symmetric atmosphere. This assumption allows us to simply double the optical thickness associated with half of the symmetric light ray path through the atmosphere, as shown in the exponential of Eq. 3.66. We integrate over the distance  $s$  along an approximation of this half-path through the atmosphere. The geometry of this approximate light ray path is shown in Fig. 3.16. The upper limit of half optical thickness integration, the distance to the top of the atmosphere ( $s_T$ ) can be defined as:

$$s_T = \sqrt{(h_T + R_\oplus)^2 - (h_g + R_\oplus)^2} \quad (3.67)$$

and the height associated with a given distance  $s$  as:

$$h_s = \sqrt{(h_g + R_\oplus)^2 + s^2} - R_\oplus \quad (3.68)$$

We have established the fundamental equations needed to populate radiance coefficient tables using Eq. 3.65. In Sections 3.6.1, 3.6.2, 3.6.3, and 3.6.4, we will compute half optical thickness ( $\tau$ ) for use in Eq. 3.66 (or transmittance ( $\mathbb{T}$ ) directly) for Rayleigh scattering, aerosol extinction, molecular absorption, and cloud extinction. Fig. 3.17 shows a set of transmittance results computed for a range of grazing heights using the methods we will describe in

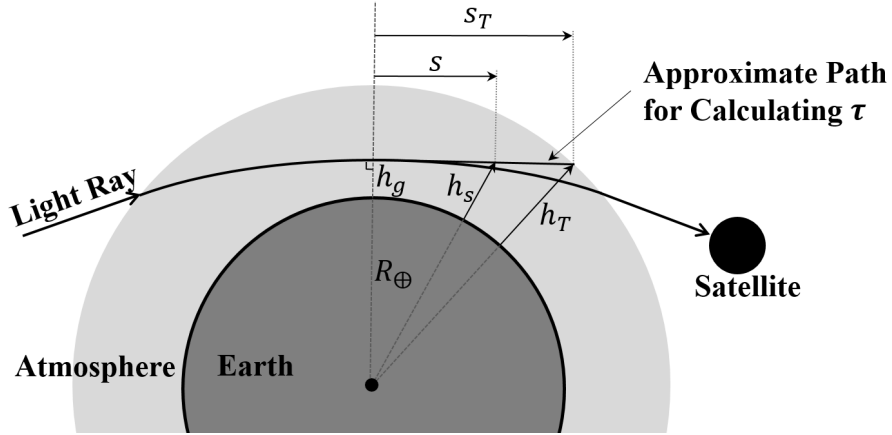


Figure 3.16: Geometric parameters involved in modeling extinction processes.  $R_{\oplus}$  is the Earth radius,  $h_T$  is the height of the top of the atmosphere (50 km),  $s_T$  is the path distance from the grazing point to the top of the atmosphere,  $h_g$  is the light ray grazing height, and  $h_s$  is the height of a light ray at a path distance ( $s$ ) along the approximate light ray path.

this section. The more simple, smooth wavelength dependence of Rayleigh scattering and aerosol extinction is very different than the behavior of molecular absorption processes. The significance of aerosols and molecular absorption, which are ignored in Vokrouhlický et al. (1993), is clear.

### 3.6.1 Rayleigh scattering

Scattering of light by the atoms and molecules of a loosely packed substance (such as air in the atmosphere) can be modeled using the Lorentz theory of charged particle interactions in matter and Maxwell's theory of electromagnetic fields. Solar radiation induces an oscillating dipole state in atoms and molecules which it strikes in the atmosphere. In the case of elastic scattering, these atoms and molecules can be treated as damped harmonic oscillators which emit what we refer to as scattered radiation (Thomas (1999)). Rayleigh scattering refers to scattering of radiation by particles significantly smaller than the wavelength of the incident radiation. We ignore the scattered light, but are interested in the attenuation of solar radiation due to Rayleigh scattering along each light ray path.

Like Vokrouhlický et al. (1993), the fundamental property of the medium that we use to model Rayleigh scattering is the scattering coefficient at sea level ( $X_{r0}$ ), which is the ratio of scattered power to power carried unit distance through the scattering medium; we assume this coefficient to scale linearly with atmospheric density. While Vokrouhlický et al. (1993) gives a single  $X_{r0}$  value for the “reference wavelength” of 550 nm, we describe Rayleigh scattering as a function of wavelength. This approach allows for a more precise calculation of the wavelength integrated Rayleigh scattering coefficients and captures the significant

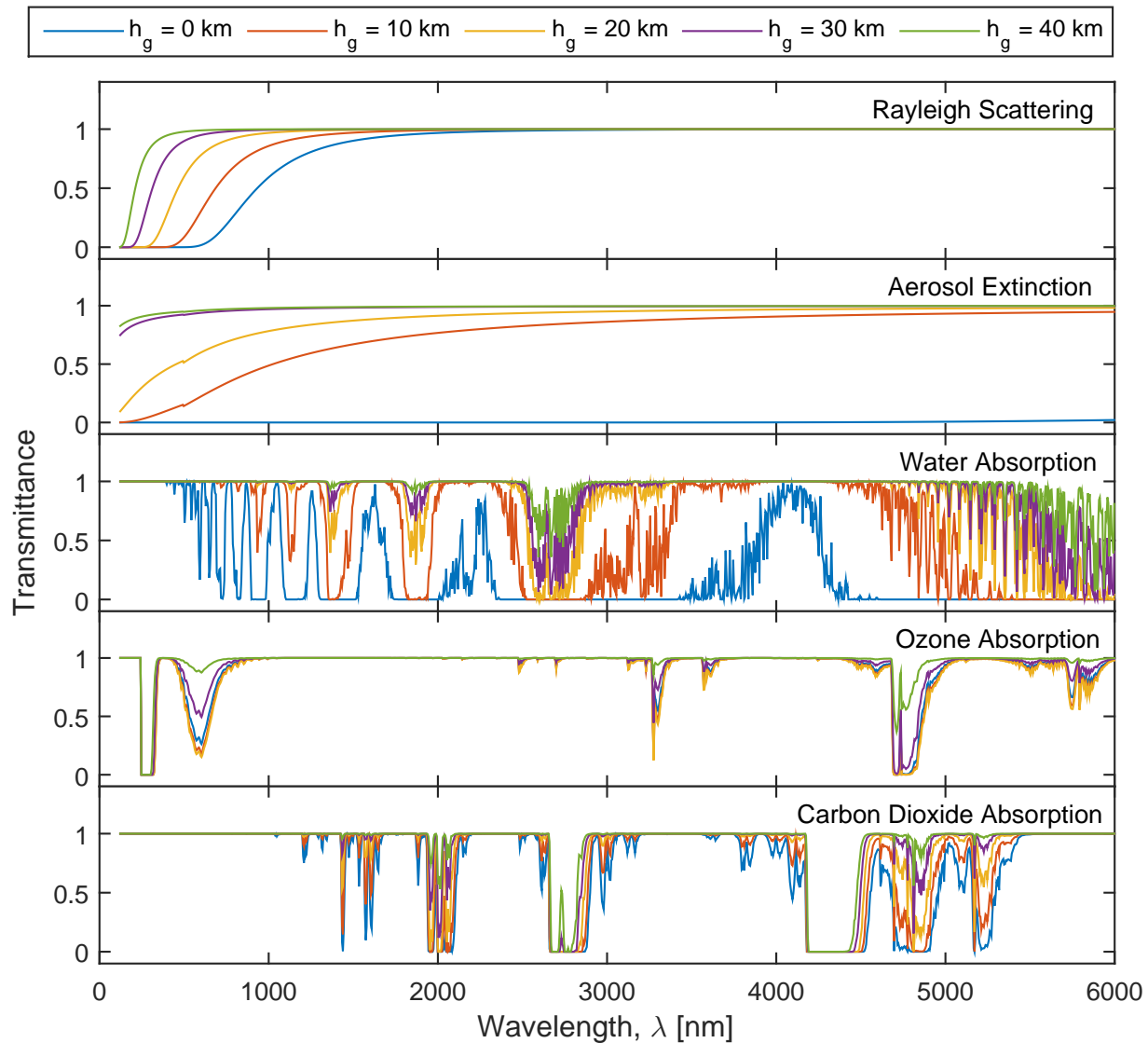


Figure 3.17: Transmittances at different grazing heights.

changes in solar spectral composition due to Rayleigh scattering. The scattering coefficient is determined by the solution of the damped harmonic oscillator model with the assumption of particles much smaller than the wavelength ( $\lambda$ ) of the radiation (Thomas and Stamnes, 2002):

$$X_{r0}(\lambda) = \frac{128\pi^5 N_0}{3\lambda^4} \alpha_{p0}^2 \quad (3.69)$$

where  $N_0$  is the molecular number density at sea level and  $\alpha_{p0}$  is the polarizability of the medium at sea level. Eq. 3.69 illustrates the wavelength dependence of Rayleigh scattering which leads to significant changes in the spectral composition of light as it passes through the atmosphere. Polarizability is a measure of the resistance of the molecules and atoms in the medium to the induced oscillating dipole behavior that causes Rayleigh scattering. Polarizability can be conveniently defined as a function of refractive index using an approximate form of the Lorentz-Lorenz equation for indices of refraction close to unity (Thomas, 1999):

$$\alpha_{p0} = \frac{\eta_0 - 1}{2\pi N_0} \quad (3.70)$$

where  $\eta_0$  the refractive index at sea level, which can be calculated from density using Eq. 3.55.

Eq. 3.69 assumes isotropic behavior of Rayleigh scattering in the atmosphere; however, the molecules are anisotropic scatterers. To account for this anisotropic scattering, we apply King's correction factor ( $C_k$ ) to the scattering coefficient. We define this factor using the formulas from Bates (1984) for the primary constituents of dry air ( $O_2$ ,  $N_2$ ,  $Ar$ , and  $CO_2$ ). We compute the weighted average of these formulas using the mole fractions of each constituent in the lower atmosphere from Picard et al. (2008) to give the King's correction factor ( $C_k$ ) for air as a function of wavelength:

$$C_k(\lambda) = 1.0467 + 5.3755 \times 10^{14} \frac{1}{\lambda^2} + 3.0321 \times 10^{36} \frac{1}{\lambda^4} \quad (3.71)$$

where wavelength ( $\lambda$ ) is in meters. Adding this correction factor to Eq. 3.69 gives the final form of the Rayleigh scattering coefficient (again with units in meters):

$$X_{r0}(\lambda) = \frac{32\pi^3(\eta_0 - 1)^2}{3N_0\lambda^4} (1.0467 + 5.3755 \times 10^{14} \frac{1}{\lambda^2} + 3.0321 \times 10^{31} \frac{1}{\lambda^4}) \quad (3.72)$$

We integrate over the approximate light ray path shown in Fig. 3.16 (in path distance ( $s$ )) to determine the half optical thickness for Rayleigh scattering ( $\tau_r$ ):

$$\tau_r(\lambda, h_g) = \frac{X_{r0}(\lambda)}{\rho_0} \int_0^{s_{max}} \rho(h_s) ds \quad (3.73)$$

where  $\rho_0$  is the atmospheric density at sea level.

### 3.6.2 Aerosol extinction

Aerosols in the atmosphere include a variety of natural and man made particles such as volcanic dust, meteoric dust, sea salt, and sulfates from burning oil and coal which vary significantly in their sizes, shapes, and optical properties. Table 18-10a from Jursa (1985), which is based on the aerosol modeling of Shettle and Fenn (1976, 1979), provides standard profiles of extinction coefficient,  $X'_a$ , for the rural model aerosol. Extinction profiles are defined for varying conditions, allowing the effects of surface meteorological range, season, volcanic activity, and upper atmosphere state to be considered. Surface meteorological range is a measure of visibility which represents the strength of atmospheric extinction at sea level. These values of  $X'_a$  are tabulated for the reference wavelength ( $\lambda'=550$  nm). To capture the wavelength dependence of aerosol extinction, we use the wavelength exponent ( $w$ ):

$$X_a(\lambda) = X'_a \left( \frac{\lambda'}{\lambda} \right)^w \quad (3.74)$$

This approach was first presented by Ångström (1929) with a constant value of the wavelength exponent between 1.0 and 1.5 over all wavelengths; however, Bird (1984) and Gueymard (2001) demonstrate the utility of using two different values. We use the rural wavelength exponents from Table B.1 in Gueymard (2001) which were computed by curve fitting to results from the MODTRAN and LOWTRAN models using the Shettle and Fenn (1979) rural reference aerosol. One value of  $w$  is used for wavelengths above 500 nm and another for wavelengths below 500 nm. Wavelength exponents from Gueymard (2001) are selected based on humidity. Using the tabulated  $X'_a$  altitude profile and wavelength exponents, we integrate along the light ray path from Fig. 3.16 to calculate the half optical thickness for aerosol extinction:

$$\tau_a(\lambda, h_g) = \left( \frac{\lambda'}{\lambda} \right)^w \int_0^{s_{max}} X'_a(h_s) ds \quad (3.75)$$

For the results presented here, we selected three sets of aerosol conditions to investigate: low, medium, and high aerosol turbidity. These three aerosol extinction profiles represent the range of possible aerosol conditions from Jursa (1985), and the conditions corresponding to these three scenarios are summarized in Table 3.1, and Fig. 3.18 shows the associated aerosol extinction coefficient profiles.

Table 3.1: Parameters used to generate the aerosol extinction profiles used here, based on data from Jursa (1985). “Background” refers to background stratospheric, i.e. an atmosphere with negligible volcanic aerosols. Seasons specified in the table are for the USS atmosphere case, and for other standard atmosphere cases the corresponding season is chosen (e.g. fall/summer is used with the sub-arctic summer standard atmosphere).

Profile	Season	Met. Range	Volcanic State	Upper Atmos. State
Low	Fall/Winter	50 km	Background	Normal
Medium	Fall/Winter	10 km	Moderate	Extreme
High	Spring Summer	2 km	Extreme	Extreme

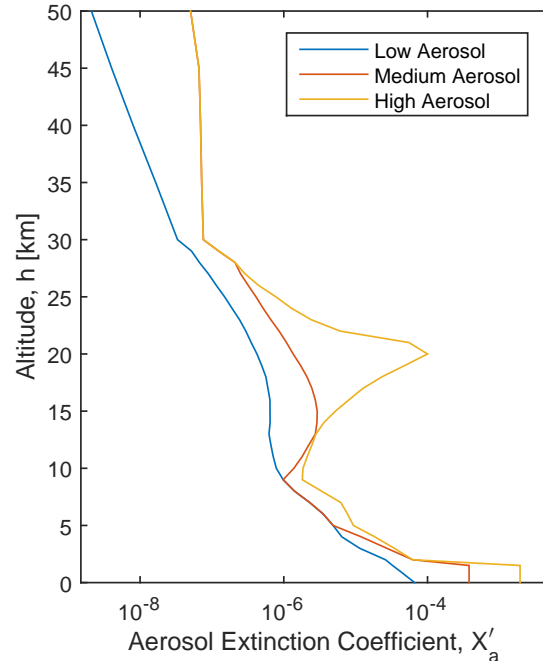


Figure 3.18: Aerosol extinction coefficient profiles for each of the scenarios described in Table 3.1.

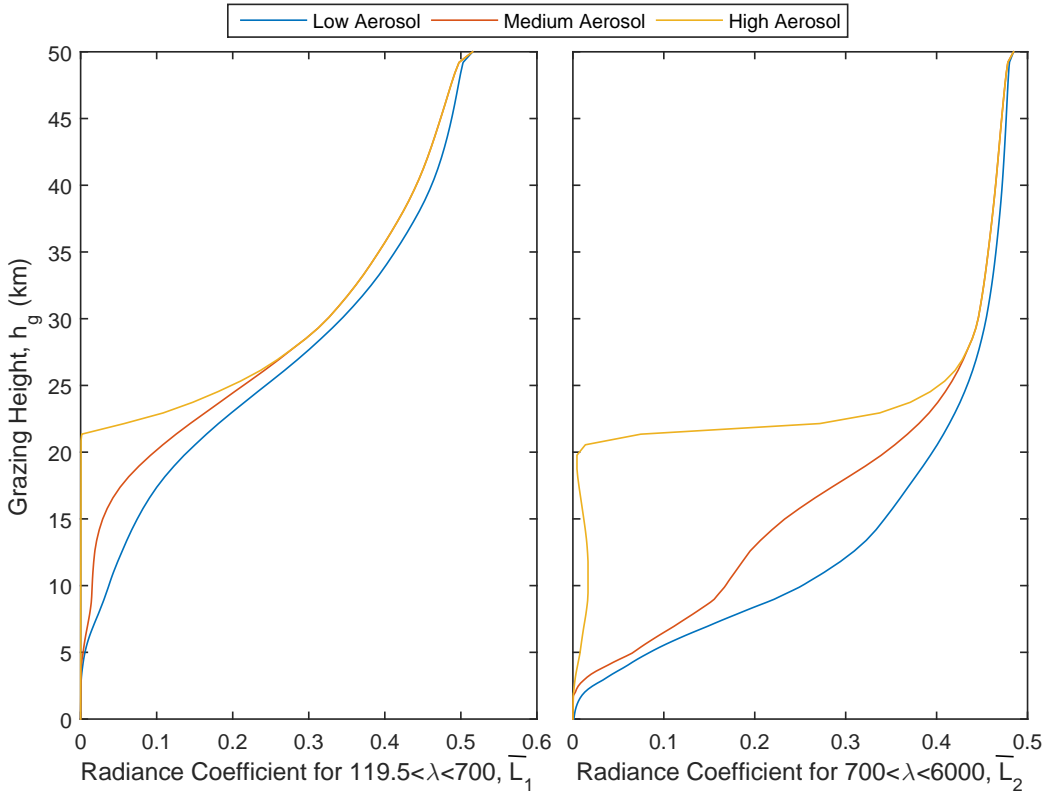


Figure 3.19: Extinction coefficient profiles for a two spectral bin model with a Visible/UV bin ( $\bar{L}_1$ ) and IR bin ( $\bar{L}_2$ ). Results are shown for each of the aerosol profiles described in Table 3.1.

The significant variation shown in Fig. 3.18 demonstrates the high level of uncertainty in aerosol extinction modeling. At some altitudes, the the aerosol extinction coefficient for the high aerosol profile is over 100 times smaller than the low aerosol value. The selection of aerosol profile significantly influences tabulated radiance coefficient values. Fig. 3.19 shows extinction coefficient profiles for a two spectral bin extinction model (i.e.  $N_b = 2$ ) for the three aerosol turbidity scenarios, with all other extinction modeling inputs held constant. The choice of a 50 km atmosphere height results in a smooth transition in the extinction coefficients to their extraterrestrial values at  $h_g = 50\text{ km}$  in 3.19. From these plots, it is clear that aerosols can play a significant role in penumbra SRP. In Fig. 4.10d, we compare penumbra SRP results from these different aerosol turbidity scenarios.

### 3.6.3 Molecular absorption

We model molecular absorption by the three gases that most significantly influence the total solar radiance transmitted: ozone ( $\text{O}_3$ ), carbon dioxide ( $\text{CO}_2$ ), and water ( $\text{H}_2\text{O}$ ). When

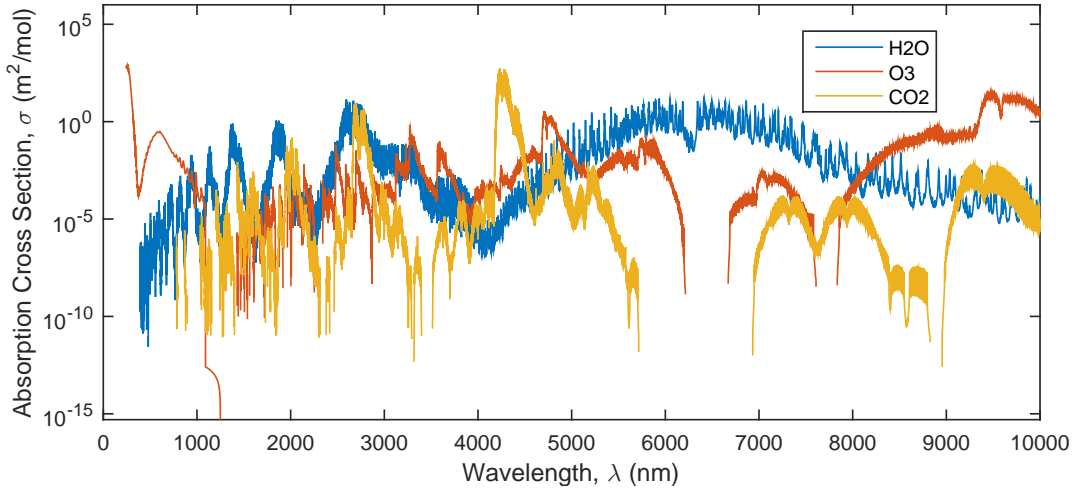


Figure 3.20: HITRAN absorption cross section spectra used in the SOLAARS model.

the wavelength of radiation excites a rotational or vibrational state in molecules in the atmosphere, energy from the radiation is lost to the molecules. For each constituent of the atmosphere, there are numerous excitation wavelengths that need to be considered. The HITRAN (High Resolution Transmission) molecular spectroscopic database (Rothman et al., 2013) is a continuously updated collection of spectral lines corresponding to molecular absorption and emission developed by the Air Force Cambridge Research Laboratories in the late 1960's. Pressure and temperature broadening effects lead to a spectral spread of absorption lines, which HITRAN can consider to provide precise absorption cross section ( $\sigma$ ) spectra (in  $\text{m}^2/\text{mol}$ ). These line broadening variations are not significant enough in the lower atmosphere to cross our relatively large ( $\Delta\lambda = 5 \text{ nm}$ ) spectral bins and influence results. Therefore, we use the same HITRAN absorption cross section spectra (see Fig. 3.20) from standard conditions (1 atm, 296 K) at all altitudes.

Altitude variations enter molecular absorption calculations through variations in the number density of absorbing molecules in the atmosphere. The number density of a particular molecule at a particular altitude is computed using the total number density and the unitless mixing ratio,  $M$ , of that molecule. The total number density ( $N$ ) is given by the selected atmosphere profile from COESA (1966), and the mixing ratios for  $\text{H}_2\text{O}$  and  $\text{O}_3$  are given as a function of altitude by Anderson et al. (1986). These mixing ratio profiles from Anderson et al. (1986) are shown in Fig. 3.21. Following Anderson et al. (1986), we assume uniform mixing of  $\text{CO}_2$  up to our atmosphere height of 50 km, however we assume a higher, more up-to-date figure for this constant mixing ratio from Picard et al. (2008) of  $M_c(h_s) = 0.0004$ . We integrate number density along the light ray path from Fig. 3.16 and multiply by the absorption cross section to give the half optical thickness:

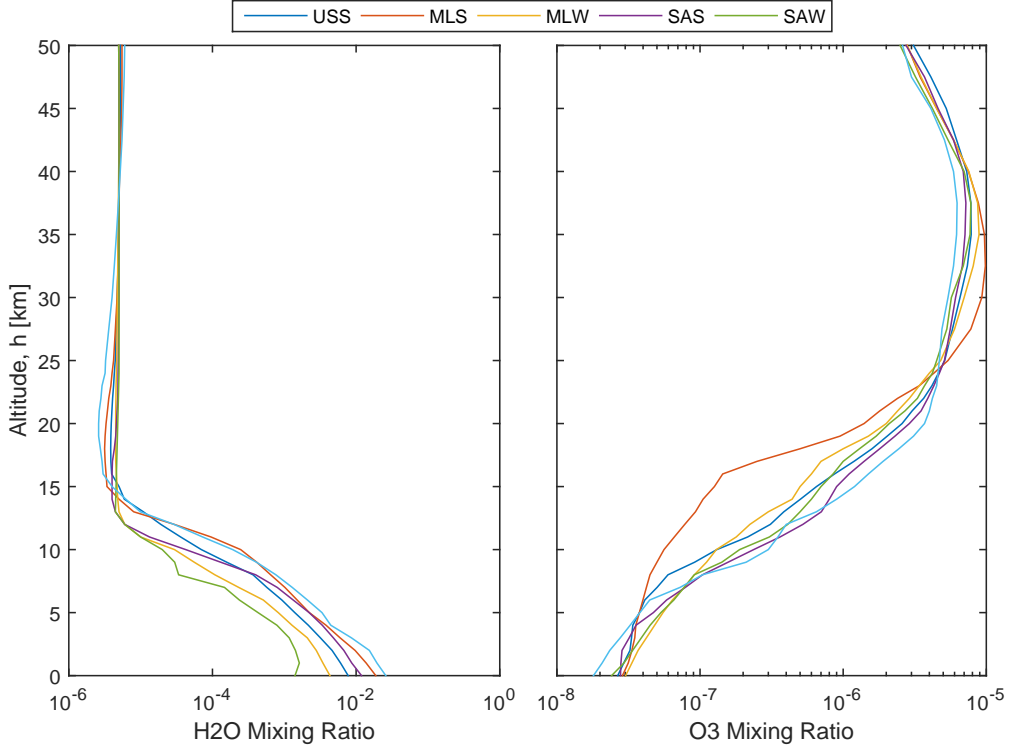


Figure 3.21: Mixing ratios profiles for the five standard atmospheres used in SOLAARS.

$$\tau_m(\lambda, h_g) = \sigma(\lambda) \int_0^{s_{max}} N(h_s) \mathbb{M}(h_s) ds \quad (3.76)$$

Once we compute the half optical thickness for each molecule, we can compute the individual transmittances using Eq. 3.66. We multiply these transmittances of each molecule to give the total transmittance for molecular absorption:

$$\mathbb{T}_m(\lambda, h_g) = \mathbb{T}_{m,o}(\lambda) \mathbb{T}_{m,w}(\lambda) \mathbb{T}_{m,c}(\lambda) \quad (3.77)$$

where the transmittance subscripts refer to the molecule being addressed (i.e. *o* for O<sub>3</sub>, *c* for CO<sub>2</sub>, and *w* for H<sub>2</sub>O). The mixing ratio variations shown in Fig. 3.21, translate to clear differences in tabulated radiance coefficient results. Fig. 3.22 shows extinction coefficient profiles for a two spectral bin extinction model (i.e.  $N_b = 2$ ) for each of the five standard atmospheres, with all other extinction modeling inputs held constant.

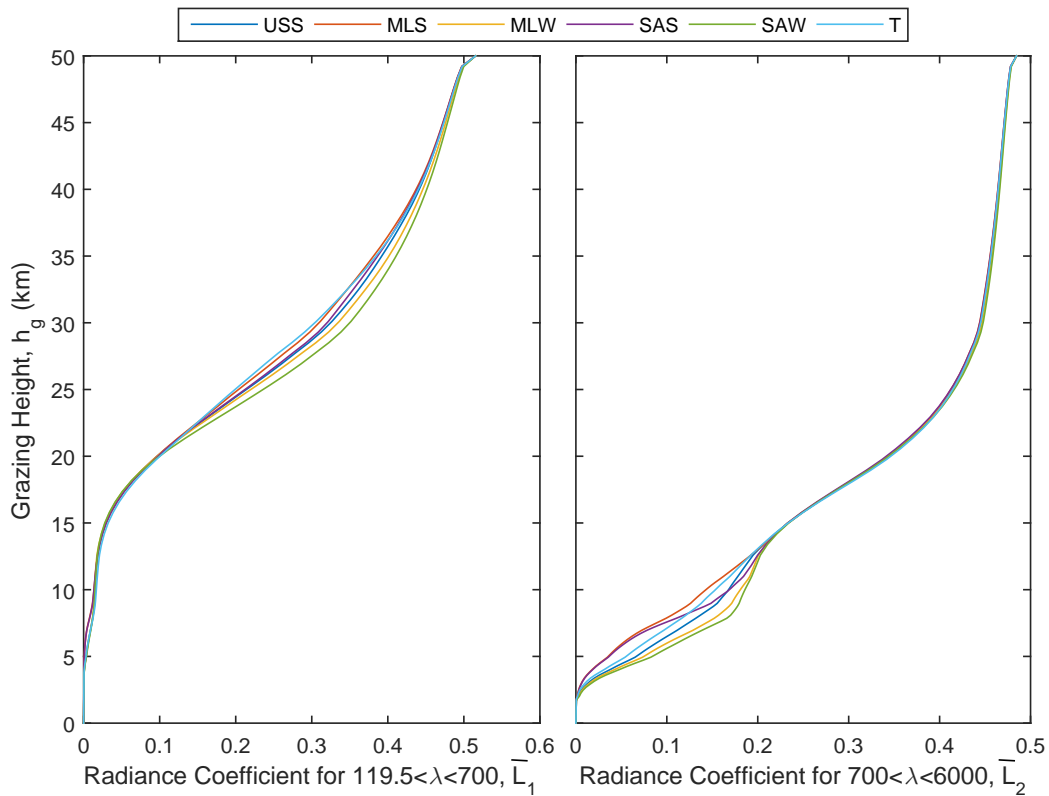


Figure 3.22: Extinction coefficient profiles for a two spectral bin model with a Visible/UV bin ( $\bar{L}_1$ ) and IR bin ( $\bar{L}_2$ ). Results are shown for each of the standard atmospheres used in the SOLAARS model.

### 3.6.4 Cloud extinction

Clouds are a highly unpredictable and significant variable in the optics of the atmosphere below 15 km. Clouds are optically thick relative to the rest of the atmosphere, and they are present over the majority of Earth at any moment in time. Wylie et al. (2005) presented data from 22 years of observations indicating 75% cloud coverage of Earth. Global satellite measurements in Lelli et al. (2011) show an average vertical column cloud optical depth of 19.1, which is very large (aerosol optical depth is usually less than 0.5). The grazing path of light rays significantly increases the likelihood of light rays striking clouds, and light rays passing below the cloud layer will pass through the layer twice on their way to penumbra. Due to this grazing geometry of light rays and the high optical thickness of clouds, we assume that light rays with grazing heights below the cloud top height,  $h_{CT}$ , are completely attenuated (i.e.  $\mathbb{T}_c = 0$ ). Light rays with grazing heights above the cloud top height are unaffected. So, in summary:

$$\mathbb{T}_c(\lambda, h_g) = \begin{cases} 0 & \text{if } h_g < h_{CT} \\ 1 & \text{if } h_g \geq h_{CT} \end{cases} \quad (3.78)$$

What remains is to input some cloud top height ( $h_{CT}$ ). Lelli et al. (2011) presents zonal averages of cloud top height from seven years of satellite observations (see Fig. 3.23). The data indicate significant zonal variations in cloud top height and frequency which are supported by other measurements (Rossow and Schiffer 1999; Sassen et al. 2008; Wylie et al. 2005). The zonal average values from Lelli et al. (2011) vary significantly with latitude from 4.02 km to 8.42 km and vary from 2.01 km to 12.21 km if we include one standard deviation from the mean. This relationship between light ray grazing point latitude and average cloud top height could be used to set this input to extinction parameter modeling; however, we simply use the limits of these zonal averages as boundaries over which to vary the cloud top height input. In Fig. 4.10b, we show the influence of this highly uncertain input by comparing penumbra SRP results from different cloud top height ( $h_{CT}$ ) values.

### 3.6.5 Extinction model validation

The SMARTS2 radiative transfer code described in Gueymard (2001) produces, among other data, direct beam SSI on Earth's surface as a function of various input variables describing the atmosphere and observer location. Our modeling does not include all of the effects considered by Gueymard (2001), namely molecular absorption by number of gases in the atmosphere. To verify our simpler modeling of atmospheric extinction, we run the SMARTS2 RTC and our extinction model under the same atmospheric conditions.

Both our model and the SMARTS2 model are used to calculate direct beam SSI for the Sun directly overhead (zero zenith angle). Fig. 3.24 shows the results of this comparison to the

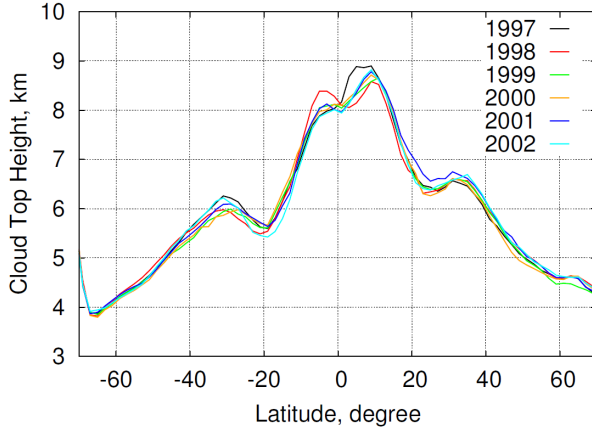


Figure 3.23: Zonal average cloud top heights from Lelli et al. (2011).

SMARTS2 RTC. The results of our modeling and SMARTS2 are smoothed to 50 nm resolution using a moving average, so that the difference between the two models can be clearly visualized regardless of a difference in spectral resolution of the two data sets. The agreement between the SMARTS2 results and our modeling is good, with a total wavelength integrated difference of less than 2%. Additionally, in Fig. 3.24 we show the extraterrestrial spectrum (ASTM E490) used as input to both models, and we show the results of our modeling if only Rayleigh scattering is considered, as Vokrouhlický et al. (1993) did. The significant difference between the "Rayleigh Only" and the "Full Modeling" curves is characterized by the lack of two features in the "Rayleigh Only" SSI curve: (1) a low magnitude broadband drop; and (2) higher magnitude localized drops. The broadband drop missing from the "Rayleigh Only" curve is caused by aerosol extinction, and the missing localized drops are caused by molecular absorption. These results demonstrate the precision of our extinction modeling and illustrate the significance of the previously ignored extinction processes.

### 3.7 SOLAARS-CF: A fast approximation to SOLAARS

The full SOLAARS model described so far in this chapter is very precise, however its potential for certain applications is limited because of its complexity and high computational cost. SOLAARS-CF, a simple curve fit based approximation to the full model, provides a physically representative shadow function for these applications.

To generate a simple, fast approximation to the full SOLAARS model, we convert the large solar radiation field data set (i.e. radiance, spectral composition, and direction of each light ray) generated at a given Sun-Earth-satellite geometry to a single, unitless (0-1) SRP attenuation factor ( $\alpha$ ). The SRP attenuation factor is the fraction of total solar radiance remaining at a given position, and is defined in the SOLAARS framework as:

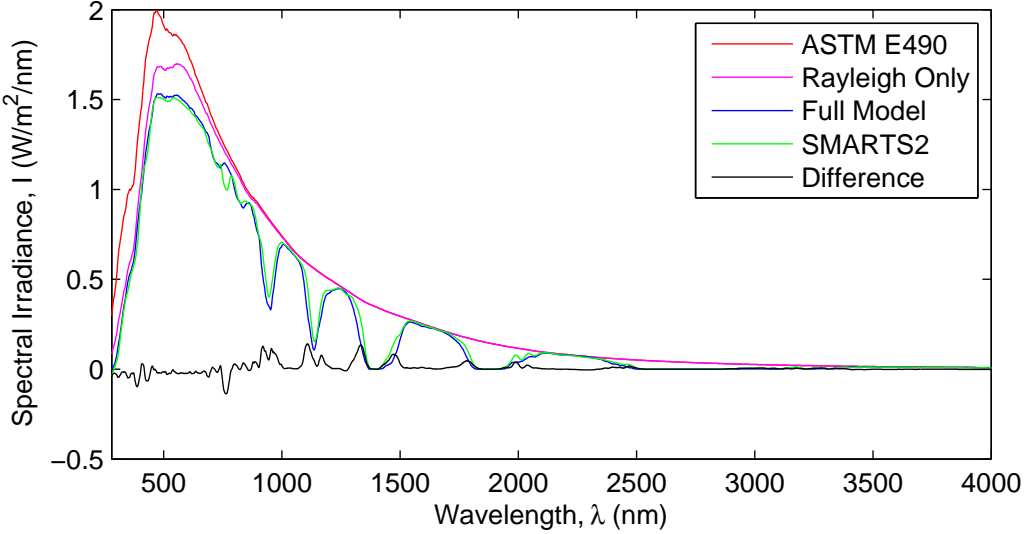


Figure 3.24: Comparison of SMARTS2 (Gueymard, 2001) and the results of our full modeling and modeling with only Rayleigh scattering for direct beam SSI. The extraterrestrial spectrum used from ASTM (2014) is shown as well. Note that these SSI spectra are smoothed to 50 nm resolution. The difference between the full SOLAARS model and SMARTS2 results is shown as well.

$$\alpha = \sum_{i=1}^{\mathbb{N}_r} (\bar{L}(h_{g,i}) \sin(\theta_i) \Delta\theta_i \Delta\phi_i) \quad (3.79)$$

where a single spectral bin is used (i.e.  $\mathbb{N}_b = 1$ ), eliminating the spectral bin summation. When multiplied by the results of any SRP modeling that ignores the presence of Earth, this SRP attenuation factor can be used to account for Earth eclipses and penumbra transition SRP behavior.

The goal of the SOLAARS-CF model is to provide a simple, accurate shadow function which describes the behavior of  $\alpha$  as a function of Sun-Earth-satellite geometry. Development of the SOLAARS-CF shadow function includes the following steps:

1. Define geometric parameters which drive penumbra SRP
2. Generate SRP attenuation factor ( $\alpha$ ) data using SOLAARS
3. Define the SOLAARS-CF shadow function by curve fitting attenuation factor data to geometric parameters

Sect. 3.7.1 describes the geometry used to parameterize penumbra SRP and presents the SOLAARS attenuation factor ( $\alpha$ ) data to be curve fitted. Sect. 3.7.2 describes the process

of curve fitting to SOLAARS SRP attenuation factor data. Finally, Sect. 3.7.3 outlines the software implementation of the SOLAARS-CF model.

### 3.7.1 Geometric parameters and SOLAARS data

To produce a relatively simple shadow function, a number of variables in the full SOLAARS model must be fixed. The following assumptions are made to simplify the problem:

1. USS atmosphere density and mixing ratio profiles
2. Medium aerosol extinction coefficient profile (see Table 3.1)
3. Cloud top height ( $h_{CT}$ ) of 5892.5 m, the mean of zonal averages from Lelli et al. (2011)
4. Constant satellite optical properties as a function of wavelength
5. Axial tilt of Earth with respect to the ecliptic is negligible in oblateness modeling

Assumptions 1-3 are selecting the average atmospheric conditions for a global model. Assumption 4 results from the use of only one spectral bin in Eq. 3.7. It would be possible to repeat the process we carry out here for multiple spectral bins, creating a separate shadow function for each one; however, in the interest of simplicity and ease of implementation, we create a single shadow function for all solar flux. Finally, Assumption 5 greatly simplifies our treatment of Earth oblateness.

The geometry involved in the SOLAARS-CF shadow function is based on satellite position relative to the Sun, Earth, and ecliptic as illustrated in Fig. 3.25. For a spherical Earth, SRP is primarily driven by the two distances  $r_R$  and  $r_E$ . The distance along the Sun-Earth direction is defined as:

$$r_R = -\vec{r} \cdot \hat{R} \quad (3.80)$$

Since we assume zero axial tilt of Earth, polar flattening occurs only in the ecliptic direction ( $\hat{E}$ ). This simplification allows us to generate a SOLAARS curve fit of the form  $\alpha(r_R, r_E)$  for a spherical Earth, and compensate for Earth oblateness by scaling the  $r_E$  component before evaluating the curve fit. To properly scale the distance  $r_E$  and compensate for oblateness, we need to separate its vector into the components perpendicular to the ecliptic ( $r_{E\perp}$ ) and parallel to the ecliptic ( $r_{E\parallel}$ ). The geometry in Fig. 3.25 gives the following:

$$\vec{r}_E = \vec{r} - (\vec{r} \cdot \hat{R})\hat{R} \quad (3.81)$$

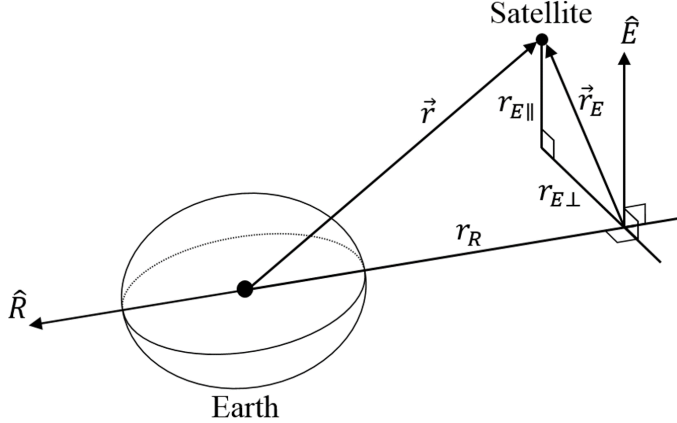


Figure 3.25: SOLAARS-CF geometric parameters.  $\hat{R}$  is the geocentric unit vector pointing to the Sun and  $\hat{E}$  is the unit normal to the ecliptic. The satellite position vector  $\vec{r}$  is described in the curve fit SOLAARS approximation by its projection along the  $\hat{R}$  direction ( $r_R$ ) and its remaining components in  $\vec{r}_E$ . The component of  $\vec{r}_E$  perpendicular to the ecliptic is  $r_{E\perp}$  and the component parallel to the ecliptic is  $r_{E\parallel}$ , which is scaled to compensate for Earth oblateness.

$$r_{E\parallel} = \hat{E} \cdot \vec{r}_E \quad (3.82)$$

$$r_{E\perp} = \sqrt{r_E^2 - r_{E\parallel}^2} \quad (3.83)$$

When generating attenuation factor ( $\alpha$ ) data for curve fitting, we override the precise oblateness modeling described in Section 3.1 and use a constant equatorial Earth radius for curve fitting. This results in an attenuation factor dataset which is circularly symmetric about  $\hat{R}$ . Fig. 3.26a illustrates this circular symmetry of the penumbra SRP attenuation factors from SOLAARS when oblateness is ignored. Fig. 3.26b shows that when polar flattening in the ecliptic is considered, the attenuation factor data is simply compressed in the ecliptic direction by the oblateness scaling factor:

$$s_O = \frac{R_{\oplus,e}}{R_{\oplus,p}} \quad (3.84)$$

where  $R_{\oplus,e}$  and  $R_{\oplus,p}$  are the equatorial and polar Earth radii, respectively. Note that the scaling factor used in Fig. 3.26 is exaggerated significantly to illustrate its effect. With this scaling factor, we can scale  $r_{E\parallel}$  to adjust the distance  $r_E$  and compensate for oblateness before applying our  $\alpha(r_R, r_E)$  curve fit:

$$r'_E = \sqrt{r_{E\perp}^2 + (s_O r_{E\parallel})^2} \quad (3.85)$$

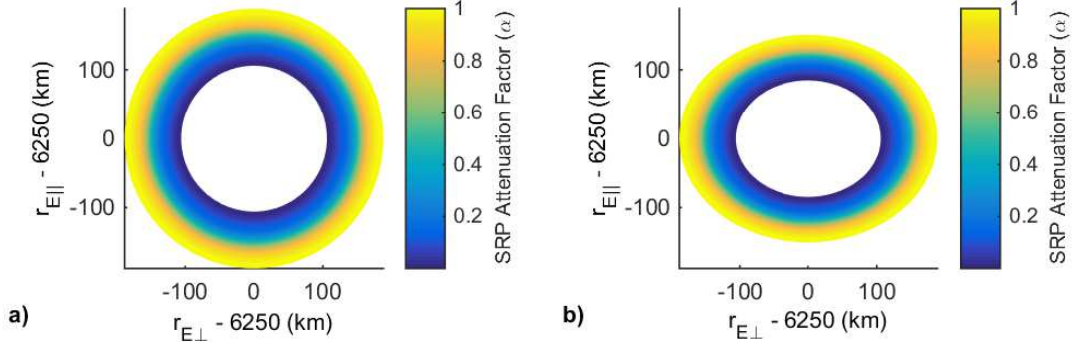


Figure 3.26: A constant slice of SOLAARS results for locations in a constant  $r_R$  plane without Earth oblateness correction (a) and with the correction for flattening in the ecliptic (b).

This adjusted distance ( $r'_E$ ) makes the transition from Fig. 3.26b to the corresponding point in Fig. 3.26a.

Since we can simply adjust  $r_E$  to deal with oblateness, it is only necessary to curve fit SOLAARS as a function of the two distances  $r_R$  and  $r_E$ . To cover orbits from LEO to GEO,  $r_R$  is varied from 2000 km to 45000 km at 70 evenly spaced values. At each value of  $r_R$ , SOLAARS is used to compute SRP attenuation factors ( $\alpha$ ) at 70 values of  $r_E$  evenly distributed over the penumbra region. The data from SOLAARS, which we need to match with a curve fit is shown in Fig. 3.27

### 3.7.2 Curve fitting

Like Hubaux et al. (2012), we use the hyperbolic tangent sigmoid function to model penumbra SRP behavior and fit the surface in Fig. 3.27. This three dimensional curve fitting is a two step process. First, for each constant  $r_R$  slice of the data in Fig. 3.27, we fit the following function, which is a summation of three hyperbolic tangent sigmoids shifted and scaled by the fit coefficients ( $a_1-a_8$ ):

$$\alpha = \frac{1 + a_1 + a_2 + a_1 \tanh(a_3(r'_E - a_4)) + a_2 \tanh(a_5(r'_E - a_6)) + \tanh(a_7(r'_E - a_8))}{2 + 2a_1 + 2a_2} \quad (3.86)$$

Note that this curve fit is evaluated with the adjusted distance  $r'_E$  in units of  $10^6$  meters. The summation of three sigmoids allows us to more precisely capture the complex behavior of penumbra SRP. Using the trust-region-reflective curve fitting algorithm in MATLAB, we generate a unique set of  $a$  coefficients at each of the 70  $r_R$  values in the SOLAARS dataset. Fig. 3.28 illustrates the quality of this three-sigmoid fit, showing each of the three sigmoids,

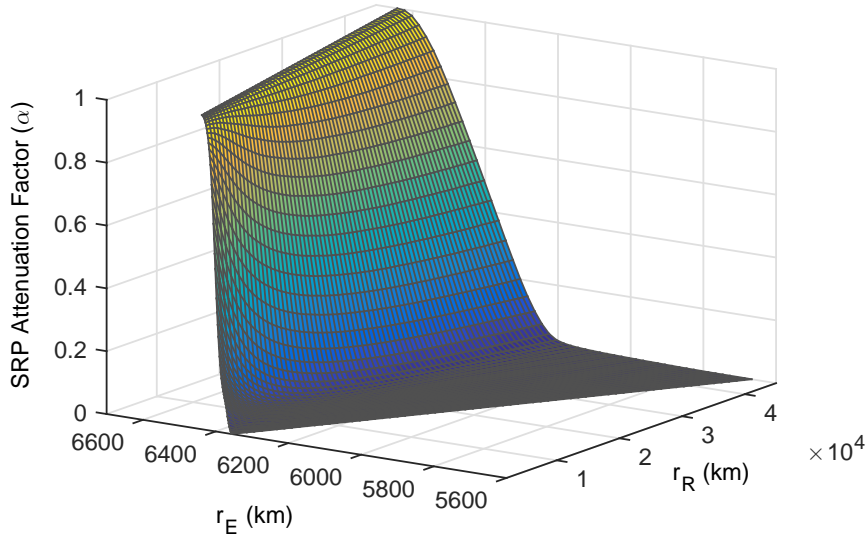


Figure 3.27: SOLAARS attenuation factor data which is the basis of the SOLAARS-CF curve fit.

total SOLAARS-CF curve, and SOLAARS dataset slice being fit to. In the second step of curve fitting, a global (i.e.  $r_R$  and  $r_E$ ) dependent curve fit of the SRP attenuation factor is developed by fitting each of these  $a$  coefficients as a function of  $r_R$ .

Each of the eight  $a$  coefficients, computed by curve fitting to  $r_R$  slices of SOLAARS data, behaves differently as a function of  $r_R$  and requires a unique curve fit. These  $a$  coefficient curve fit formulas, and the  $b$  coefficients which drive them, are given in Table 3.2. The behavior of raw  $a$  coefficient data and of the tabulated curve fits are shown in Fig. 3.29. The scaling coefficient for sigmoid 2 ( $a_2$ ) is the most challenging to accurately fit, and so we anticipate the most significant errors will occur in the full sunlight ( $\alpha \approx 1$ ) region. The final curve fitting results, shown in Fig. 3.30, confirm that the most significant errors occur near full sunlight and demonstrate the accuracy of SOLAARS-CF curve fitting with maximum residuals  $< 3\%$ .

### 3.7.3 Implementation

Software implementation of the SOLAARS-CF model is described in Fig. 3.31. First, the components of the satellite position vector  $r_R$  and  $r_E$  are computed, and  $r_E$  is adjusted for Earth oblateness. These position vector components are then used to evaluate the SOLAARS curve fit and give the SRP attenuation factor ( $\alpha$ ). SRP accelerations can be modeled without

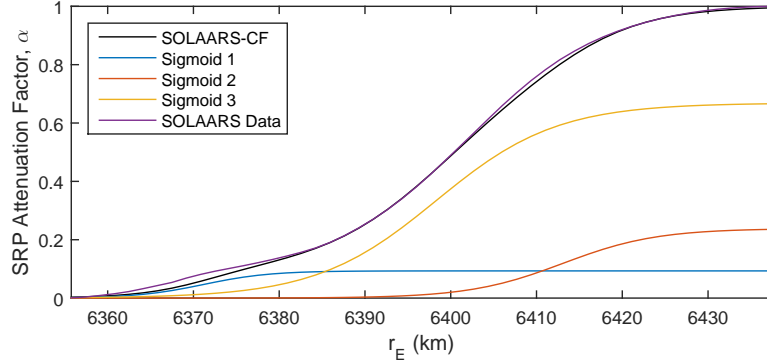


Figure 3.28: Comparison of SOLAARS-CF curve fit and SOLAARS SRP attenuation factor data being fit to in the  $r_R=2000$  km slice. The three sigmoids, which correspond to the three hyperbolic tangent terms in Eq. 3.7.2, compose the SOLAARS-CF curve.

Table 3.2: Curve fitting formulas for computing the  $a$  coefficients which capture  $r_R$  dependence of penumbra SRP. Note that these curve fitting formulas are evaluated with the distance  $r_R$  in units of  $10^6$  meters.

Formula	$b_1$	$b_2$	$b_3$	$b_4$
$a_1 = b_1 e^{b_2 r_R} + b_3 e^{b_4 r_R}$	0.1715	-0.1423	0.01061	-0.01443
$a_2 = b_1 r_R + b_2$	0.008162	0.3401	-	-
$a_3 = b_1 e^{b_2 r_R} + b_3 e^{b_4 r_R}$	260.9	-0.4661	27.81	-0.009437
$a_4 = b_1 r_R^{b_2} + b_3$	-0.006119	1.176	6.385	-
$a_5 = b_1 e^{b_2 r_R} + b_3 e^{b_4 r_R}$	87.56	-0.09188	19.30	-0.01089
$a_6 = b_1 r_R + b_2$	0.002047	6.409	-	-
$a_7 = b_1 e^{b_2 r_R} + b_3 e^{b_4 r_R}$	61.98	-0.1629	27.87	-0.02217
$a_8 = b_1 e^{b_2 r_R} + b_3 e^{b_4 r_R}$	6.413	-0.0002593	-0.01479	-0.1318

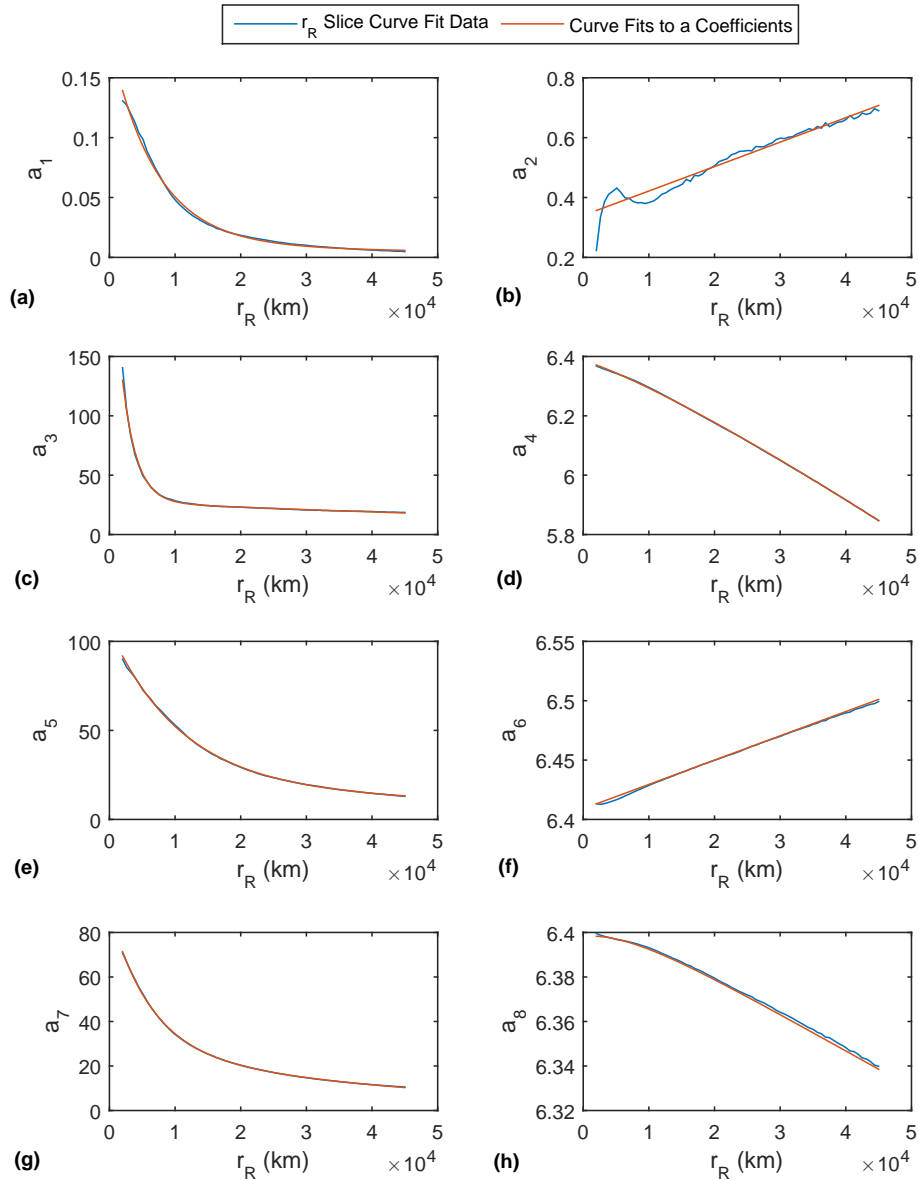


Figure 3.29: Curve fitting results for  $a$  coefficients in each constant  $r_R$  slice of the SOLAARS data and associated curve fits to the  $a$  coefficients as a function of the  $r_R$  distance.

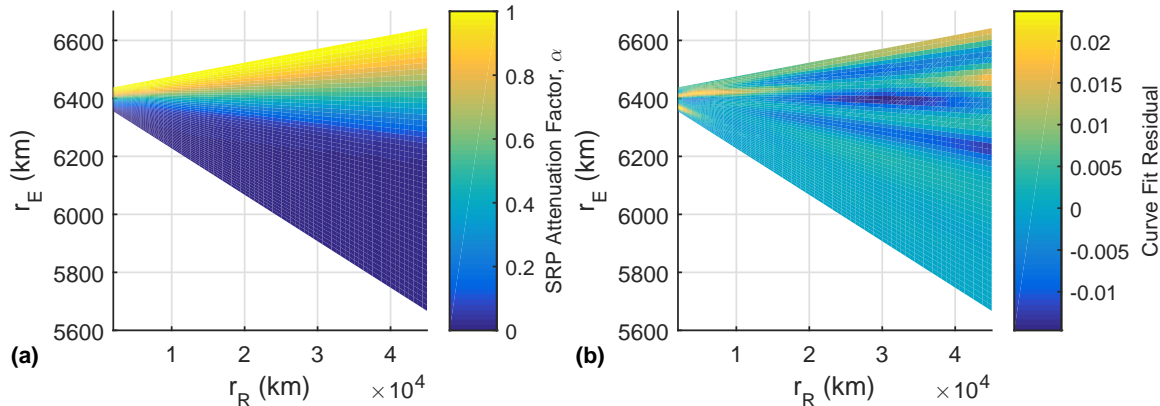


Figure 3.30: SOLAARS results which are the basis for curve fitting (a) and curve fitting residuals (b).

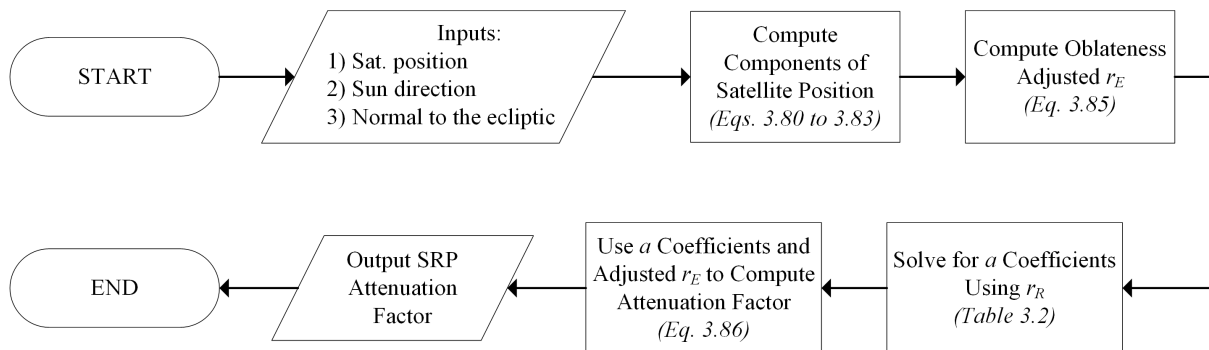


Figure 3.31: Flowchart for SOLAARS-CF software implementation.

considering the presence of Earth, and multiplied by this SOLAARS-CF attenuation factor to account for Earth eclipses and penumbra SRP behavior.

# Chapter 4

## Results and Analysis

### 4.1 Application to the GRACE satellites

The GRACE satellite mission is a joint effort by NASA and the German Aerospace Center (DLR). The primary goal of the mission, as described in Tapley et al. (2004), is to measure anomalies in Earth's gravity field. The two twin GRACE satellites (denoted GRACE A and GRACE B), shown in Fig. 4.1, fly in polar, low Earth orbit (LEO) separated along the orbital path by a distance of approximately 220 km.

Measurement of gravity field anomalies is accomplished by continuous measurements of the distance between the two satellites, as illustrated in Fig. 4.2. Gravity anomalies influence the relative motion of the satellites, which are observed using a highly accurate K-band ranging system. Non-gravitational forces influence the relative motion of the satellites as well, so each GRACE satellite has a high accuracy accelerometer to remove the influence of non-gravitational forces from inter-satellite ranging data.

For the orbit of the GRACE satellites - retrograde with a nodal precession of -50 degrees/year, 89 degrees inclination, near circular, decaying from 500 km in March, 2002 to 460 km in 2011 - seasons with eclipse conditions have a duration of about 120 days alternating with full-sun periods of about 40 days. This means that for 75% of the mission we can observe two penumbra transitions per revolution, or about 30 per day. Fig. 4.3 shows a map of SOLAARS-CF shadow function data computed over the entire year of 2008 for GRACE A. For some days before and after the full-sun period, the transition time periods are elongated due to the glancing intersection of the orbit with the terminator of the Earth shadow.

The GRACE accelerometers have provided excellent time series for many years now. A very low sensor noise level at high frequencies has been verified (Flury et al., 2008), and the



Figure 4.1: A photo of the GRACE satellites during integration from Doornbos (2012).

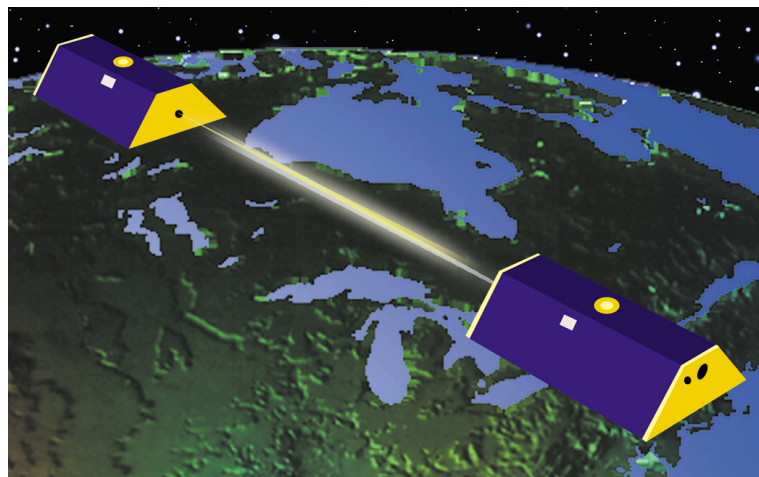


Figure 4.2: Illustration of the GRACE satellites in orbit from <http://www.csr.utexas.edu/grace>.

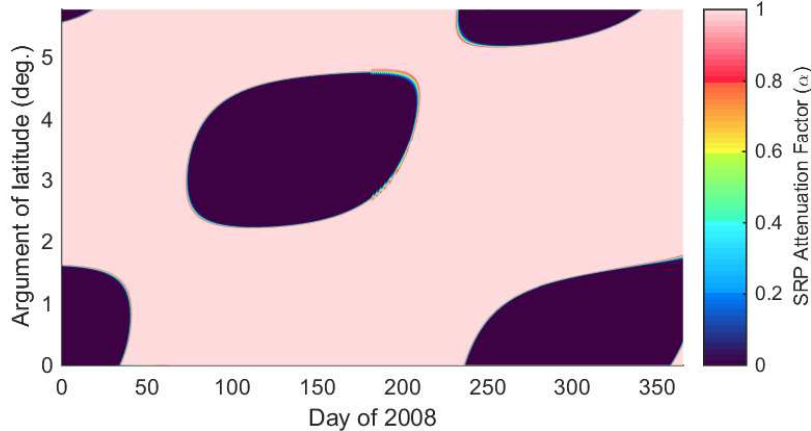


Figure 4.3: GRACE A shadow function map for GRACE A for 2008 generated using SOLAARS-CF.

acceleration change during penumbra transitions is much larger than the accelerometer noise level. This makes the transitions stand out as very distinct features in the accelerometer time series, giving us a unique opportunity to validate our penumbra SRP models.

#### 4.1.1 Testing SOLAARS-CF oblateness with GRACE data

GRACE A acclerometer data is used to test the simplified oblateness modeling in SOLAARS-CF, which ignores the axial tilt of Earth with the ecliptic. 78 clean penumbra transition accelerometer signals are selected from a 140 day span of ACC1B acclerometer data between January 20, 2008 and June 8, 2008. The SOLAARS-CF model is applied over each of these penumbra time periods with and without considering Earth oblateness. The spherical Earth SOLAARS-CF model does not apply the oblateness correction to the distance  $r_E$  and uses the WGS84 mean Earth radius as the radius of the spherical Earth (NIMA, 2000). Accelerometer signals are scaled and biased so that they change between 0 and 1 over the penumbra time period and can be treated as SRP attenuation factors for comparison with SOLAARS-CF results. Fig. 4.4 shows one of these SRP attenuation factor comparisons.

An SRP attenuation factor of  $\alpha = 0.5$  is used to select a penumbra center time for each transition in each SRP attenuation factor curve. Penumbra timing error is defined as the difference between the penumbra center time computed from modeling results and the center time derived from accelerometer data. Penumbra timing error results, shown in Fig. 4.5, illustrate the significant improvement in penumbra timing achieved with the simplified SOLAARS-CF oblateness model. Using the oblate Earth model reduced average timing error relative to the accelerometry based results from 8.08s to 1.83s, which is a greater than 77% improvement.

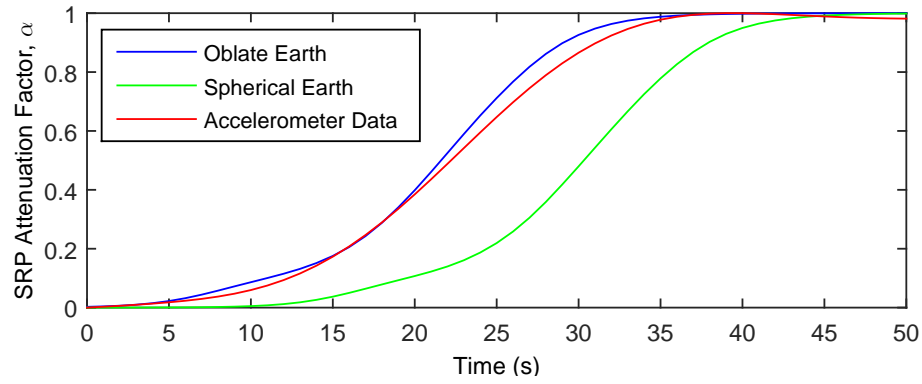


Figure 4.4: Comparison of GRACE A attenuation factors derived from accelerometer data and from the SOLAARS-CF model with and without Earth oblateness.

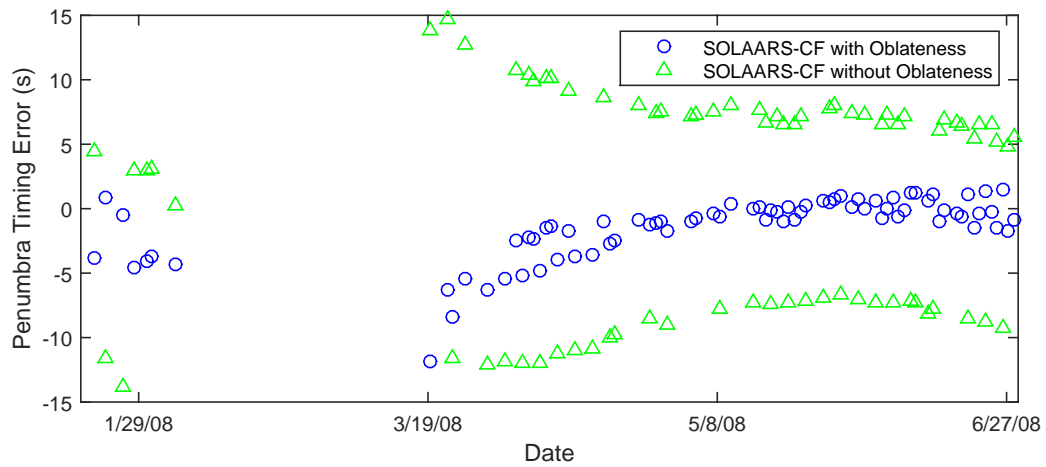


Figure 4.5: Comparison of penumbra timing error results with and without Earth oblateness in SOLAARS-CF.

### 4.1.2 Applying SOLAARS to GRACE

In this section, we describe how the full SOLAARS model is applied to the twin GRACE satellites. This is important both as documentation of our validation experiment and as an example of how SOLAARS is applied to a specific problem. We have formulated the model to be adaptable to a variety of applications, primarily through the selection of optics function ( $\vec{O}$ ) and number of spectral bins ( $N_b$ ).

For GRACE, we model the spacecraft geometry in the optics function ( $\vec{O}$ ), using eight flat panels described in the GRACE product specification document (Bettadpur, 2007). We do not consider the GRACE boom because it is not a flat panel like the other surfaces, and we find that including it in SRP acceleration calculations does not significantly influence the results. The product specification document provides the following for each surface panel, where the index  $k$  identifies the panel:

1. Area ( $A_k$ )
2. Specular reflectivity for visible light ( $v_{k,1}$ ) and IR light ( $v_{k,2}$ )
3. Diffuse reflectivity for visible light ( $\kappa_{k,1}$ ) and IR light ( $\kappa_{k,2}$ )
4. Direction unit normal vector ( $N_k$ )

Since we have GRACE surface reflectivities for two spectral bins, we use  $N_b = 2$  in Eq. 3.32 (hence the indices 1 and 2 for reflectivities in the list above). We split the solar spectrum at the visible/IR boundary (700 nm). Hence, the  $j = 1$  spectral bin has boundaries of  $\lambda_1^- = 119.5\text{nm}$  and  $\lambda_1^+ = 700\text{nm}$ , and the  $j = 2$  spectral bin has boundaries of  $\lambda_2^- = 700\text{nm}$  and  $\lambda_2^+ = 6000\text{nm}$ . These boundaries are used to produce radiance coefficient tables for each spectral bin ( $\bar{L}_1$  and  $\bar{L}_2$ ) using Eq. 3.65.

Our definition of the optics function ( $\vec{O}$ ) for this GRACE investigation assumes that the influence of one light ray is the sum of three components: (1) an absorbed portion of the incident ray; (2) a specularly reflected ray; and (3) a Lambertian diffusely reflected field of rays. Since our approximation for the GRACE geometry is composed of flat panels, our  $\vec{O}$  function is a summation over the eight panels:

$$\vec{O}_j(\hat{n}_i) = \sum_{k=1}^8 A_k \Psi(\hat{n}_i, \hat{N}_k) [\hat{n}_i - v_{k,j} (\hat{n}_i + 2\Psi(\hat{n}_i, \hat{N}_k) \hat{N}_k) - \kappa_{k,j} \frac{2}{3} \hat{N}_k] \quad (4.1)$$

where  $\Psi$  is the surface panel shadow function. This  $\Psi$  function is zero when the surface is in shadow from the light ray and is the cosine of the angle between the incident light ray direction ( $\hat{n}$ ) and the normal to the satellite surface panel ( $\hat{N}$ ) when the ray is incident on the outer panel surface:

$$\Psi(\hat{n}, \hat{N}) = \begin{cases} 0 & \text{if } \hat{n} \bullet \hat{N} \geq 0 \\ -\hat{n} \bullet \hat{N} & \text{if } \hat{n} \bullet \hat{N} < 0 \end{cases} \quad (4.2)$$

In order to use each panel direction ( $\hat{N}$ ) from (Bettadpur, 2007) in Eq. 4.1, we have to rotate it from the satellite reference frame ( $\{s\}$ ) to the Earth pointing reference frame ( $\{e\}$ ) of Eq. 3.32. The satellite reference frame axes approximately point in along track (towards the twin satellite), cross track, and radial (nadir pointing) directions (Bettadpur, 2007). We define this transformation in two rotations. For the first rotation, we use GRACE SCA1B attitude quaternions obtained from star camera observations to describe a rotation from the satellite reference frame to an Earth centered inertial reference frame ( $\{i\}$ ). We interpolate GRACE attitude quaternions using spherical linear interpolation (Shoemake, 1985) from 5 s to 1 s time steps. This way, modeling produces results at the same sampling rate as the GRACE ACC1B accelerometer data. Using these quaternions at each satellite position, we compute the rotation matrix  $\mathbf{R}^{s \rightarrow i}$ , which rotates each panel direction vector to the Earth centered inertial frame. For the second rotation, we use the satellite position ( $\vec{r}$ ) and Sun position ( $\vec{R}$ ) in the Earth centered inertial frame to define a rotation from this frame to the Earth pointing frame:

$$\hat{z} = -\frac{\vec{r}}{\|\vec{r}\|} \quad \hat{y} = \frac{\vec{R} \times \vec{r}}{\|\vec{R} \times \vec{r}\|} \quad \hat{x} = \hat{y} \times \hat{z}$$

$$\mathbf{R}^{i \rightarrow e} = \begin{bmatrix} \hat{x}^\top \\ \hat{y}^\top \\ \hat{z}^\top \end{bmatrix} \quad (4.3)$$

The two rotation matrices ( $\mathbf{R}^{i \rightarrow e}$  and  $\mathbf{R}^{s \rightarrow i}$ ) are combined to yield the final rotation matrix for transformation from the GRACE satellite reference frame to the Earth pointing reference frame where SRP calculations are carried out:

$$\mathbf{R}^{s \rightarrow e} = \mathbf{R}^{i \rightarrow e} \mathbf{R}^{s \rightarrow i} \quad (4.4)$$

### 4.1.3 SOLAARS solar radiation fields

By dividing the solar radiation field into light rays and computing each one's intensity and spectral composition, we essentially generate a series of images of the Sun from the satellite's perspective. Visualizing these solar radiation fields clearly demonstrates the significance of atmospheric refraction and extinction for a satellite in penumbra.

The modeled solar radiation fields illustrated in Fig. 4.6 show the evolution of solar radiation fields incident on GRACE A during an umbra entry transition on May 15, 2008. Each

window in these plots describes the solar radiation field at a different time in the penumbra transition. Fig. 4.6a illustrates the changes in radiance associated with the light rays in each solar radiation field, which is the sum of the radiance coefficients from all spectral bins (i.e.  $\sum_{j=1}^{N_b} \bar{L}_j$ ). Fig. 4.6b illustrates the changes in mean wavelength, which is the radiance weighted spectral bin center-wavelength (i.e.  $\frac{1}{N_b} \sum_{j=1}^{N_b} \bar{L}_j \lambda_j$ ). In generating Fig. 4.6b, we use the full set of spectral bins possible, with 5 nm bin widths ( $\lambda_j^+ - \lambda_j^-$ ) used in numerical evaluation of Eq. 3.65. We use this high spectral resolution to show the very detailed description of the solar radiation fields possible in our model. Note that this is much greater resolution than we actually use for GRACE SRP modeling. As described in Sect. 2.5, we only use the two large spectral bins for which we have optical properties. The top of our model atmosphere at a height of 50 km and solid Earth boundaries are marked in the window for each solar radiation field.

In Fig. 4.6, each solar radiation field is symmetric about  $\phi = 0$ , and, due to the assumption of a spherically symmetric atmosphere, this  $\phi$  width is nearly constant throughout the transition. Conversely, atmospheric refraction leads to significant compression and asymmetry of the solar radiation field in  $\theta$ . We should note that this compression of the field represents one of the major attenuation processes influencing penumbra SRP. One might assume that this compression represents focusing of the sunlight and an increase in the angular density of its optical power. In fact, this reduction in the angular size of the solar radiation field accounts for optical divergence in the atmosphere, as described by Vokrouhlický et al. (1993). The oblong, refracted shapes match those shown in Vokrouhlický et al. (1993) and in the photographic observations presented in Cameron et al. (1963).

In Fig. 4.6a, the radial variations in radiance are the result of solar limb darkening. As the Sun sets to the center of the atmosphere at about 15 s (see elapsed time above each frame), the radiance at the center of the solar radiation field has dropped to about 60% of the full sunlight value. At this point in the transition, changes in the spectral composition (shown in Fig. 4.6b) become clear. As the Sun sets, the wavelength dependence of atmospheric extinction processes result in progressively greater mean wavelengths. The mean wavelength at 25 s is about 400 nm greater than the full sunlight value. This change in spectral composition corresponds to changes in the sunlight-satellite interactions, i.e. the amount of incident light that is reflected or absorbed. At 35 s and 40 s, spectral changes increase significantly, however optical divergence (seen in small angular size of the radiation fields) and atmospheric extinction (in Fig. 4.6a) have already reduced the SRP to near zero. We are used to observing sunsets and sunrises here on Earth, and these illustrations showing essentially the same event (amplified by a longer atmospheric path) from the perspective of a satellite in penumbra is compelling. The significance of the atmosphere, which is generally ignored in computing penumbra SRP, is clear.

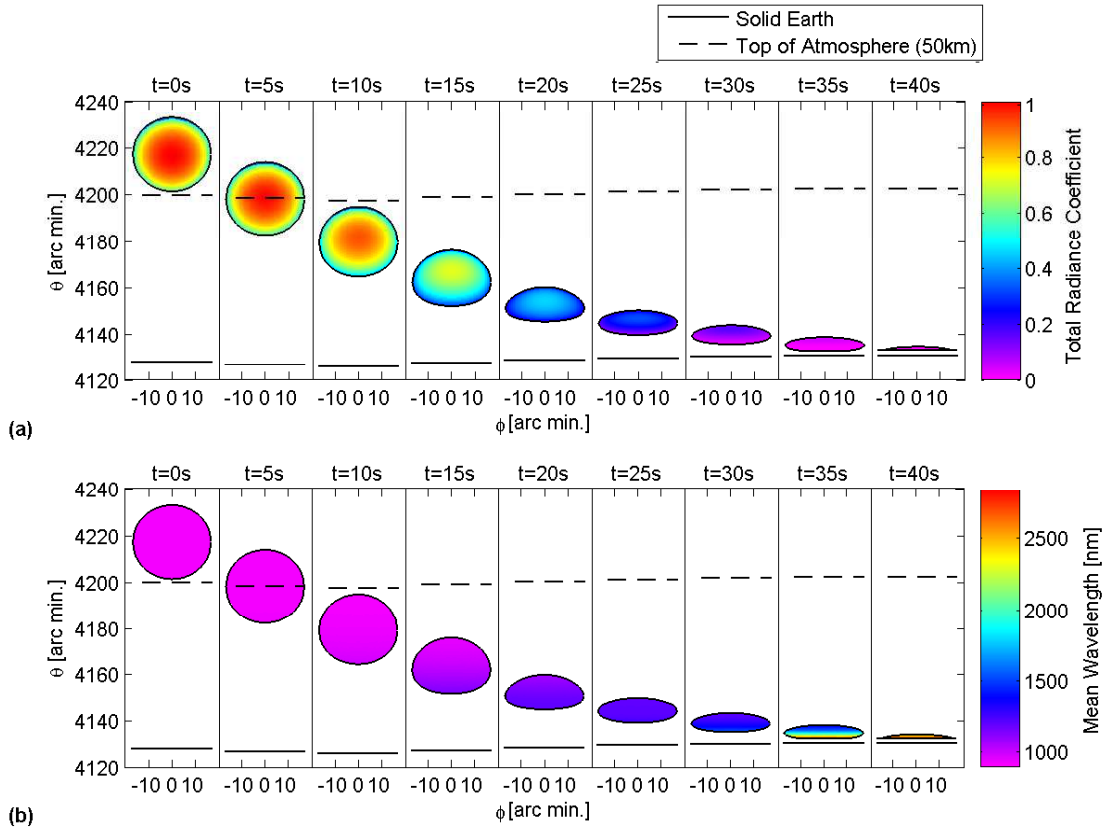


Figure 4.6: A SOLAARS solar radiation field dataset for a GRACE prenumbra transition. Each frame in these plots is titled with the elapsed time in the penumbra transition. These results were generated using the “low aerosol” profile from Table 3.1 and a cloudless (i.e.  $h_{CT} = 0$ ) USS atmosphere. Results are separated into two plots, where (a) shows radiance and (b) shows the spectral composition of the solar radiation fields.

#### 4.1.4 Two typical GRACE penumbra transitions

We start with two typical examples of how the observed non-gravitational accelerations change during a penumbra transition of a GRACE satellite. One set of modeled and observed accelerations is shown Fig. 4.7 and another, for a longer penumbra transition, is shown in Fig. 4.8. These figures show observed and modeled accelerations in the three axes of the satellite reference frame fixed to the spacecraft body for a time span including the penumbra transition itself with some margin before and after. We show 35 mHz low-pass filtered accelerometer observations (ACC1B data, 1 seconds sampling rate) before and after proper scaling (see Sect. 4.1.6). In addition to the results of our SOLAARS and SOLAARS-CF models, the results from the model of Montenbruck and Gill (2000) which does not consider atmospheric effects are shown.

The acceleration change is very prominent in all three directions in both modeling results and observations. According to the SOLAARS modeling results, the total length of the shorter penumbra transition in Fig. 4.8 between umbra (at 21 seconds) and full-sun (at 83 seconds) is 62 seconds. The total length of the longer penumbra transition in Fig. 4.8 between umbra (at 25 seconds) and full-sun (at 130 seconds) is 105 seconds. The total acceleration change during this time span for both transitions is about  $34 \text{ nm/s}^2$ .

Generally, results confirm the quality of both the accelerometer instrument and our SRP models. The agreement of the M&G 2000 results with accelerometer data is considerably worse. In both the results of the SOLAARS model and in the observed accelerations, the center of the penumbra transition (when the SRP drops to 50% of its initial magnitude) occurs about 14 seconds after it is expected by the M&G 2000 model for the transition shown in Fig. 4.8. Due to the partial transparency of the atmosphere and refraction of light around Earth, the actual penumbra transitions last more than three times longer than predicted by the M&G 2000 model. The SOLAARS-CF results for the shorter penumbra transition track closely with the results of the full SOLAARS model, however there is significant timing disagreement in the longer transition shown in Fig. 4.8. This indicates that the assumption of zero axial tilt with the ecliptic in the simpler SOLAARS-CF oblateness model can result in increased penumbra timing errors compared to the more rigorous SOLAARS oblateness model.

The M&G 2000 model produces symmetric transition curves, when the actual behavior is asymmetric with a characteristic tail on the umbra ends of the acceleration curves. This tail was described by Vokrouhlický et al. (1993), and results from high levels of atmospheric refraction in the lower atmosphere. In the penumbra tail, sunlight is traveling through lower altitudes in the atmosphere. At these altitudes, large refraction angles cause the SRP to persist; However, at these low grazing heights, SRP is low due to high levels of extinction and beam divergence. The error in the M&G 2000 model for shadow entry will often counteract the error of the following shadow exit. This is one reason why the M&G 2000 model nevertheless can work well for precise orbit determination. Integration errors are further reduced by symmetry of subsequent penumbra transitions (Vokrouhlický et al.,

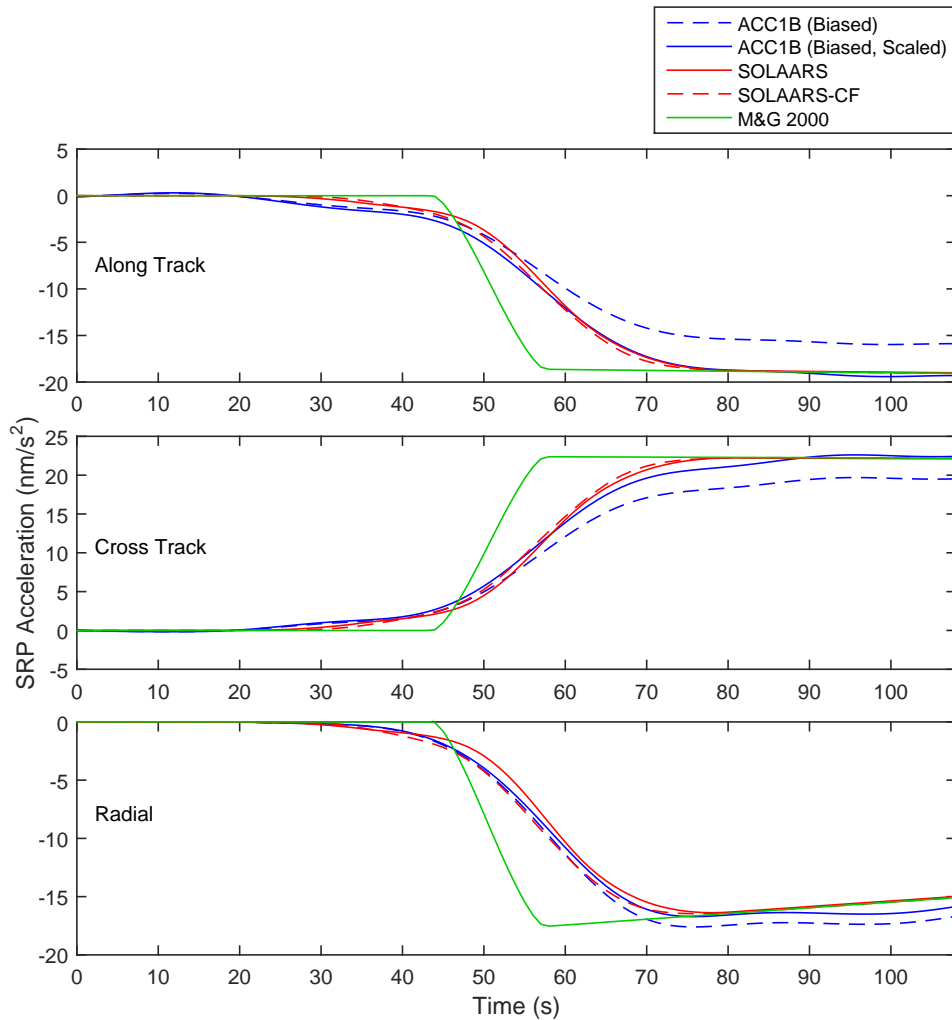


Figure 4.7: Typical example of a shadow exit of GRACE Satellite A on January 22, 2008. Accelerometer data and SRP modeling results from SOLAARS, SOLAARS-CF, and the model from Montenbruck and Gill (2000) are shown.

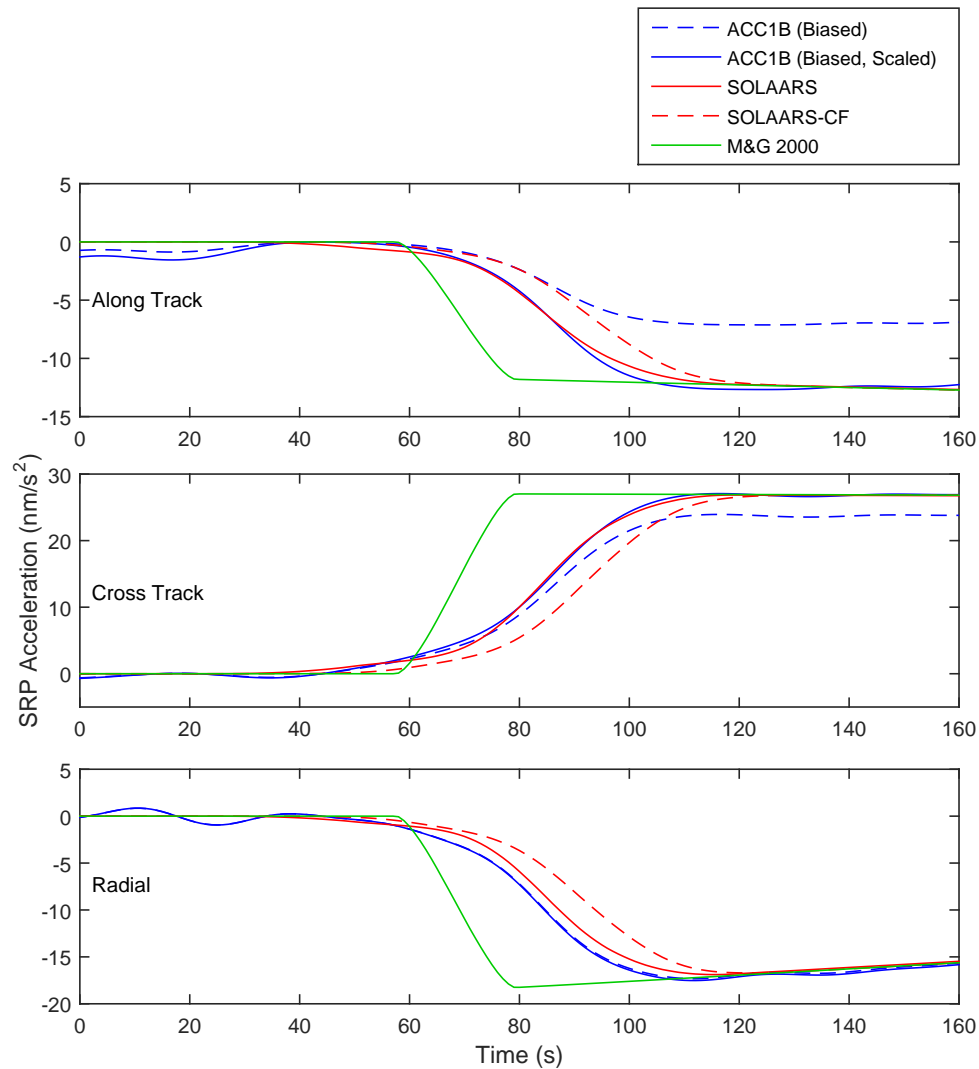


Figure 4.8: Typical example of a shadow exit of GRACE Satellite A on March 25, 2008. Accelerometer data and SRP modeling results from SOLAARS, SOLAARS-CF, and the model from Montenbruck and Gill (2000) are shown.

1993).

#### 4.1.5 Issues to consider

Good agreement with GRACE accelerometer data provides some level of validation for our penumbra SRP model. However, there are some issues that limit the value of these comparisons. First, the accelerometer data contains all non-gravitational accelerations, not only SRP. There are usually only a few penumbra SRP signals in each day of GRACE accelerometer data that are so sharp and well defined as the ones shown in Fig. 4.7 and Fig. 4.8, and a good match of observations and SRP modeling results is only obtained when the transition clearly stands out in the accelerometer signal.

Clear penumbra SRP acceleration observations require residual drag and winds to change slowly, and thruster activations should not be present at the time of the transition. For a typical transition signal, the acceleration rate of change is about  $0.6 \text{ nm/s}^2/\text{s}$ . For most of the GRACE mission, the acceleration rate of change due to drag and wind is less than  $0.1 \text{ nm/s}^2/\text{s}$ . During geomagnetic storms however, acceleration variability increases by several orders of magnitude. Under such conditions, the penumbra transition signal is obscured by drag signals and cannot be clearly distinguished (Doornbos et al., 2010). Overall, however, there are plenty of very clear penumbra transition signals to be investigated throughout the GRACE mission. For each penumbra SRP comparison we make, we assume that no other accelerations are changing significantly on that time scale and subtract a bias equal to the observed acceleration just outside of umbra from the accelerometer data.

Another issue in comparing with GRACE accelerometer data involves our GRACE optics function ( $\vec{O}$ ). While our model for the solar radiation fields is highly physical and precise, our optics function (based on the GRACE panel model) is relatively simple. Cheng et al. (2007) found that only by effectively scaling the SRP contributions of the port and starboard solar arrays by over 50 % were they able to produce good agreement with accelerometer observations. Similarly, we found that various adjustments to the panel properties would improve the fit of SRP accelerations to modeling results. However, no adjustments could be found that worked for all cases. One adjusted model may fit for a few days, and then no longer fit once the orbit-sun geometry has changed. Note that before carrying out this effort to compute adjustment factors for the macro model, the accelerometer scale factors from Bettadpur (2009), which are obtained from orbit determination, had already been applied.

A thorough estimation effort using the magnitudes of these penumbra steps in the ACC1B data, GRACE attitude and position data, and solar ephemerides, could conceivably be used to generate an empirical optics function. Since our focus is not on the optics function, but, rather, the solar radiation fields, we simply use the eight-panel model unchanged and scale the accelerometer data in each of the satellite reference frame directions so that its change during the transition matches the modeled change. By looking at results for a series of penumbra transitions, rather than selecting a single well defined signal, we can see their

variability.

#### 4.1.6 A series of subsequent transitions

Fig. 4.9 shows ACC1B data (scaled and biased) and SRP modeling results for a series of 43 shadow exits of the GRACE A satellite over a three day period centered around the January 22, 2008 transition shown in Fig. 4.7. Again, ACC1B data is biased to equal zero on the umbra end of the transition. All results are scaled based on the factors used for the exceptionally clean observation in Fig. 4.7. Again, the figure shows accelerometer data and SRP modeling results for the along track, cross track, and radial components in the GRACE satellite reference frame. Over time, the  $\beta'$  orbit angle (not to be confused with the  $\beta$  solar emission angle we use here) between the Sun direction and the orbital plane of the GRACE satellites changes. This changing  $\beta'$  angle causes the changing amplitude of the along and cross track components in SRP modeling results. During the 3 days covered by Fig. 4.9, the angle between orbital plane and the light rays does not change significantly, so this change in the magnitude of SRP acceleration changes is small, however clear in the modeling results.

The subsequent transitions shown in Fig. 4.9 show good agreement between SOLAARS and the accelerometer data, however there are a number of transitions that show significant disagreement with modeling results. In some of these cases, there are clearly other accelerations coinciding with the penumbra transition SRP signal, especially in the radial direction. However, some other accelerometer series that do not coincide closely with modeling results show clear penumbra transition behavior. For a better fit with the model, these transitions would require different scaling (presumably due to errors in the GRACE plate model). There is a clear pattern which shows greater SRP towards umbra (i.e. more of a penumbra tail) in the modeling results than in the ACC1B data. This could be the result of clouds in the atmosphere. Modeling results were computed for zero cloud top height ( $h_{CT} = 0$ ) (see Section 3.6.4), so effectively a cloudless atmosphere. As we will point out in Section 4.1.8 with Fig. 4.10b, higher cloud top heights ( $h_{CT}$ ) attenuate the penumbra tail and would produce better agreement with the observations in Fig. 4.9.

We can conclude that the SOLAARS, and to a lesser degree SOLAARS-CF, models effectively describe the radiation reaching the GRACE satellites at each time during penumbra transitions. This suggests that the most relevant processes affecting radiation during its path through the atmosphere are taken into account. However, comparisons with un-scaled accelerometer data confirm that, as Cheng et al. (2007) points out, the interaction of solar radiation with GRACE satellite surfaces using the simple plate model is inaccurate. While these accelerometer time series are somewhat limited for this application, they provide a more direct look at penumbra SRP accelerations than was previously available and validate the accuracy of our modeling.

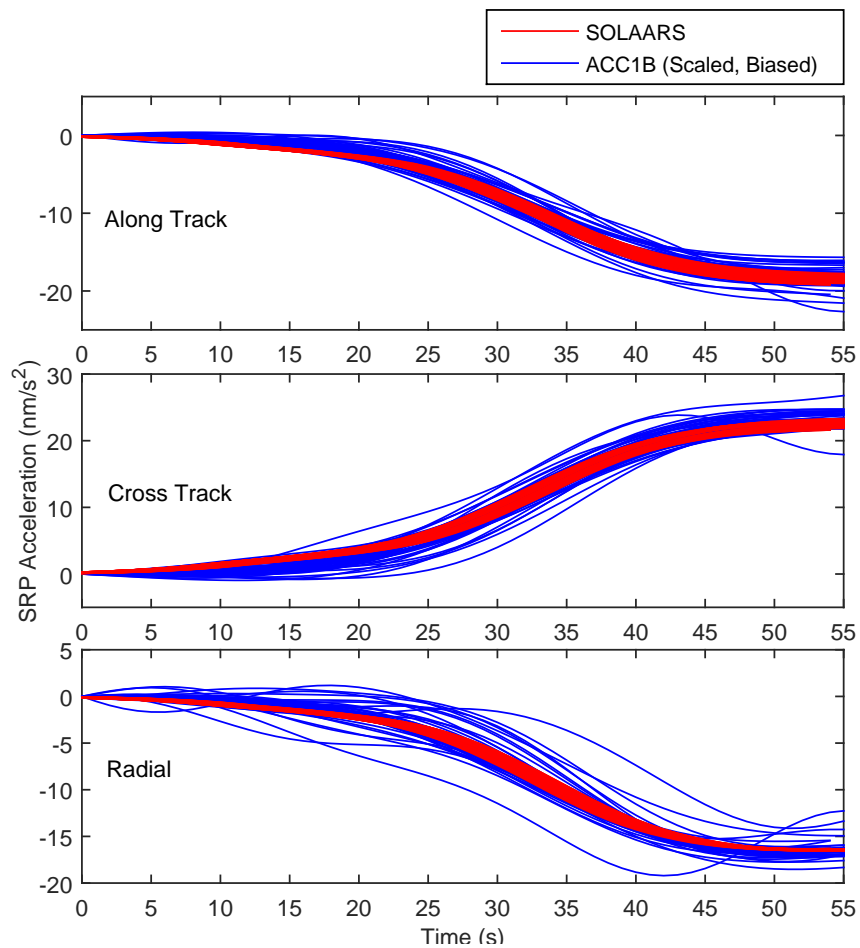


Figure 4.9: Accelerometer data and SRP modeling results from our precise model for 43 subsequent shadow entries of GRACE Satellite A on January 21-23, 2008.

### 4.1.7 Sensitivity analysis

SOLAARS is driven by many input variables (see Fig. 3.2). Some of these inputs are straightforward to assign (e.g. mean solar radiance ( $L_{\odot}$ ), solar radius ( $R_{\odot}$ ), satellite position ( $r$ ), etc.), while others are based on somewhat unpredictable atmospheric conditions. It is important to quantify the sensitivity of our model to these uncertain inputs, so that we can understand which ones are important to precisely assign. If a realistic level of change in one of these inputs produces output variations on the same scale as the difference between our model and a simple model, it needs to be assigned carefully. This ensures that our model actually provides an advantage over simpler methods. Figs. 4.10a, 4.10b, and 4.10c show modeling results for a single GRACE penumbra transition produced using different values of uncertain inputs. Fig. 4.10d is included to illustrate the importance of Earth oblateness modeling by showing results when this factor is ignored and different spherical Earth radii are used in SOLAARS. Fig. 4.10e illustrates the influence of the number of light rays used to model each solar radiation field on modeling results. For comparison with these sensitivity analysis results, Fig. 4.10f shows results from SOLAARS with results from the M&G 2000 model and 4.10g shows results from modeling without considering spectral composition changes and modeling with only Rayleigh scattering (like Vokrouhlický et al. 1993).

Figs. 4.10a, 4.10b, and 4.10c show that inputs related to atmospheric effects have the strongest influence near umbra, when the sunlight is passing further through and lower in the atmosphere. The atmosphere models referenced in Fig. 4.10a determine the altitude profiles of density ( $\rho$ ) and gas mixing ratios ( $M$ ) used in modeling. These curves indicate that variations in the 1966 US Standard Atmosphere profiles do not lead to significant changes in penumbra SRP. The results suggest that it is not practical to carefully assign density and mixing ratio profiles unless we can reduce the uncertainty imposed by other input parameters. The high cloud top height ( $h_{CT}$ ) value of 12.2 km and high aerosol profile do result in significant changes in penumbra SRP behavior (see Fig. 4.10b and 4.10c). However, we should consider that these conditions are not common. Lelli et al. (2011) indicates that cloud top height ( $h_{CT}$ ) values as high as 12.2 km are rare at most latitudes, and the high aerosol profile is the result of an uncommon set of conditions: high humidity, an extreme upper atmospheric state, and an extreme level of volcanic activity.

The input that produces the largest differences in penumbra SRP is Earth radius ( $R_{\oplus}$ ), with results shown in Fig. 4.10d. Sensitivity to Earth radius is nearly as large as the effect of using the M&G 2000 model. The significance of sensitivity to Earth radius is compounded by the fact that, unlike the other important inputs, we can expect it to closely approach its boundary values (i.e. polar and equatorial radii) as the Earth-Sun-satellite geometry varies. This shows that to accurately model penumbra transitions, the Earth oblateness model should be implemented for accurate modeling of penumbra transition timing.

The results shown in Fig. 4.10g are meant to represent the methods from Vokrouhlický et al. (1993). It is clear that, at least for GRACE, considering the changes in spectral composition

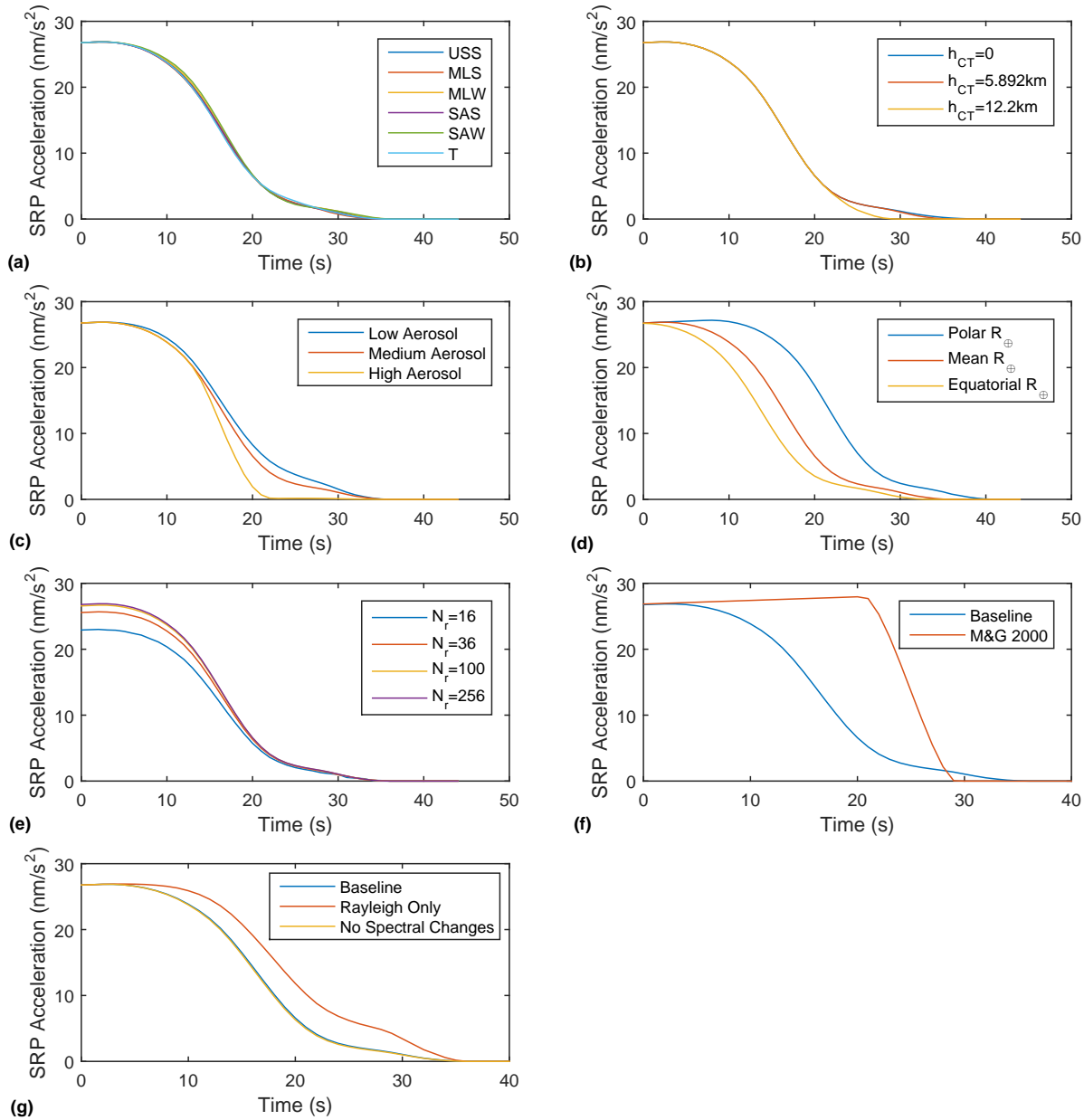


Figure 4.10: Sensitivity of SRP modeling results to varying input conditions/methods: (a) standard atmosphere model, (b) cloud top height, (c) aerosol profile (see Table 3.1), (d) Earth radius, (e) number of light rays used ( $N_R$ ), (f) comparison with the M&G 2000 model, and (g) comparison with modeling without effects ignored by Vokrouhlický et al. (1993). Note that “baseline case” in (e) and (f) refers to results from our full model using the USS atmosphere model, a 5.892 km cloud top height, mean Earth radius, medium aerosol profile, and 196 light rays.

of sunlight during penumbra transitions does not significantly influence SRP acceleration results. Therefore, it is practical to use just one wavelength bin in SOLAARS modeling for GRACE. Modeling without the extinction processes considered in SOLAARS in addition to the Rayleigh scattering considered in Vokrouhlický et al. (1993) has a significant influence on modeling results. The “Rayleigh Only” curve shows that the other extinction processes not considered in previous penumbra SRP models are important to include.

Van Helleputte et al. (2009) demonstrates a clear correlation between the  $\beta'$  orbit angle and GRACE K-band range residuals. These increased residuals are correlated with the orbit-Sun geometry, pointing to SRP acceleration modeling as a potential contributor. The minimum range residuals in Van Helleputte et al. (2009) occur at beta prime angles of magnitudes greater than 66 deg., when, according to our penumbra SRP model, the satellites are in full sunlight with no penumbra transitions. This suggests that errors in penumbra SRP modeling could be contributing to this oscillating range residual behavior. However, this  $|\beta'|$  correlation could also be driven by the modeling of the GRACE geometry and optical properties, which was done using a simple cannonball model in Van Helleputte et al. (2009).

The absolute value of the  $\beta'$  orbit angle determines penumbra SRP behavior. As the orbit-Sun orientation approaches full sunlight periods, the penumbra transitions become longer. As the transitions become longer, the significance of any errors in penumbra SRP force modeling become more significant to orbit propagation or orbit determination because acceleration errors are integrated over longer penumbra time periods. To quantify the effect of the most significant input uncertainty, aerosol conditions, we integrate the difference between the high aerosol and low aerosol SRP acceleration results in Fig. 4.10c. This gives us a single maximum change in velocity,  $\Delta v$ , induced by a particular uncertain input or modeling option for a given penumbra transition. Fig. 4.11a shows these  $\Delta v$  values computed for a single penumbra transition each day (not including days without penumbra transitions) between January 21, 2008 and June 27, 2008. Additionally, Fig. 4.11a shows  $\Delta v$  results for the integrated difference between baseline SOLAARS results and M&G 2000 results, so we can check that SOLAARS errors caused by input uncertainty will always be smaller than errors caused by using the simpler M&G 2000 model. This gives us results over a full range of  $\beta'$  orbit angle magnitudes (i.e.  $|\beta'|$ ), which are shown in Fig. 4.11b.

As the  $\beta'$  magnitude shown in Fig. 4.11b increases, with the orbit approaching a full sunlight phase, the potential for larger penumbra SRP error increases as well. This growth in error near full sunlight phases matches the behavior of GRACE K-band range residuals from Van Helleputte et al. (2009). The  $\Delta v$  values from using the M&G 2000 atmosphere-free model are about five times larger than the errors induced by uncertainty in aerosol conditions. Therefore, even unusually large aerosol uncertainties are not significant enough to invalidate the SOLAARS model.

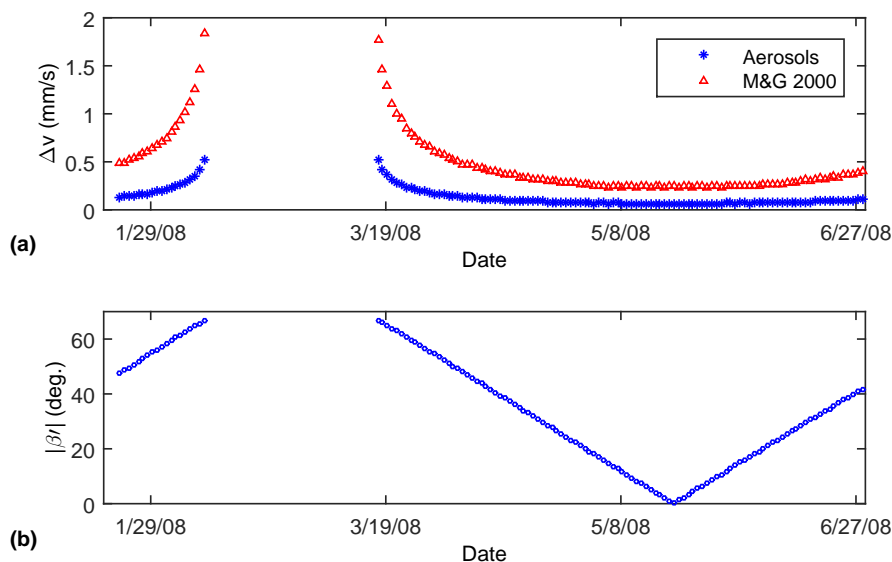


Figure 4.11: Sensitivity of modeling results to the  $\beta'$  orbit angle. This sensitivity is presented as a  $\Delta v$  integrated difference between the extrema of penumbra SRP accelerations (for a single transition on each date) modeled using the high and low aerosol profiles and between baseline SOLAARS and M&G 2000 results. (a) shows the  $\Delta v$  results and (c) shows the magnitude of  $\beta'$  orbit angles.

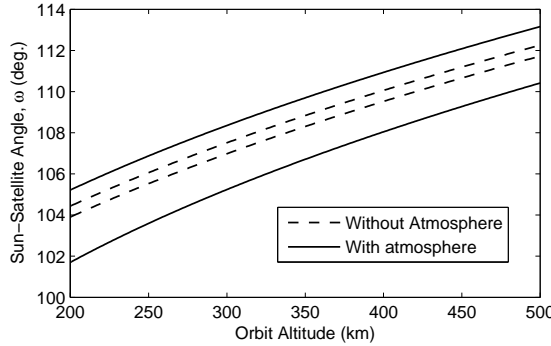


Figure 4.12: Comparison of penumbra transition limits.

#### 4.1.8 A note on penumbra boundaries

As previously discussed in Chapter 2, various approaches to modeling penumbra SRP define the penumbra region based on an atmosphere-free Earth and prescribe that SRP smoothly drop-off in that region. McMahon and Scheeres (2010) point out that a lack of symmetry in umbra entrance and exit transitions could lead to large changes in secular terms used to model SRP effects on long term orbit dynamics. Running our model for GRACE did not show significant asymmetries in the length of umbra entry/exit pairs of transitions (< 1% for any of those in the time period addressed in Fig. 4.11). However, there are two caveats we should consider: First, we have demonstrated that varying atmospheric conditions can significantly influence penumbra SRP, and therefore some level of asymmetry should at least be considered in estimating the uncertainty in these secular terms. Second, secular rates are also influenced by the total length of time spent in penumbra and under the influence of SRP, and a simple model of the shape of the penumbra region underestimates its size. Fig. 4.12 shows the penumbra boundaries as a function of Sun-Earth-satellite angle ( $\omega$ ) and orbit altitude for our model and an atmosphere-free model like the one from Montenbruck and Gill (2000).

It is clear that the shape of the penumbra region changes significantly when it is more precisely bounded by the beginning of atmospheric extinction and the end of refracted sunlight as illustrated in Fig. 3.1. Our comparisons to GRACE accelerometer data show that considering atmospheric effects gives an improved understanding of the location and size of the penumbra region. It is possible that the relatively simple SOLAARS-CF model is too complex for a particular application or does not work within some selected mathematical framework. In these cases, modelers could significantly improve penumbra SRP modeling accuracy by simply using the boundaries shown in Fig. 4.12 with whatever mathematical function being used to describe attenuation of SRP in penumbra .

## 4.2 Application to the Earth flyby anomaly

Numerous deep-space missions have used Earth flybys to gain or lose heliocentric orbital energy en-route to their destinations. During a number of these gravity assist maneuvers, beginning with the first Galileo Earth flyby in December of 1990, mission operators have observed motion that cannot be explained by their detailed force models. Numerous explanations have been unsuccessfully proposed and investigated as the source of the Earth flyby anomaly. In this section, we investigate solar radiation pressure (SRP) modeling during penumbra transitions as a contributor to or explanation for the anomaly. We compare propagated Earth flyby trajectories generated using the SOLAARS-CF model to propagated trajectories generated using the simpler M&G 2000 model, which is representative of what is typically used in orbit determination (OD) programs.

During Earth flybys, spacecraft follow hyperbolic trajectories which take them close to Earth. During these maneuvers, ground based Doppler radars precisely track the spacecraft. Doppler radar observations are assimilated by orbit determination programs which include detailed models of the significant known forces acting on the spacecraft. Unfortunately, limitations on the ability of radars to track spacecraft motion near perigee lead to Doppler blackout periods around perigee on the order of hours. On numerous occasions, the pre-encounter and post-encounter flyby trajectory estimates do not match one another. This disagreement points to either measurement errors or a change in orbital energy during these perigee passes that is not captured in the force models used in the orbit determination system. (Anderson et al., 2008)

The unexplained change in orbital energy of the Earth flyby anomaly is described by the anomalous change in hyperbolic excess velocity,  $\Delta v_\infty$ . The scalar hyperbolic excess velocity is defined as:

$$v_\infty^2 = \vec{v} \cdot \vec{v} - \frac{2\mu}{r} \quad (4.5)$$

The anomalous change in hyperbolic excess velocity is the difference in  $v_\infty$  between the post-encounter and pre-encounter estimated trajectories. Table 4.1 shows  $\Delta v_\infty$  values, estimated errors in the  $\Delta v_\infty$  values and other relevant parameters for the past anomalous Earth flybys. In addition to the past flybys, information is provided for the October 2013 Juno Earth flyby, which had not yet occurred at the outset of this work. Recent analysis of the Juno flyby indicates that no anomalous  $\Delta v_\infty$  was observed (Thompson et al., 2014). Reported values of  $\sigma_{v_\infty}$  in Table 4.1 illustrate the uncertainty caused by the high atmospheric drag in the 1992 Galileo flyby and thruster activity in the Cassini flyby which caused difficulty in identifying the anomaly (Anderson et al., 2008). The MESSENGER flyby data did not significantly exhibit the effects of the anomaly.

Since the Earth flyby anomaly was first identified following the 1990 Galileo flyby, researchers have proposed a broad range of explanations for the anomaly. Lammerzahl et al. (2008)

Table 4.1: Data from past Earth flyby anomalies up to MESSENGER (labeled MSGR) from Anderson et al. (2008) and recent Juno  $\Delta v_\infty$  and  $\sigma_{v_\infty}$  values are from Thompson et al. (2014). Note that the majority of observed anomalous  $\Delta v_\infty$  values are at least an order of magnitude greater than the estimated errors in hyperbolic excess velocities. The Juno spacecraft mass used here is from NASA (2011) and is a beginning of mission value.

Spacecraft	Galileo	Galileo	NEAR	Cassini	Rosetta	MSGR	Juno
Flyby Date	12/8/90	12/8/92	1/23/98	8/18/99	3/4/05	8/2/05	10/9/13
S/C Mass (kg)	2497	2497	730	4612	2895	1086	3625
Perigee Alt. (km)	960	303	539	1175	1956	2347	562
$v_\infty$ (km/s)	8.949	8.877	6.851	16.010	3.863	4.056	-
$\Delta v_\infty$ (mm/s)	3.92	-4.6	13.46	-2	1.8	.02	0
$\sigma_{v_\infty}$ (mm/s)	0.3	1.0	0.01	1	0.03	0.01	<1

presents a summary of these explanations which include hardware and Doppler ranging related issues, errors in modeling well-known environmental forces, and more exotic explanations that concern new physics such as non-Newtonian gravity and modifications of relativity. The study presented in Atchison et al. (2010) examined Lorentz accelerations as a potential cause of the anomaly.

In some respects, penumbra SRP modeling appears to be a promising candidate for explaining the flyby anomaly. Anderson et al. (2008) precisely fits an expression that provides the  $\Delta v_\infty$  values from past anomalies based on the orbital inclinations of the flyby trajectories. The SOLAARS-CF model considers oblateness, which leads to a correlation between orbital inclination and penumbra SRP. Additionally, including the atmosphere significantly changes the shape of the penumbra region (see Fig: 4.12) which could lead to penumbra transitions completely missed by simpler, atmosphere-free models. This connection between SRP force and inclination is not captured by the traditional non-physical SRP models. However, we can easily show that penumbra SRP modeling is not completely responsible for the flyby anomaly. First, only Galileo during the 1990 flyby and Cassini during its flyby passed into Earth's penumbra. Additionally, Lammerzahl et al. (2008) estimates that the anomalous acceleration is on the order of  $10^{-4}$  m/s $^2$ , which is far greater than the nm/s $^2$  scale SRP accelerations of these spacecraft.

Regardless of this conclusion that SRP is not the sole reason for the anomaly, the influence of penumbra SRP modeling could be greater than the estimated errors. Therefore we followed through with this investigation to evaluate whether penumbra SRP modeling has a significant influence on the anomaly, and therefore could be used to better understand or predict the cause. In this study, we focus on the flybys which did experience penumbra transitions: Galileo's 1990 flyby and the Cassini and Juno Earth flybys.

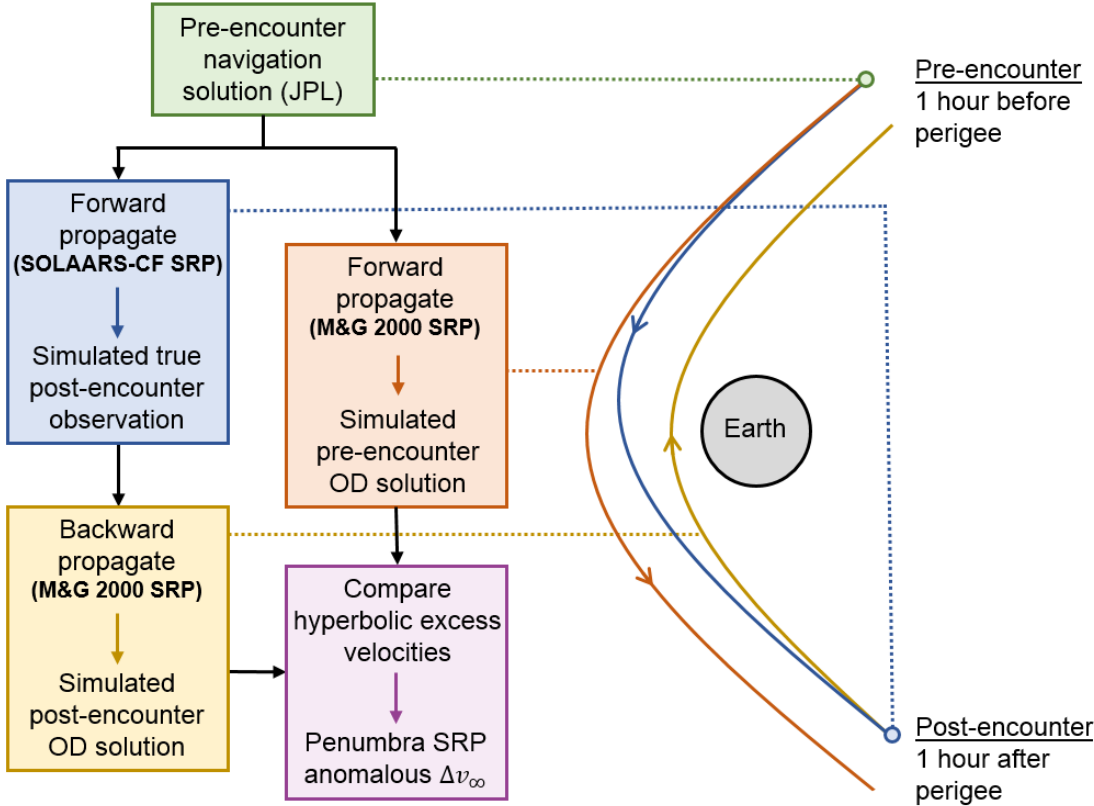


Figure 4.13: Process for estimating the contribution of penumbra SRP to the flyby anomaly. We compute a penumbra SRP anomalous  $\Delta v_\infty$  by comparing the hyperbolic excess velocities of the simulated pre-encounter and post-encounter OD solutions at each time step.

#### 4.2.1 Computing the penumbra SRP anomaly contribution

We quantify the influence of penumbra SRP on the anomaly without implementing an orbit determination framework. We do this by generating and comparing simulated pre-encounter and a post-encounter flyby trajectories. For each of the three flybys addressed here (Galileo 1990, Cassini, and Juno), we propagate three trajectories through a two hour Doppler blackout period centered at perigee. Fig. 4.13 illustrates these three trajectories and describes the flow of information between the orbit propagation processes.

We assume that the trajectory forward propagated using the SOLAARS-CF model represents the true trajectory of the spacecraft and the trajectories propagated using the simpler M&G 2000 penumbra SRP model represent OD solutions for the pre-encounter and post-encounter fitted trajectories. The post-encounter, final state solution of the true trajectory is used as a post-encounter observation. This simulated observation serves as the starting point for backward propagation of the simulated post-encounter OD solution using the M&G 2000 model. Pre-encounter navigation solutions for the initial states of the simulated true

trajectory and pre-encounter OD solution are provided by the JPL HORIZONS system. To our knowledge, the Juno navigation solution has not been used to update the HORIZONS dataset, and the initial state used here is a preliminary estimate.

The orbit propagator includes models of other orbital perturbations in addition to SRP. Residual air drag forces are modeled using the J70 atmosphere model (Jacchia, 1971). Third body gravity forces are included for the Sun and Moon. The irregularities in Earth's gravity field are modeled according to Vallado (2001) using a 10<sup>th</sup> degree and order implementation of the EGM96 gravity field model. We use the SPICE toolkit to obtain precise planetary and solar ephemerides and Earth orientations (Acton, 1996).

The SOLAARS-CF and M&G 2000 SRP models are implemented such that modeled solar radiation fields outside the penumbra periods are identical. Towards the same aim, both modes of operation for the orbit propagator use the same method for modeling the SRP force imposed on a spacecraft by a given solar radiation field. Since the focus of this work is investigating the effect of modeling the SRP interactions with the atmosphere, we use simple models of spacecraft geometry and optical properties. Cassini and Galileo have irregular, compact geometries as a result of their radioisotope thermoelectric power sources. These irregular geometries are approximated as spheres. Conversely, Juno is solar powered, and therefore has a higher area-to-mass ratio and a more uniform, flat geometry. The Juno geometry is approximated as a flat plate pointing to the Sun. Optical properties are applied based on the dominant outer material on the three spacecraft. For the Cassini and Galileo spacecraft, this material is reflective aluminized kapton (Doody, 2009). For Juno, the dominant (Sun pointing) surfaces are solar panels.

### 4.2.2 SRP accelerations

Fig. 4.14 shows the behavior of the SOLAARS-CF and M&G 2000 penumbra SRP accelerations which were used for propagation of the spacecraft trajectories. For comparison, the results of the full SOLAARS model were computed at the SOLAARS-CF propagated positions. Like GRACE SRP results, the SOLAARS-CF results are quite close to the SOLAARS results, demonstrating the quality of this approximate method. As expected, SRP results from the M&G 2000 model show more consistent, linear attenuation of SRP in the penumbra region. The SOLAARS SRP accelerations show significantly more variation and longer transitions.

The increased length of SOLAARS transitions is caused by refraction of light around the Earth by the lower atmosphere. The umbra ends of these SOLAARS transitions are characterized by a tail region. During the majority of these tail phases, the full limits of the solar radiation field are visible from the perspective of the spacecraft, however SRP is significantly attenuated due to extinction and refractive beam divergence. Extinction and divergence of solar flux increases as the light takes successively longer paths through the atmosphere at successively lower altitudes. Timing offsets between the two models are caused by Earth

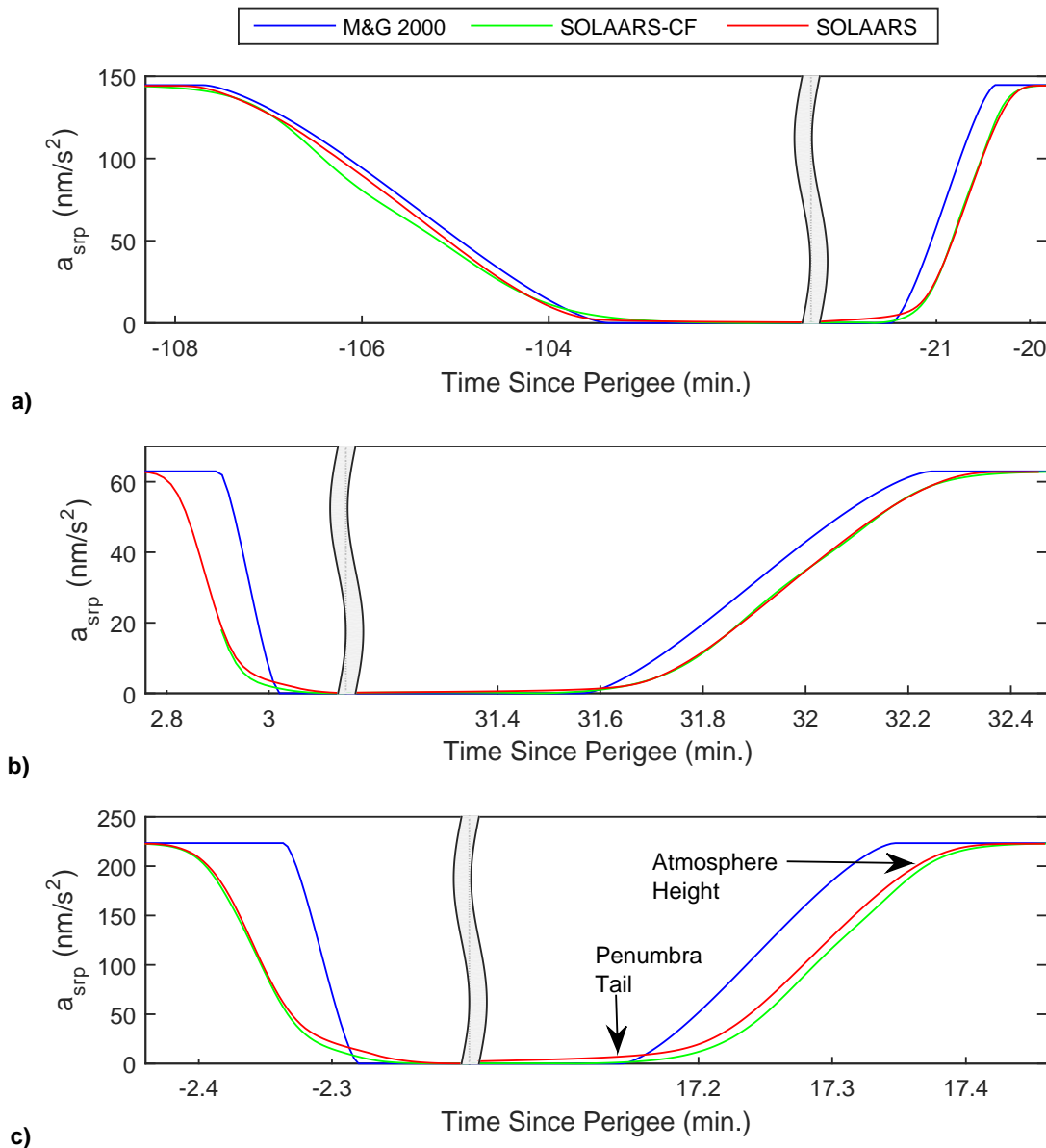


Figure 4.14: SOLAARS-CF, full SOLAARS, and M&G 2000 penumbra SRP modeling results for a) 1990 Galileo, b) Cassini, and c) Juno Flybys. Note that the full SOLAARS was not used in propagation of any the trajectories, but was applied to the trajectory solution from SOLAARS-CF for comparing SRP acceleration results.

oblateness effects and by the height of the atmosphere. Penumbra transitions into shadow begin later for SOLAARS when light rays are passing over high-latitudes where Earth's radius is smaller than at mid-latitudes. The height of the SOLAARS atmosphere is 50 km, which adds to the Earth radius and, in the case of a sunset transition, begins scattering solar radiation before the M&G 2000 model recognizes any obstacle for the solar flux.

The effects considered by SOLAARS create two distinct regions which are labeled in plot (c) of Figure 4. The tail produces greater SRP near umbra, while the atmosphere height leads to an earlier start to the transition into umbra. These details drive the disagreement between the SOLAARS-CF and M&G 2000 penumbra SRP accelerations as shown in Fig. 4.14; however, the degree to which this disagreement translates into the anomalous  $\Delta v_\infty$  is driven by the magnitude of SRP accelerations and lengths of the transition periods.

### 4.2.3 Error estimation and anomaly behavior

In order to resolve the small influence of penumbra SRP on the anomaly, it is necessary to integrate flyby trajectories with tight tolerances. We use an explicit Runge-Kutta 4th/5th order integrator to propagate the spacecraft trajectories. To ensure numerical discretization errors are not significantly influencing our modeling results, we estimate  $\Delta v_\infty$  errors by generating two additional trajectories for each spacecraft. After forward propagating with each SRP model, we then backward propagate from the final state of each trajectory solution with the same model, e.g. we forward propagate with SOLAARS-CF, then backward propagate over the same time period from the final SOLAARS-CF propagated state.

The hyperbolic excess velocities ( $v_\infty$ ) at each time step in these backward propagated trajectories are compared to the values for their forward propagated counterpart to estimate error ( $\sigma_{v_\infty}$ ). In the absence of numerical integration errors, these values would be zero. Fig. 4.15 shows the SOLAARS-CF and M&G 2000 error estimates as a function of time since perigee for the 1990 Galileo flyby. Regardless of adaptive step size selection, these errors consistently exhibit the peaks around perigee shown in Fig. 4.15. We sum the maximum absolute value of these two error estimates to produce our anomaly error estimate.

In addition to the behavior of these error estimates, Fig. 4.15 shows the behavior of the anomaly over the modeling period. The anomaly consistently exhibits the same peaks around perigee that are prevalent in the error estimates. Variations in  $\Delta v_\infty$  over the modeling period are on the level of error, and therefore  $\Delta v_\infty$  is effectively constant over the trajectory. This indicates that whatever anomaly is caused by disagreement between the forward propagated trajectories is not significant enough to cause the anomaly to grow during backward propagation of the third, post encounter trajectory. This growth during backward propagation could conceivably occur, given a significant enough disagreement between the forward propagated trajectories to cause the timing and dynamics of the SRP and other perturbations in backward propagation to vary significantly. However, this was not observed in any of the three cases we addressed. Error estimation results for all three spacecraft exhibit the

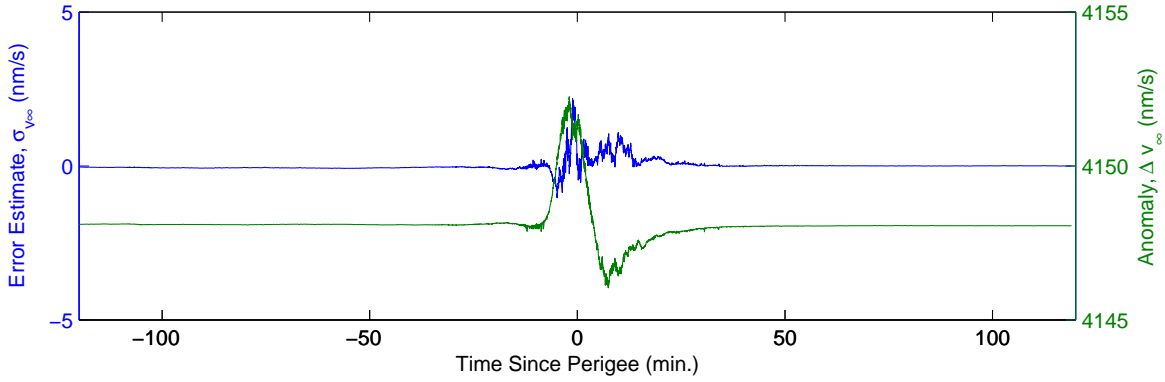


Figure 4.15: Anomaly error estimate ( $\sigma_{v_\infty}$ ) and  $\Delta v_\infty$  results for 1990 Galileo Flyby.

Table 4.2: Estimated penumbra SRP anomalous  $\Delta v_\infty$  contributions and estimated error in these contributions ( $\sigma_{v_\infty}$ ). The time spent in penumbra ( $\Delta t_p$ ) and full sunlight SRP acceleration magnitude ( $a_{SRP}$ ) are included to illustrate their correlation with anomaly results.

Flyby	Galileo 1990	Cassini	Juno
Penumbra SRP $\Delta v_\infty$ (nm/s)	4150	597	1180
$\sigma_{v_\infty}$ (nm/s)	2.19	0.281	17.3
$a_{SRP}$ (nm/s <sup>2</sup> )	144	63.0	223
$\Delta t_p$ (s)	563	103	39.4

behavior shown in Fig. 4.15.

#### 4.2.4 Penumbra SRP contribution to the anomaly

Table 4.2 summarizes our results for the penumbra SRP contributions to the anomaly. Error estimates for each case in Table 4.2 are all less than 2% of the anomaly results. Key drivers of the penumbra SRP anomaly contribution are included as well: full sunlight SRP acceleration and time spent in SOLAARS-CF penumbra. The anomaly estimate for Galileo is significantly higher than the others. This larger anomaly is caused by the length of time Galileo spent in penumbra during its Earth flyby. However, even this larger Galileo penumbra SRP anomaly is at least three orders of magnitude smaller than those reported for the flyby anomalies. These results show that penumbra SRP has made negligible contributions to the Earth flyby anomalies for Galileo, Cassini, and Juno.

# Chapter 5

## Conclusions and Future Work

### 5.1 Review

#### 5.1.1 Application to the GRACE satellites

Using GRACE accelerometer observations, we have shown that modeling the location and size of the penumbra region without considering atmospheric effects leads to errors in the timing and length of penumbra transitions. Additionally, atmosphere-free approaches which result in a symmetric curve of SRP attenuation in penumbra do not capture the complex shape of SRP acceleration curves produced by atmospheric refraction and extinction. Comparisons with GRACE accelerometer data offer a unique opportunity to validate our methods, and these comparisons demonstrate the accuracy of our model.

The SOLAARS sensitivity analysis for the GRACE orbit shows that penumbra SRP is sensitive to Earth oblateness and various unpredictable atmospheric conditions. Earth oblateness and aerosol conditions in the atmosphere are particularly important in determining the timing and behavior of SRP during transitions. While aerosol conditions may be challenging to predict or describe based on atmospheric modeling or data, our sensitivity analysis considered extreme levels of variation which are unlikely. Therefore the likelihood of significant aerosol extinction modeling errors can be mitigated by using average conditions. Errors in penumbra SRP modeling become more significant at larger  $\beta'$  orbit angles, when the orbit is near full sunlight periods.

#### 5.1.2 Application to the Earth flyby anomaly

We quantified the contribution of penumbra SRP to the Earth flyby anomaly by applying two models in an orbit propagator: an atmosphere free, spherical Earth model from Montenbruck

and Gill (2000) and the SOLAARS-CF model. We modeled penumbra SRP contributions to the Earth flyby anomaly for the recent Juno flyby, the Cassini flyby, and the 1990 Galileo flyby. The results of this study indicate that penumbra SRP is not a significant contributor to the flyby anomaly as the modeled contributions are orders of magnitude smaller than the observed anomalous  $\Delta v_\infty$  values. SRP results illustrate a significant disagreement between the more conventional M&G 2000 model and the SOLAARS-CF model, however spacecraft SRP accelerations would need to be significantly larger to lead to a considerable influence of penumbra SRP modeling on the Earth flyby anomaly.

## 5.2 Conclusions

We have built upon the previous state-of-the-art penumbra SRP model from Vokrouhlický et al. (1993) and demonstrated the significance of previously neglected atmospheric effects. Our model considers changes in the shape, radiance, and spectral composition of sunlight in penumbra due to Earth oblateness, lower atmospheric refraction, Rayleigh scattering, aerosol scattering, molecular absorption, and cloud extinction. In addition to modeling previously neglected atmospheric effects, we derived the complex light ray geometries and presented an efficient computational framework that allows us to reduce computational cost while increasing accuracy.

The accuracy of the SOLAARS model comes with a significant increase in complexity and computational cost compared to typical models. While this may limit the viability of our full model within certain orbit determination or orbit propagation schemes, it should be used to inform how penumbra SRP is modeled. We have demonstrated that atmospheric effects are the driving factor in penumbra SRP behavior. The shape of penumbra SRP acceleration curves (like those in Fig. 4.7) and the timing and duration of penumbra transitions from any simplified model should be informed by the results of a complete, highly physical model which considers atmospheric effects. The SOLAARS-CF shadow function effectively provides this simplified model for applications where computational cost is an important consideration.

## 5.3 Future work

The SOLAARS and SOLAARS-CF results presented in Chapter 4 show the improved accuracy that these models offer compared to typical penumbra SRP models. The next step is to continue applying these models to determine what, if any, is the improvement that will be achieved in the final data products. The application that shows the most promise for immediate improvement through SOLAARS SRP modeling is thermosphere density and wind retrieval from satellite accelerometry. Some initial work has begun on this front using SOLAARS-CF in GOCE wind and density retrieval, but more analysis is needed to quantify the improvements. Precise orbit determination is another application that currently shows

promise for improvement using SOLAARS and SOLAARS-CF. Again, initial work has begun with the SOLAARS-CF model being applied to GPS satellite orbit determination and more work is needed to quantify the improvements.

These initial GOCE and GPS applications have only utilized the simpler but less precise SOLAARS-CF model. The coding required to transfer the SOLAARS-CF model to other programming languages is trivial, while the effort required for the full SOLAARS model is much more complicated. The SOLAARS-CF model has been successfully transferred from MATLAB to FORTRAN, which is a common language used in precise orbit determination and wind and density retrieval. The same conversion is necessary for SOLAARS. Implementing SOLAARS in more application oriented languages and offering it to the public will help encourage others to integrate this precise model into their application specific codes and ensure that its complexity doesn't limit its usefulness to the scientific and engineering communities.

# Bibliography

- Acton, C. (1996). Ancillary data services of nasa's navigation and ancillary information facility. *Planetary and Space Science* 44(1), 65–70.
- Adhya, S., A. Sibthorpe, M. Ziebart, and P. Cross (2004). Oblate Earth eclipse state algorithm for low-Earth orbiting satellites. *Journal of Spacecraft and Rockets* 41(1), 157–159.
- Anderson, G. P., J. H. Chetwynd, S. A. Clough, E. P. Shettle, and F. X. Kneizys (1986). AFGL atmospheric constituent profiles (0-120km). Technical Report AFGL-TR-86-0110, Air Force Geophysics Laboratory.
- Anderson, G. P., J. H. Chetwynd, Jr., J.-M. Theriault, P. K. Acharya, A. Berk, D. C. Robertson, F. X. Kneizys, M. L. Hoke, L. W. Abreu, and E. P. Shettle (1993). Modtran2: suitability for remote sensing.
- Anderson, J. D., J. K. Campbell, J. E. Ekelund, J. Ellis, and J. F. Jordan (2008). Anomalous orbital energy changes observed during spacecraft flybys of earth. *Physical Review Letters* 100, Paper 091102.
- Ångström, A. (1929). On the atmospheric transmission of sun radiation and on dust in the air. *Geografiska Annaler* 11, 156–166.
- ASTM (2014). Standard solar constant and zero air mass solar spectral irradiance tables.
- Atchison, J. A., M. A. Peck, and B. J. Streetman (2010). Lorentz accelerations in the earth flyby anomaly. *Journal of Guidance, Control, and Dynamics* 33, 1115–1122.
- Auer, L. H. and E. M. Standish (2000). Astronomical refraction: Computational method for all zenith angles. *The Astronomical Journal* 199(5), 2472–2474.
- Avrett, E. and R. Loeser (1984). Line transfer in static and expanding atmospheres. In W. Kalkofen (Ed.), *Methods in Radiative Transfer*, pp. 341–379. Cambridge University Press.
- Bates, D. R. (1984, June). Rayleigh scattering by air. *Planetary Space Science* 32, 785–790.

- Berk, A., G. Anderson, P. Acharya, L. Bernstein, L. Muratov, J. Lee, M. Fox, S. Adler-Golden, J. Chetwynd, M. Hoke, R. Lockwood, J. Gardner, T. Cooley, C. Borel, and P. Lewis (2005). Modtran 5, a reformulated atmospheric band model with auxiliary species and practical multiple scattering options: update. In *Algorithms and Technologies for Multispectral, Hyperspectral, and Ultraspectral Imagery XI*, Volume 5806, pp. 662–667.
- Berk, A., L. Bernstein, and D. Robertson (1989). Modtran: A moderate resolution model for lowtran 7. Technical Report AD-A214 337, Air Force Geophysics Laboratory.
- Bettadpur, S. (2007). Gravity Recovery and Climate Experiment Product Specification Document (Rev 4.5 – February 20, 2007). Technical Report GRACE 327-720/CSR-GR-03-02, Center for Space Research, The University of Texas at Austin.
- Bettadpur, S. (2009, January). Recommendation for a-priori Bias & Scale Parameters for Level-1B ACC Data (Release 00). <http://podaac-www.jpl.nasa.gov/>.
- Bird, R. E. (1982). Terrestrial solar spectral modeling. *Solar Cells* 7, 107–118.
- Bird, R. E. (1984). A simple, solar spectral model for direct-normal and diffuse horizontal irradiance. *Solar Energy* 32(4), 461 – 471.
- Bird, R. E. and C. J. Riordan (1986). Simple solar spectral model for direct and diffuse irradiance on horizontal and tilted planes at the earth's surface for cloudless atmospheres. *Journal of Climate and applied meteorology* 25(1).
- Brine, D. and M. Iqbal (1983). Diffuse and global solar spectral irradiance under cloudless skies. *Solar Energy* 30(5), 447 – 453.
- Cameron, W. S., J. H. Glenn, M. S. Carpenter, and J. A. O'Keefe (1963, June). Effect of refraction on the setting sun as seen from space in theory and observation. *The Astronomical Journal* 68, 348.
- Cheng, M., J. Ries, and B. Tapley (2007). Assessment of solar radiation model for GRACE orbit determination. *Advances in the Astronautical Sciences* 129.
- COESA (1966). *US standard atmosphere supplements, 1966*. US Government Printing Office, Washington, DC: Committee for the Extension of the Standard Atmosphere.
- Doody, D. (2009). *Deep Space Craft: An Overview of Interplanetary Flight*. Springer-Verlag.
- Doornbos, E. (2012). *Thermospheric density and wind determination from satellite dynamics*. Springer Theses. Berlin, Heidelberg: Springer.
- Doornbos, E. (2014). Goce+ theme 3: Air density and wind retrieval using goce data - data set user manual. Technical report, TU Delft.

- Doornbos, E., M. Förster, B. Fritsche, T. van Helleputte, J. van den IJssel, G. Koppenwallner, H. Lühr, D. Rees, P. Visser, and M. Kern (2010). Air density models derived from multisatellite drag observations. In *Proceedings ESA's Second Swarm International Science Meeting*.
- Doornbos, E., R. Scharroo, H. Klinkrad, R. Zandbergen, and B. Fritsche (2002). Improved modelling of surface forces in the orbit determination of ERS and ENVISAT. *Canadian Journal of Remote Sensing* 28(4), 535–543.
- ESA (1999). gravity recovery and steady-state ocean circulation mission. Technical Report ESA SP-1233(1), ESA publication division.
- Ferraz-Mello, S. (1964). Sur le probleme de la pression de radiations dans la theorie des satellites artificiels. *Comptes Rendus de l'Académie des Sciences* 258, 463.
- Ferraz-Mello, S. (1972). Analytical study of the Earth's shadowing effects on satellite orbits. *Celestial Mechanics* 5(1), 80–101.
- Flury, J., S. Bettadpur, and B. D. Tapley (2008). Precise accelerometry onboard the GRACE gravity field satellite mission. *Advances in Space Research* 42(8), 1414–1423.
- Garfinkel, B. (1944, February). An investigation in the theory of astronomical refraction. *The Astronomical Journal* 50, 169–179.
- Garfinkel, B. (1967). Astronomical refraction in a polytropic atmosphere. *The Astronomical Journal* 72(235–254).
- Gates, D. M. (1966). Spectral distribution of solar radiation at the earth's surface. *Science* 151(3710), 523–529.
- Gregg, W. and K. Carder (1990). A simple spectral solar irradiance model for cloudless maritime atmospheres. *Limnology and Oceanography* 35(8), 1657–1675.
- Gueymard, C. (1989). A two-band model for the calculation of clear sky solar irradiance, illuminance, and photosynthetically active radiation at the earth's surface. *Solar Energy* 43(5), 253 – 265.
- Gueymard, C. (2001). Parameterized transmittance model for direct beam and circumsolar spectral irradiance. *Solar Energy* 71(5), 325–346.
- Hubaux, C., A. Lematre, N. Delsate, and T. Carletti (2012). Symplectic integration of space debris motion considering several earths shadowing models. *Advances in Space Research* 49(10), 1472 – 1486.
- Irvine, W. (1975). Multiple scattering in planetary atmospheres. *Icarus* 25, 175–204.

- Jacchia, L. G. (1971). New static models of the thermosphere and exosphere with empirical temperature profiles. *Smithsonian Astrophysical Observatory Special Report 313*.
- Jursa, A. S. (Ed.) (1985). *Handbook of geophysics and the space environment*. Air Force Geophysics Laboratory Hanscom.
- Justus, C. G. and M. V. Paris (1985). A model for solar spectral irradiance and radiance at the bottom and top of a cloudless atmosphere. *Journal of Climate and Applied Meteorology 24*(3), 193–205.
- Kabeláč, J. (1988). Shadow function - contribution to the theory of the motion of artificial satellites. *Bulletin of the Astronomical Institutes of Czechoslovakia 39*(4), 213–220.
- Kneizys, F. X., E. P. Shettle, L. W. Abreu, J. H. Chetwynd, G. P. Anderson, W. O. Gallery, J. E. A. Selby, and S. A. Clough (1988). Users guide to LOWTRAN 7. *Environmental Research Papers*.
- Kozai, Y. (1961). Effects of Solar Radiation Pressure on the Motion of an Artificial Satellite. *SAO Special Report 56*.
- Lála, P. (1971). Semi-analytical theory of solar pressure perturbations of satellite orbits during short time intervals. *Bulletin of the Astronomical Institutes of Czechoslovakia 22*(2), 63–72.
- Lála, P. and L. Sehnal (1969). The Earth's shadowing effects in the short-periodic perturbations of satellite orbits. *Bulletin of the astronomical institutes of Czechoslovakia 20*, 328.
- Lammerzahl, C., O. Preuss, and H. Dissus (2008). Is the physics within the solar system really understood? In *Lasers, Clocks, and Drag-Free Control*, pp. 75–98. Springer-Verlag, Berlin.
- Leckner, B. (1978). The spectral distribution of solar radiation at the earth's surfaceelements of a model. *Solar Energy 20*(2), 143 – 150.
- Lelli, L., A. A. Kokhanovsky, V. V. Rozanov, M. Vountas, A. M. Sayer, and J. P. Burrows (2011, August). Seven years of global retrieval of cloud properties using space-borne data of GOME-1. *Atmospheric Measurement Techniques Discussions 4*, 4991–5035.
- Link, F. (1962). Eclipses de satellites artificiels. *Bulletin of the Astronomical Institutes of Czechoslovakia 13*(1), 1–8.
- McCartney, E. J. (1976). *Optics of the atmosphere: Scattering by molecules and particles*. New York: Wiley.
- McMahon, J. W. and D. J. Scheeres (2010). New solar radiation pressure force model for navigation. *Journal of Guidance, Control, and Dynamics 33*, 1418–1428.

- Montenbruck, O. and E. Gill (2000). *Satellite orbits - models, methods and applications*. Berlin, Heidelberg, New York: Springer-Verlag.
- Moon, P. (1940). Proposed standard solar-radiation curves for engineering use. *Journal of the Franklin Institute* 230(5), 583 – 617.
- NASA (2011, August). Juno launch press kit. Online, “[http://www.jpl.nasa.gov/news/press\\_kits/JunoLaunch.pdf](http://www.jpl.nasa.gov/news/press_kits/JunoLaunch.pdf)”.
- NIMA (2000, January). Department of defense world geodetic system. Technical Report TR8350.2, National Imagery and Mapping Agency.
- Picard, A., R. S. Davis, M. Glser, and K. Fujii (2008). Revised formula for the density of moist air (cipm-2007). *Metrologia* 45(2), 149.
- Reigber, C., P. Schwintzer, and H. Lühr (1999). The CHAMP geopotential mission. In I. Marson and H. Sünkel (Eds.), *Bollettino di Geofisica Teoretica ed Applicata*, Vol. 40, No. 3-4, Sep.-Dec. 1999, *Proceedings of the 2nd Joint Meeting of the International Gravity and the International Geoid Commission, Trieste 7-12 Sept. 1998, ISSN 0006-6729*, pp. 285–289.
- Riordan, C. J. (1986). Spectral solar irradiance models and data sets. *Solar Cells* 18, 223–231.
- Rossow, W. B. and R. A. Schiffer (1999, November). Advances in Understanding Clouds from ISCCP. *Bulletin of the American Meteorological Society* 80, 2261–2288.
- Rothman, L. S., I. E. Gordon, Y. Babikov, A. Barbe, D. C. Benner, O. F. Bernath, M. Birk, L. Bizzocchi, V. Boudon, L. R. Brown, et al. (2013). The HITRAN2012 molecular spectroscopic database. *Journal of Quantitative Spectroscopy and Radiative Transfer* 130, 4–50.
- Sassen, K., Z. Wang, and D. Liu (2008, April). Global distribution of cirrus clouds from CloudSat/Cloud-Aerosol Lidar and Infrared Pathfinder Satellite Observations (CALIPSO) measurements. *Journal of Geophysical Research (Atmospheres)* 113(D8), D00A12.
- Seidelmann, P. K. (Ed.) (1992). *Explanatory supplement to the Astronomical almanac*. Mill Valley, CA: University Science Books. United States Naval Observatory, Washington, D.C.
- Shettle, E. P. and R. W. Fenn (1976). Models of the atmospheric aerosols and their optical properties. In *AGARD Conference Proceedings*, Number 183, Lyngby, Denmark.
- Shettle, E. P. and R. W. Fenn (1979). Models of the aerosols of the lower atmosphere and the effects of humidity variations on their optical properties. Technical Report TR-79-0214, ADA 085951, AFGL.

- Shoemake, K. (1985). Animating rotation with quaternion curves. In *ACM SIGGRAPH computer graphics*, Volume 19, pp. 245–254. ACM.
- Smith, H. J. P., D. J. Dube, M. E. Gardner, S. A. Clough, and F. X. Kneizys (1978, January). FASCODE: Fast Atmospheric Signature CODE (spectral transmittance and radiance). Technical report.
- Tapley, B. D., S. Bettadpur, M. Watkins, and C. Reigber (2004). The gravity recovery and climate experiment experiment, mission overview and early results. *31*(L09607).
- Tapley, B. D., J. C. Ries, S. Bettadpur, and M. Cheng (2007). Neutral density measurements from the Gravity Recovery and Climate Experiment Accelerometers. *Journal of Spacecraft and Rockets* 6(44), 1220–1225.
- Thomas, G. and K. Stamnes (2002). *Radiative Transfer in the Atmosphere and Ocean*. Atmospheric and space science. Cambridge University Press.
- Thomas, J. B. (1999). An analysis of gravity-field estimation based on intersatellite dual-1-way biased ranging. Technical Report JPL Publication 98-15, Jet Propulsion Laboratory.
- Thompson, P. F., M. Abrahamson, S. Ardalan, and J. Bordi (2014). Reconstruction of the earth flyby by the juno spacecraft. In *24th AAS/AIAA Space Flight Mechanics Meeting, Santa Fe, New Mexico*.
- Utrillas, M. P., J. V. Boscá, J. A. Martínez-Lozano, J. Cañada, F. Tena, and J. M. Pinazo (1998, September). A comparative study of SPCTRAL2 and SMARTS2 parameterised models based on spectral irradiance measurements at Valencia, Spain. *Solar Energy* 63, 161–171.
- Vallado, D. A. (2001). *Fundamentals of Astrodynamics and Applications, Second Edition*. Microcosm Press, El Segundo, California.
- Van Helleputte, T., E. Doornbos, and P. Visser (2009). CHAMP and GRACE accelerometer calibration by GPS-based orbit determination. *Advances in Space Research* 43(12), 1890–1896.
- Vokrouhlický, D., P. Farinella, and F. Mignard (1993). Solar radiation pressure perturbations for Earth satellites, I. A complete theory including penumbra transitions. *Astronomy and Astrophysics* 280, 295–312.
- Vokrouhlický, D., P. Farinella, and F. Mignard (1994). Solar radiation pressure perturbations for Earth satellites, II. An approximate method to model penumbra transitions and their long-term orbital effects on LAGEOS. *Astronomy and Astrophysics* 285, 333–343.
- Vokrouhlický, D., P. Farinella, and F. Mignard (1996). Solar radiation pressure perturbations for Earth satellites, IV. Effects of the Earth’s polar flattening on the shadow structure and the penumbra transitions. *Astronomy and Astrophysics* 307, 635–644.

- Wyatt, S. P. (1961, March). The Effect of Radiation Pressure on the Secular Acceleration of Satellites. *SAO Special Report 60*.
- Wylie, D., D. L. Jackson, W. P. Menzel, and J. J. Bates (2005, August). Trends in Global Cloud Cover in Two Decades of HIRS Observations. *Journal of Climate* 18, 3021–3031.
- Ziebart, M. (2004). Generalized analytical solar radiation pressure modeling algorithm for spacecraft of complex shape. *Journal of Spacecraft and Rockets* 41(5), 840–848.